Politecnico di Torino

Department of Environmental, Land and Infrastructure Engineering

Master of Science in Georesources and Geoenergy Engineering

A.Y. 2024/2025

Molecular diffusion of CO_2 and H_2 through caprock and formation water

Supervisors:	Candidate:
Prof. Dario VIBERTI	Vanessa EL DAHDAH
Dr. Cristina SERAZIO	

July 17, 2025

Abstract

This thesis investigates molecular diffusion phenomena in underground storage of CO_2 and H_2 in depleted gas reservoirs. Furthermore, a sensitivity analysis on how grid resolutions may impact numerical results is carried out. Four simulation cases all based on compositional fluid modeling were run for 5,000 years. Two cases consider a fine 1 m × 1 m × 0.5 m mesh (cases A1, A2), and a coarse 11 m × 11 m × 0.5 m mesh (cases B1, B2). All cases are done using the same rock properties, fluid properties and boundary conditions. Analysis of results shows that the inherent properties of each gas (density, solubility and molecular size) govern the outcome. In the high-resolution models roughly 23 % of the CO_2 dissolves into the surrounding brine, while only about 3-4 % of the H_2 does so, even though both gases spread just a few meters from the wellbore (≈ 3 m for CO_2 and 0.5 m for H_2). Coarsening the grid cuts the dissolved mass by four-to-six-fold without changing penetration depth, showing that true diffusion length is set by physics, whereas the absolute amount calculated is highly sensitive to mesh size. In every scenario the overlying shale caprock limits total losses to less than 1 % of the injected volume, confirming its long-term sealing capacity. Overall, a fine grid is essential for accurate CO_2 mass-balance assessments, while a coarse grid is usually adequate for initial H_2 storage screening. With appropriate design focus, pressure management for CO_2 and purity maintenance for H_2, both gases can be stored safely in depleted reservoirs for millennia.

Acknowledgment

I would like to express my deepest gratitude to **Professor Dario Viberti** and **Dr. Cristina Serazio**, whose guidance, patience and enthusiasm were indispensable to the completion of this thesis. I am equally thankful to all the professors who have accompanied me throughout this academic journey; their teaching has shaped both my knowledge and my curiosity. I also wish to acknowledge the **Lebanese University** and **Politecnico di Torino** for granting me the invaluable opportunity to pursue this double-degree program. To my family, whose unwavering love and support have carried me every step of the way—I would not be here without you. Finally, heartfelt thanks to my friends and classmates, whose camaraderie turned long days of study into memorable moments and made this experience truly enjoyable.

Contents

List of Tables

List of Figures

Introduction

The melting of polar ice, the occurrence of intense heat waves, and the unrelenting rise in sea level are all signs that climate change is becoming a reality rather than a far-off prediction. The increasing supply of long-lived greenhouse gases, of which carbon dioxide (CO_2) is by far the major source, is tracked by all of these symptoms. In 2023, the global mean CO_2 reached a new high of 419.3 parts per million, which was more than 50% higher than the pre-industrial baseline [**NOAA Climate.gov, 2023**]. Approximately three-quarters of all greenhouse gas emissions are caused by the energy system, which still heavily depends on fossil fuels for everything from power plants and refineries to automobiles and boilers, according to the **IEA 2024**. Accordingly, the 2015 Paris Agreement stipulates those emissions must peak before 2025 and decrease 43% by 2030 in order to limit the increase in global temperature to 1.5 °C [**UNFCC, 2015**]. In addition to cleaner energy, removing the CO_2 that has already been produced on a big scale will be necessary to meet that goal.

One proven remedy is carbon capture, utilization and storage (CCUS), which separates CO_2 from flue gas or process streams and injects it into deep geological formations. The International Energy Agency [**IEA, 2020**] notes bluntly that *"reaching net-zero will be virtually impossible without CCUS*". An unparalleled multi-decade dataset on subsurface confinement is provided by the Sleipner field in the Norwegian North Sea, where about one million tons of CO_2 have been injected annually since 1996 with no discernible escape [**Equinor, 2019**]. An impermeable cap-rock, usually shale or evaporite, is essential to closing the storage complex in such projects.

Hydrogen (H_2) is becoming a second pillar of the energy transition as CO_2 disposal progresses. The IEA predicts that global consumption will surpass 100 Mt in 2024 with additional rise under nearly all policy scenarios. In 2023, it hit 97 Mt, up 2.5% from the year before [**IEA, 2024**]. H_2 provides a low-carbon feedstock for steel, fertilizers, shipping, and firm electricity because it only creates water when utilized in fuel cells or burners. However, the safe and affordable storage of tens of terawatt-hours of hydrogen is essential for large-scale implementation. Deep aquifers, depleted gas fields, and salt caverns are examples of underground solutions that complement seasonal renewable energy fluctuations and offer capacities orders of magnitude greater than those of surface tanks or cryogenic vessels [**Heinemann et al., 2021**].

Though each gas has unique behaviors that need to be taken into consideration, the literature generally suggests that underground storage of CO_2 and H_2 is physically possible. Decades of research and field experience have made CO_2 storage effective; large-scale initiatives have used methods like mineral fixation, solubility trapping, and structural trapping to store CO_2 without experiencing considerable leakage [**IEAGHG, 2024; Kampan et al., 2016**]. Although it has been demonstrated that depleted gas reservoirs can theoretically store H_2, hydrogen's low density and high diffusivity mean that it will occupy a larger volume and possibly mix more than natural gas. Hydrogen storage is becoming a prominent part of the clean energy transition. Important research highlights that although the fundamental trapping mechanisms are comparable to those of natural gas storage [**e.g., Feldmann et al., 2016; Paterson 1983; Pfeiffer and Bauer 2015**], H_2 may encounter more mobile fingering and buoyancy override because of an unfavorable mobility ratio with brine (low viscosity H_2 vs water). An unbroken shale can keep gas for geologic ages (with diffusion losses being low), but both gases need a high-quality caprock for long-term retention. Two strategic questions are brought up by these differences. First, is it possible for an undamaged cap-rock to exclude a buoyant, highly diffusive H_2 plume as well as it can CO_2? Second, how much gas is lost through slow molecular diffusion through the cap-rock and dissolution into formation brine over operational and post-closure time-scales — from months in cyclic storage to thousands of years as required by regulators — and how sensitive are those losses to reservoir simulators' numerical resolution?

This project tackles those open questions by isolating diffusion-driven transport of CO_2 and H_2 at the reservoir–cap-rock interface and within formation water by numerical simulations of simplified case studies**.** Bulk diffusivities were calculated in two steps. Gas-phase diffusivity was estimated with the Wilke–Lee correlation; although this gives values of the correct order of magnitude, it is known to be less accurate at the ≈150 barsa pressures relevant in subsurface formation conditions. For diffusion in water and in dense-phase CO_2 (treated by the simulator as an oil pseudo-component), coefficients were instead interpolated directly from published measurements at the reservoir conditions of 50 °C and 150 barsa. Then the effective diffusivities were calculated based on the porosity, bulk diffusivities, and the tortuosity. Then in order to explicitly quantify the impact of grid resolution and timestep control on anticipated fluxes, the values are then implemented in a compositional simulator (tNavigator® - Rock Flow Dynamics) and run on matched grids, a coarse mesh of 11 m × 11 m × 0.5 m and a fine mesh of 1 m × 1 m × 0.5 m. Scenarios span a single injection-production cycle to five millennia of post-closure observation, allowing the cumulative impact on stored-gas inventory and purity to be assessed for depleted-field settings. By comparing CO_2 and H_2 under identical conditions, the study defines an error envelope for long-term leakage forecasts and proposes best-practice gridding guidelines for future CCS and underground-hydrogen projects.

This manuscript is divided into three chapters. Chapter 1 provides a literature review about the CO_2 and H_2 storage by analyzing the primary geological settings, tracing the development of CO_2 sequestration and emerging H_2 storage, and explaining how phase behavior, diffusion theory, caprock integrity, and simulator capabilities influence present knowledge and highlight knowledge gaps. Furthermore, the Cartesian grid, GERG fluid description, petrophysical constants, explicit diffusion and dissolution options, equilibrium initialization, and the depletion-injection schedule that establishes the baseline for every run are all covered in detail in Chapter 2. Chapter 3 quantifies the CO_2- and H_2-flux into the caprock and aquifer, presents pressure, composition and components’ solubility as well as water mass density forecasts for the four grid/fluid scenarios, and evaluates how sensitive plume evolution is to diffusion coefficients, grid resolution, and important model assumptions.

1. State of the Art

1.1 Subsurface Storage of CO_2 and H_2

CO_2 Storage History

Human activity is changing the Earth's climate more and more. The amount of greenhouse gases present in the atmosphere is one of the issues. CO_2 is the most important greenhouse gas. As a result, the quantity of CO_2 must be reduced. Carbon dioxide Capture and Storage (CCS), referred to as CO_2 sequestration, is one way to do this. As the name suggests, CCS is a method that involves directly removing CO_2 from major sources, such as power stations or industrial sites. After that, the captured CO_2 is moved via trucks and pipelines to be long-term injected into deep formations.

Dedicated CCS pilot projects began to appear by the late 1990s and early 2000s, despite the fact that CO_2 injection for enhanced oil recovery (EOR) in West Texas began in the 1970s [**Lake, 2014**]. For example, the Frio Brine Pilot in Texas (2004–2005) tested monitoring methods and observed plume migration by injecting around 1,600 tonnes of CO_2 into a salty aquifer [**Ilgen & Cygan, 2016**]. Around 67,000 tonnes of CO_2 were injected into a sandstone reservoir in Germany as part of the Ketzin project (2008–2013), which offered important insights on onshore monitoring and verification in Europe [**Ivandic et al., 2015**]. The Weyburn–Midale project in Canada, which has injected more than 30 million tonnes of CO_2 for both EOR and long-term storage since 2000, was another significant event [**Majer et al, 2018**].

Furthermore, projects such as Norway's Sleipner field, which has been injecting more than 19 million tonnes of CO_2 into the Utsira sandstone deposit since 1996, are examples of large-scale CO_2 storage [**Equinor ASA, n.d**]. Similarly, In Salah in Algeria (2004–2011) yielded information on geomechanical monitoring and caprock integrity by storing over 3 million tonnes of CO_2 in a deep saline formation [**Morris et al., 2011**]. More recently, one of the biggest modern CCS projects is the Gorgon project in Australia, which plans to inject 3.3 to 4 million tonnes of CO_2 annually under Barrow Island [**DEMIRS, 2025**].

Since 2017, global CCS capacity has expanded at an average 32 % compound annual rate, and the project pipeline hit record highs in July 2024 with 628 projects, 60 % more than the previous year, including 50 operating facilities (three dedicated to transport / storage) and 44 under construction (seven transport / storage) [**Global CCS Institute, 2024**]. Capacity expansion from 2010 to July 24, 2024, is depicted in Figure 1-1. Operational experience at Sleipner, Weyburn–Midale and In Salah highlights the importance of detailed site characterization, time-lapse seismic and microseismic monitoring, and active pressure management to safeguard injectivity and caprock integrity [**Chadwick et al., 2006; IPCC, 2005; Riddiford et al., 2004;**

Wilson & Monea, 2004]. Parallel regulatory evolution—from early EOR-centered rules to comprehensive storage regimes such as the EU CCS Directive 2009/31/EC, U.S. EPA Class VI well standards, and stringent provincial frameworks that enabled Canada's Quest project—has underpinned this growth [**European Commission, 2009; Global CCS Institute, 2022, 2024; US EPA, 2010**].

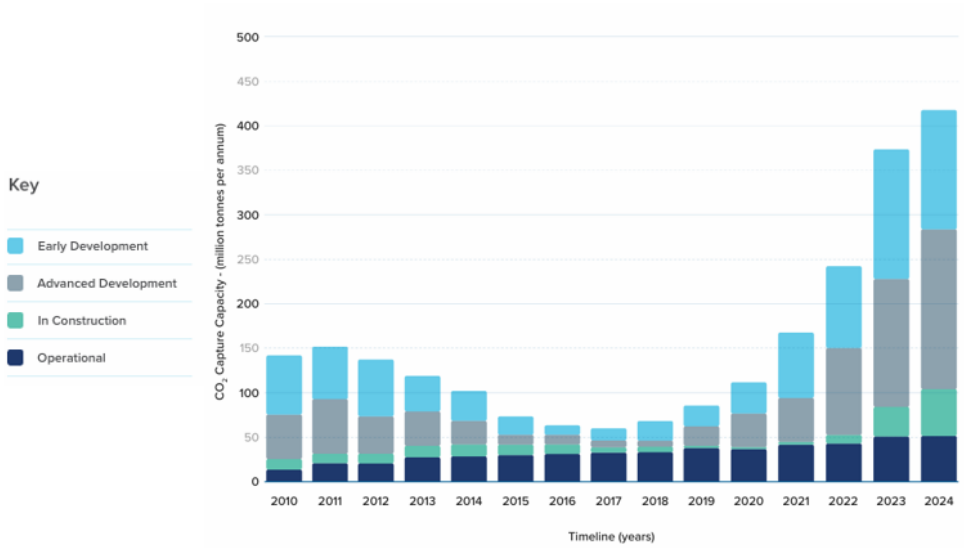

Figure 1-1: The commercial CCS facility pipeline's CO_2 capture capacity since 2010 by GLOBAL STATUS OF CCS REPORT, 2024.

Emerging hydrogen storage

At the forefront of numerous energy strategies is the shift to renewable and green energy. The availability of each energy source, such as sun or wind, determines how much electricity may be produced from renewable sources. If a sizable portion of energy output comes from renewable sources, fluctuations in its availability could result in energy shortages. Power-to-Gas technology (P2G), which transforms electrical power into gaseous fuel, is one way to lessen these shortages [**Buttler & Spliethoff**, **2018**]. The majority of P2G systems generate hydrogen by electrolysis, which can then be stored for a while and retrieved as needed. Nowadays, hydrogen is typically kept in highly insulated tanks at very low temperatures or as a gas in extremely high-pressure vessels [**Langmi et al., 2022**]. Underground geological storage facilities, such depleted natural gas or oil reservoirs, can offer an extensive storage capacity. Furthermore, because underground storage does not come into contact with ambient oxygen—a mixture of hydrogen and air is explosive in a very wide range, from 4% to 74% [**Rhodes, 2011**]—it is safer than above-ground storage tanks.is the case have lying before them the objects in space and time. These are the explanations for the recent, significant consideration of underground hydrogen storage (UHS) [**Benetatos et al., 2021; Zivar et al., 2021**].

Underground hydrogen storage (UHS) is less mature than CO_2 storage, but pilot studies exist. For instance, the Underground Sun Storage project in Austria tested the viability of H_2 storage in porous rock by injecting a 10% H_2/90% CH_4 gas combination into a depleted gas reservoir at a depth of 1200 m [**Miocic et al., 2023**]. Depleted fields and aquifers can physically hold hydrogen, as evidenced by the 50–60% H_2 found in some town gas storage sites in the middle of the 20th century (in Germany, France, etc.) [**Miocic et al., 2023**]. Figure 1-2 shows the ongoing projects for underground hydrogen storage in Europe [**Gas Infrastructure Europe (GIE), May 2022**].

These pilots show that repurposed gas reservoirs can act as "subsurface batteries," allowing power networks to strategically or seasonally buffer hydrogen, even though they are still less developed than CO_2 storage operations. As shown in Figure 1-3, in order to meet demand during times of high energy demand and low renewable energy production (2), hydrogen from renewable energy is stored during times of high renewable energy production (1) [**Heinemann et al., 2021**].

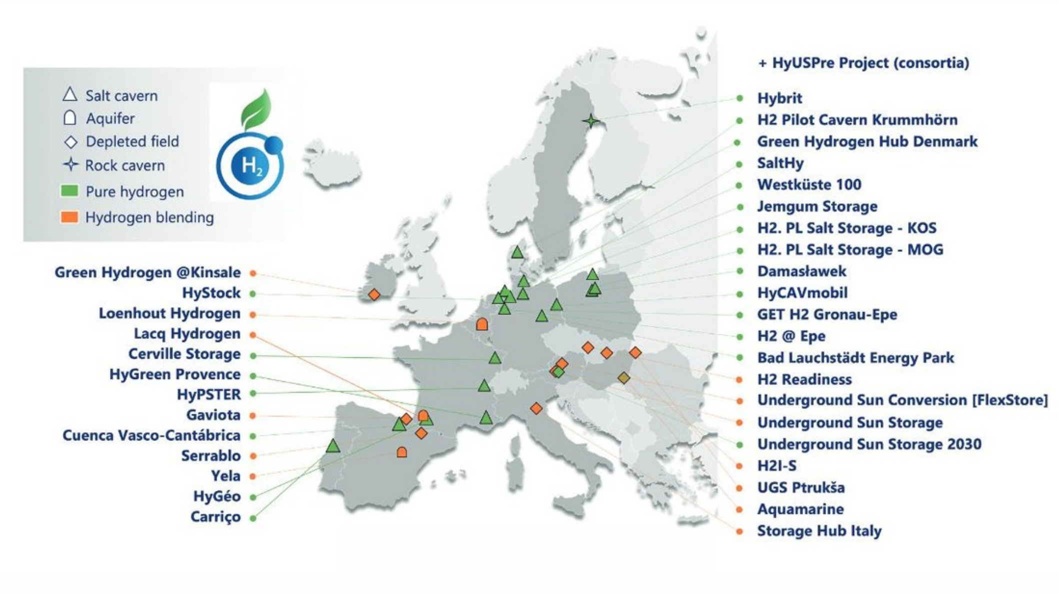

Figure 1-2: Underground hydrogen storage projects by Gas Infrastructure Europe, May 2022.

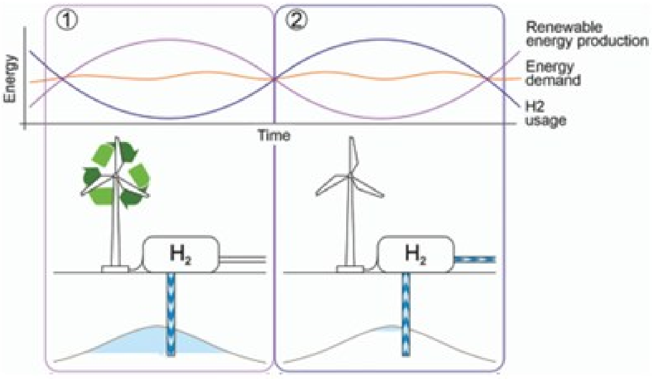

Figure 1-3: Schematic illustrating the storage of hydrogen produced from surplus renewable energy (1) for use during periods of high energy demand and low renewable output (2). (Adapted from Heinemann et al., 2021)

Further investigation is required to evaluate long-term integrity, microbial activity, and cost-effectiveness on larger scales, but preliminary findings point to low contamination and moderate diffusion losses over brief storage cycles [**Mao et al., 2024**]. Decades of experience storing natural gas can be applied to hydrogen storage in depleted fields. Both entail comparable procedures (such as pressure control, injection-withdrawal cycles, and cushion gas). However, compared to methane, hydrogen presents unique physical and operational hurdles due to its smaller molecular size and lower density [**Heinemann et al., 2021**]. For example:

- Greater Diffusivity: If H_2 is not well controlled, it may diffuse more quickly through the reservoir and possibly through caprock or wellbore materials, which could lead to leaks.
- Greater buoyancy than methane: Hydrogen may have a more noticeable vertical migration inside the reservoir.
- Microbial and Geochemical Reactions: When certain microorganisms consume H_2, they can produce byproducts like hydrogen sulphide or methane, which can change the composition of fluids and endanger the integrity of wells or the quality of gas [**Heinemann et al., 2021**].

The engineering infrastructure (compressors, monitoring systems, and well designs) created for natural gas storage provides a solid basis in spite of these variations. Operators can lower the additional cost of H_2 storage by modifying or improving current procedures, such as customizing cushion gas methods or protecting well integrity against increased diffusivity.

The necessity for large-scale, adaptable energy storage technologies is highlighted by the rise in renewable energy (wind, solar) and its sporadic nature. Water electrolysis during surplus renewable generation produces hydrogen, which can then be pumped into subsurface formations and recovered for use as fuel for transportation, industry, or power generation [**Mao et al., 2024**]. Important motivators include:

- Energy System Flexibility: Energy security and grid balance are provided by storing excess renewable electricity as hydrogen.
- Decarbonization Objectives: Many nations want to cut CO_2 emissions, and if hydrogen is made from low- or zero-carbon sources, it can be positioned as a "clean" energy source.
- Existing Infrastructure: By utilizing proven technologies from the oil and gas industry, repurposing exhausted fields and gas pipeline networks reduces upfront capital expenditures.
- Policy and Market Incentives: Industry investment in new storage projects is stimulated by government regulations, carbon pricing, and green hydrogen subsidies [**IEA, 2020**].

Notwithstanding these advantages, issues with chemical reactivity in reservoir conditions, long-term confinement during repeated injection–withdrawal cycles, and the feasibility of extrapolating pilot results to commercial operations still need to be addressed. Continued research and demonstration projects will be essential to guaranteeing dependable, secure, and reasonably priced subterranean hydrogen storage as the usage of hydrogen increases, especially in Europe and other nations investing in hydrogen economies.

Underground Gas Storage Types

Gases such as CO_2 and H_2 can be stored in a variety of geological formations, each with unique benefits and limitations [**IEA, 2020; IPCC, 2005**]. Subterranean gas storage frequently exhibits more complicated behavior than anticipated [**Amid et al., 2016; Hagemann et al., 2016**]. As a result, using certain geological features is restricted [**Gąska, 2012**]. Subterranean geological conditions and constraints on the Earth's surface determine whether the geological structure may be used for subterranean gas storage. One of the most important aspects of planning and building underground gas storage is locating and choosing suitable locations [**Carneiro et al., 2019; Lewandowska-Śmierszchalska et al., 2018; Matos et al., 2019**]. The general geology of the region, rock types, structural and tectonic factors, seismic hazards, hydrogeological and geothermal issues, the physical and chemical characteristics of the stored gas that influence its behavior in subterranean space, and geotechnical factors are among the geological criteria that should be considered [**GWPC & IOGCC, 2017; Kruck & Crotogino, 2013; Matos et al., 2019**]; also see [**Lewandowska-Śmierszchalska et al., 2018, Tarkowski, 2019**].

Natural gas storage (UGS) in salt caverns and porous rocks is something we have many years of experience with [**Basniev et al., 2010; Crotogino et al., 2010**; **GWPC & IOGCC, 2017**]. Additionally, we don't have much expertise storing hydrogen in salt caverns, which are mostly utilized by the petrochemical sector [**Goulart et al., 2020; Kruck & Crotogino, 2013; Pottier & Blondin, 1995**]. The primary distinction is that hydrogen's physiochemical characteristics necessitate greater care than those of natural gas, particularly with regard to leakage, monitoring, chemical affinity, and possible chemical, biological, or microbial interactions. The oil industry has been regularly injecting liquids into rock formations, reservoir waters, or acid gasses (H_2S and CO_2) for a number of decades [**Uliasz-Misiak & Chruszcz-Lipska, 2017**]. There were 662 subterranean natural gas storage facilities with a combined capacity of 421 billion Nm^3 in the world in 2018. Aquifers accounted for 12% of storage sites (77 installations), salt caverns for 15% (99 sites), and depleted hydrocarbon reserves for 73% (486 sites) [**Cornot-Gandolphe**, **2019**]. Before this technology is used on an industrial scale, study and testing are necessary to determine the specificity of hydrogen, even though the expertise of storing natural gas underground can be applied to the other gases under consideration.

Depleted Oil and Gas Reservoirs

These proven hydrocarbon traps have retained fluids for geological timescales, demonstrating the robustness of their structural seals and caprocks. Extensive subsurface data gathered during field development reduce site-characterization costs, and existing wells and pipelines can often be repurposed. After production, CO_2 largely replaces the former hydrocarbon-saturated pore volume, although part of the space is inaccessible because of residual water imbibition and capillary trapping [**IPCC, 2005**]. For H_2 storage, roughly 40 % of the capacity must remain as cushion gas, often the residual CH_4, to sustain deliverability, while 50–60 % acts as working gas in annual injection–withdrawal cycles [**Panfilov, 2016**]; mixing limits imposed by gas-quality regulations may require additional CH_4 buffering [**IEA, 2019**]. Key uncertainties concern the integrity of legacy wells, geochemical or microbial reactions with residual fluids, and pressure-induced seismicity, yet these formations currently account for about 81 % of underground gas storage worldwide [**Xie et al., 2009**]. Figure 1-4 shows a depleted reservoir left with only the native gas needed to preserve the integrity of the formation after hydrocarbons are extracted.

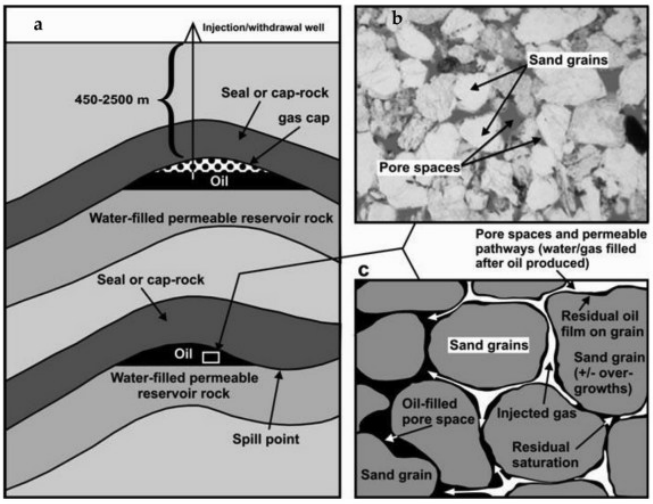

Figure 1-4: a) A summary of the filling and depletion processes of reservoirs. b) A microscopic picture shows oil-filled reservoir pores. c) Diagram showing how natural gas (oil) escapes pores and injected hydrogen occupies them [Wallace et al., 2021].

Deep Saline Aquifers

Brine-filled sedimentary formations are ubiquitous and offer vast theoretical capacity. In confined settings (Figure 1-5), structural or stratigraphic barriers provide vertical and lateral seals; in open aquifers (Figure 1-6), lateral pressure dissipation controls plume migration. For CO_2, storage efficiency hinges on caprock integrity and active pressure management to prevent fracturing or leakage. For H_2, similar reservoirs can be used, although experience is limited and a high fraction of cushion gas (≈ 80 %) is usually required, allowing only one or two operational cycles per year [**Tarkowski, 2019**]. Figure 1-7 shows the conversion of a saline aquifer into H_2 storage facility. Thorough site-specific appraisal—seismic imaging, coring, laboratory reactivity tests, and dynamic modelling—is therefore essential, and the absence of pre-existing infrastructure often makes saline aquifers more expensive to develop than depleted fields.

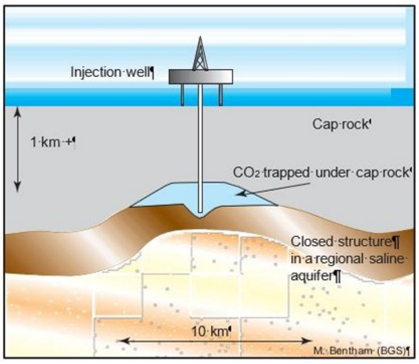

Figure 1-5 Confined aquifer [Bentham & Kirby, 2005].

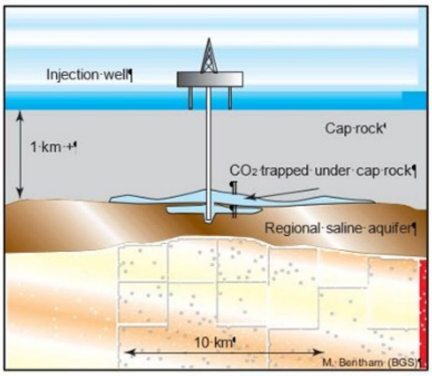

Figure 1-6: Unconfined aquifer [Bentham & Kirby, 2005].

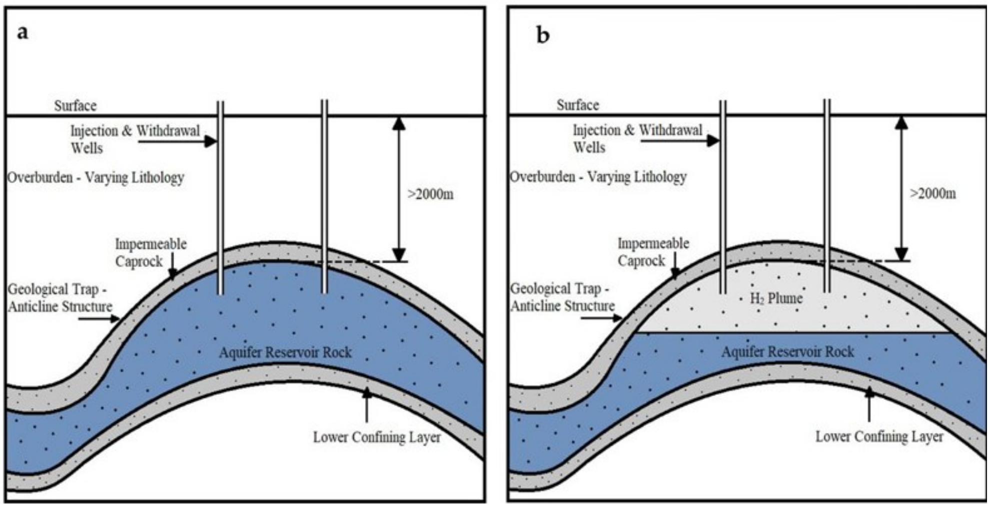

Figure 1-7: Schematic of an aquifer (a) prior to and (b) following H2 injection [Wallace et al., 2021].

Unmineable Coal Beds (CO_2 only)

In low-permeability coals, CO_2 is stored by adsorption onto organic surfaces, preferentially displacing methane and enabling simultaneous enhanced coal-bed-methane production. Storage efficiency depends on fracture permeability, coal rank and depth, and on managing produced water and gas [**White et al., 2005**].

Solution-Mined Salt Caverns (H_2 only)

Salt caverns are considered one of the most favorable options for underground hydrogen storage due to their widespread presence in many sedimentary basins and their optimal occurrence at depths up to 1500 meters. The resulting cavern is subsequently filled with a cushion gas, which is the lowest internal pressure needed to keep the cavern intact and stop salt creep. A working gas capacity (WGC) of up to 78% might be attained by using the cushion gas, which is typically taken between 22 and 33% of the volumetric capacity and should be considered an initial expenditure because it is non-recoverable. Salt caverns, in contrast to porous technologies, do not necessitate careful consideration of multiphase phenomena that can lower injection rate as leftover water collects at the cavity's bottom. Other factors like the geology of the cavern walls and their mechanical and thermodynamic impacts do need to be taken into account. This offers the possibility of more than just seasonal energy storage since it permits many injection/withdrawal cycles (up to 10 per year). These formations are particularly attractive because of the thick salt deposits they contain, with well-recognized examples found across Europe. Their suitability is largely attributed to the exceptional sealing properties of rock salt—characterized by high compressive strength, low permeability, and natural plasticity—which enables the rock to self-heal and prevent leakage. Caverns are artificially created through a process called salt leaching (Figure 1-8), where fresh water is injected into the salt rock to dissolve it, and the resulting brine is extracted through the same borehole. This process forms large, cylindrical storage cavities, often covering an area of about 1 km^2, with cavern heights exceeding 150 meters and widths spanning several dozen meters.

These man-made caverns can then be entirely filled with hydrogen gas. Salt cavern storage offers high capacity, whether in single caverns or groups of caverns, and enables multiple (up to ten) injection and withdrawal cycles per year—significantly more than seasonal storage options. Monitoring is rigorous, involving geophysical surveys during cavern formation, periodic assessments during operation, and the development of detailed digital models. Although no surface infrastructure typically exists at these sites, the geological and mining conditions are generally well understood. Salt caverns also benefit from successful past experiences with hydrogen and other gas storage. However, challenges remain, including the need to manage cavern convergence (gradual inward collapse), undesirable chemical reactions between hydrogen and impurities like interbedded materials, and the necessity of sealing old boreholes or drilling new ones that are hydrogen-resistant. Additionally, creating these caverns requires access to appropriate technology and sufficient water for leaching. Despite these considerations, the cost of developing salt caverns is typically higher than that of repurposing depleted hydrocarbon fields, but their performance and reliability often justify the investment [**Crotogino et al., 2010; Heinemann et al., 2021; Lord et al., 2014; Tarkowski, 2019**].

In conclusion, geological appropriateness, project size, economic considerations, and operational needs—such as injection/withdrawal rates, pressure limitations, and long-term monitoring requirements—all influence which of these possibilities is best.

Trapping Mechanisms

The target formation's geological and petrophysical characteristics determine how well CO_2 and, to a lesser extent, H_2 can be stored underground [**IPCC, 2005**]. These characteristics control the amount of gas that can be held (capacity) and injected (injectivity) over time. Generally speaking, there are two major types of trapping mechanisms: geochemical and physical [**Chadwick et al., 2006; IPCC, 2005**]. The basic concepts of confinement, particularly structural trapping and caprock integrity, remain applicable even if H_2 exhibits different chemistry and lower solubility than CO_2 [**Heinemann et al., 2021**].

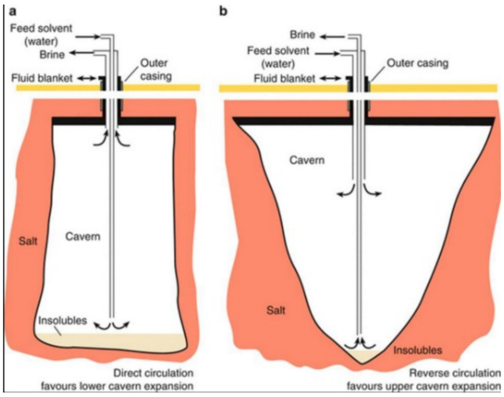

Figure 1-8: Creation of salt caverns by various configurations of dissolving systems [Warren, 2016].

Mechanisms of Physical Entrapment

I. Stratigraphic/structural and hydrodynamic entrapment

Immediately after injection stops, a buoyant plume ascends until it meets an impermeable or very-low-permeability seal. Mature hydrocarbon provinces demonstrate that such seals can retain fluids for millions of years and thus provide compelling analogues for both CO_2 and H_2 storage [**IEAGHG, 2024**]. Effective caprocks are laterally extensive sheets of shale, claystone or evaporite whose nanodarcy-scale permeability ($k<10^{-19}$ m^2) imposes capillary entry pressures of roughly 0.5–5 MPa, comfortably exceeding the buoyancy pressure of a super-critical CO_2 or a H_2 column up to several hundred meters tall. Once this threshold is reached, further upward migration is limited to extremely slow molecular diffusion through brine-filled nanopores [**Kampman et al., 2016**]. Caprocks are not chemically inert. Contact with CO_2-rich, mildly acidic brine ($pH \approx 5$) can dissolve feldspar, carbonates or clays at the reservoir/caprock interface, but concomitant precipitation—particularly of carbonates—often occludes pore throats and reinforces the seal [**Kampman et al., 2016**]. Extensive laboratory and field studies show that such reactions are typically confined to the first decimeter of the caprock and rarely degrade its bulk integrity [**IEAGHG, 2024**]. Hydrogen, by contrast, is a strong reducing agent and may stimulate abiotic or microbial pathways such as sulfate reduction (1.1) or methanogenesis (1.2):

$$5H_2 + SO_4^{2-} \leftrightarrow H_2S + 4H_2O \tag{1.1}$$

$$4H_2 + CO_2 \leftrightarrow CH_4 + 2H_2O \tag{1.2}$$

While these reactions can alter pH and redox conditions, they proceed slowly under storage conditions; to date neither laboratory columns nor field pilots have shown a measurable loss of seal capacity. Overall, structural trapping remains the primary containment line for both gases, and its performance is dominated by capillary rather than kinetic factors [**IEAGHG, 2024**].

II. Residual or Capillary Trapping

As the pressure front dissipates, formation brine re-invades the pore network and snaps the continuous gas phase into isolated ganglia, a process formalized by Land's trapping coefficient (C), which links normalized residual gas saturation S_{gr}^* to the normalized initial gas saturation S_{gi}^* during water-gas imbibition, through the formula [**Land, 1968**]:

$$S_{gr}^* = \frac{S_{gi}^*}{1+CS_{gi}^*} \tag{1.3}$$

where

$$C = \frac{1}{S_{gr,max}^*} - 1 \tag{1.4}$$

$S^{*}_{gr,max}$ is the normalized maximum residual gas saturation.

In sandstone reservoirs this capillary snap-off immobilizes about 10–40 % of injected CO_2 within days to months, which is a key safety buffer that has been documented in field and laboratory studies [**Krevor et al., 2015**]. Recent pore-network and reservoir-scale simulations extend the analysis to hydrogen. They predict Land coefficients of 0.2–2.7 in shallow (<1 km) and 0.3–3.2 in deeper (>2 km) formations, spanning the full spectrum from weak to very strong trapping. Translating those C values into operational terms, 49–62 % of injected H_2 could become residually trapped after each cyclic injection–withdrawal sequence in shallow reservoirs, and 48–60 % in deeper ones [**Khan et al., 2024**]. These high residual fractions highlight the fact that capillary trapping in UHS lowers the recoverable gas and may call for cautious reservoir selection and operational strategies (such as optimizing injection rates or cushion gas choices) to minimize losses.

Geochemical Trapping Mechanisms

I. Solubility Trapping

CO_2 dissolves into formation water until Henry's-law equilibrium is reached. The resulting CO_2-saturated brine is denser than the ambient formation water, so it sinks, creating stable, stratified layers that isolate the gas from the caprock. Because molecular diffusion in brine is slow, full dissolution of a large industrial plume may take thousands of years, yet even partial dissolution markedly reduces free-phase CO_2 mobility [**IPCC, 2005**]. Hydrogen solubility, in contrast, is almost an order of magnitude lower and decreases steeply with increasing salinity; thus, dissolution is a minor safety sink for H_2 and mainly represents a recoverable-gas loss [**Li et al., 2018; model data reported in Heinemann et al., 2021**].

II. Ionic and Mineral Trapping (CO2 only)

Dissolved CO_2 undergoes stepwise dissociation to bicarbonate and carbonate ions. In the presence of Ca^{2+}, Mg^{2+} or Fe^{2+} released from silicate dissolution, stable carbonate minerals precipitate:

$$CO_2 + Ca^{2+} + H_2O \leftrightarrow CaCO_3 + 2H^+ \tag{1.5}$$

$$CO_2 + Ca^{2+} + H_2O \leftrightarrow CaCO_3 + 2H^+ \tag{1.6}$$

$$CO_2 + Fe^{2+} + H_2O \leftrightarrow FeCO_3 + 2H^+ \tag{1.7}$$

Although reaction rates are highly temperature-dependent and generally slow (centuries), this mechanism ultimately locks carbon in the solid phase and is effectively irreversible on human timescales [**Kampman et al., 2016**].

III. Adsorption Trapping

Organic-rich coals and shales adsorb CO_2 strongly; competitive sorption can desorb methane and enable enhanced coal-bed-methane production [**White et al., 2005**]. Hydrogen physisorption is governed by weak van der Waals forces and becomes appreciable only at low temperature and high pressure, conditions rarely met at typical storage depths, so adsorption is not expected to play an important role in UHS [**Heinmann et al., 2021; Zhang et al., 2022**].

1.1 Physical Properties and Impact on Diffusion

Phase Behaviour and Critical Points

Under subterranean conditions, hydrogen and carbon dioxide behave quite differently. At about 7.38 MPa and 304 K (31.1 °C), CO_2 reaches its critical point (Figure 1-9) and transforms into a supercritical fluid [**Budisa & Schulze-Makuch, 2014].** Injectable CO_2 is dense (hundreds of kg/m^3) and can combine as a supercritical phase with liquid-like density since typical reservoir depths (>800 m) readily surpass these requirements. Therefore, supercritical CO_2 storage is more effective than gaseous or liquid CO_2 storage in subterranean deposits.

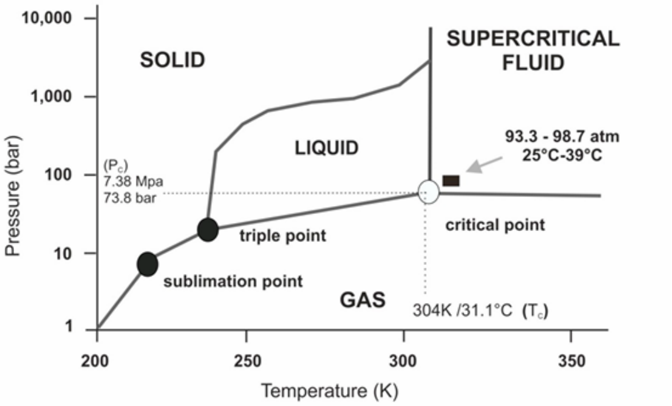

Figure 1-9: CO_2 phase diagram by Budisa & Schulze-Makuch, 2014.

On the other hand, H_2 is still a compressible gas in geologic storage due to its exceptionally low critical point (33 K and 1.285 MPa) [**Miocic et al., 2023**]. Figure 1-10 shows the different critical points of H_2, CH_4 and CO_2.

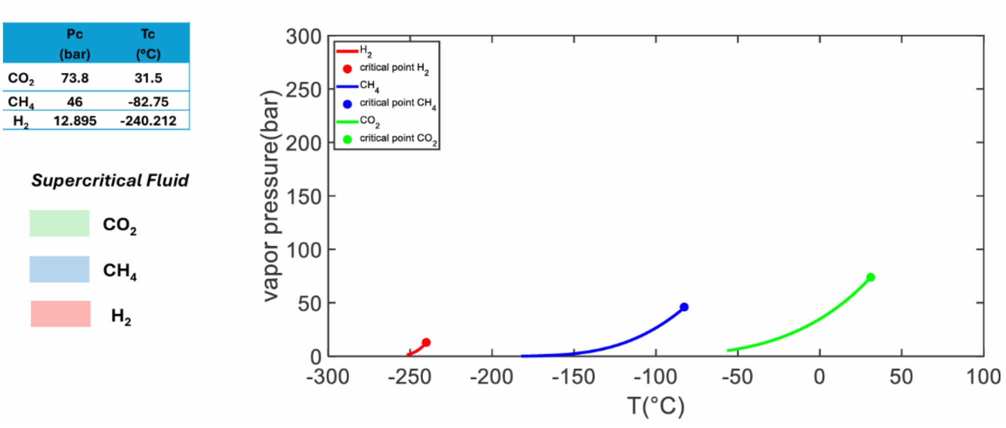

	Pc (bar)	Tc (°C)
CO_2	73.8	31.5
CH_4	46	-82.75
H_2	12.895	-240.212

Figure 1-10: Critical points of H_2, CH_4 and CO_2 [NIST, 2025].

Density and Viscosity under Reservoir Conditions

Even at reservoir pressures, the density of H_2 is orders of magnitude lower than that of CO_2 (0.09 kg/m³ vs. ~1.98 kg/m³ at NTP) [**Budisa & Schulze-Makuch, 2014**; **NIST, 2025**]. Similarly, because of the reduced molecular mass, the H_2 gas has a higher diffusion coefficient and a lower viscosity (89.48 µPoise at NTP). The following graphs (Figure 1-11 and Figure 1-12) demonstrate how CO_2 phase behavior and physical characteristics, such as density and viscosity, are highly dependent on temperature and pressure. However, the variation in density and viscosity of hydrogen is minimal within the range of normal conditions for subsurface storage [**Heinemann et al., 2021**].

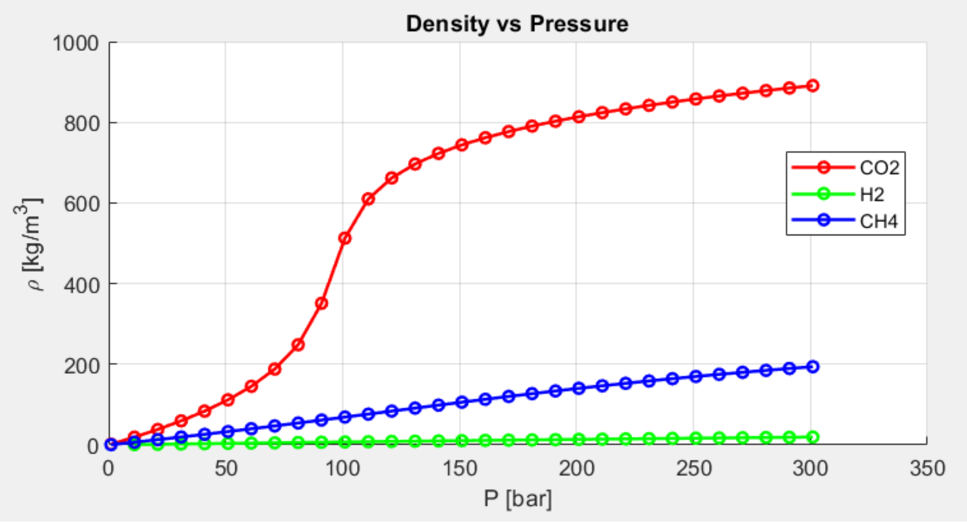

Figure 1-11: Plots of Density vs Pressure for CO_2, H_2 and CH_4 at a constant reservoir temperature of 45°C [NIST, 2025].

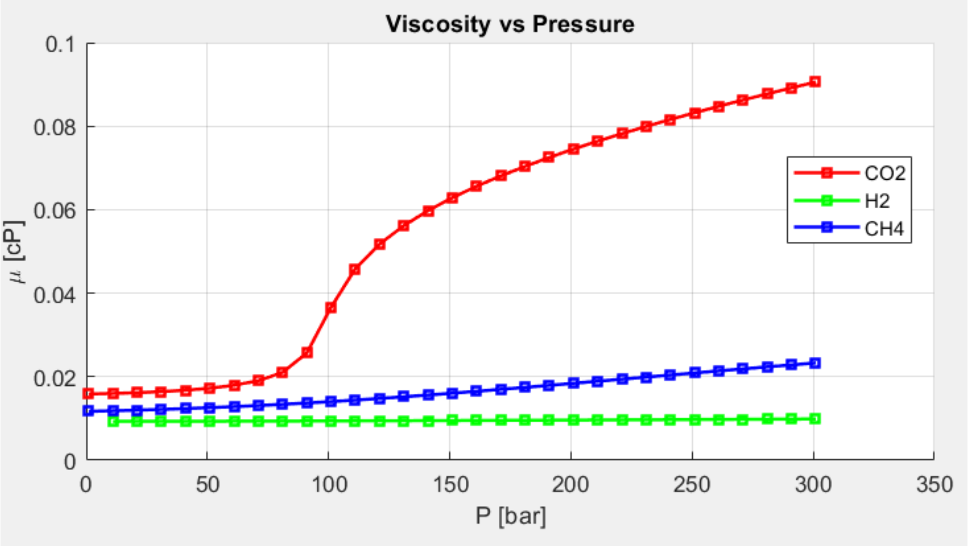

Figure 1-12: Plots of Viscosity vs Pressure for CO_2, H_2 and CH_4 at a constant reservoir temperature of 45°C [NIST, 2025].

Solubility and Dissolution in Brine

H_2 has very little solubility (around 0.0016 g per kg water at STP) [**NIST, 2025**], while CO_2 can dissolve considerably in formation brines and react to generate carbonic acid. This implies that little hydrogen losses from dissolution are to be anticipated. However, for subsurface microbiology, H_2 is a reactive electron donor; when CO_2 or sulfate is present, microorganisms can use it to make CH_4 or H_2S, changing the geochemical environment. Furthermore, H_2 solubility in water is 0.0000856 (mole fraction) at 319 K and 0.678 MPa, but it rises to 0.00103 (mole fraction) at 323 K and 7.9 MPa (Figure 1-14). This indicates that H_2 dissolution in water at subterranean circumstances is significantly higher than ambient settings. Moreover, brine ionic composition, temperature, and pressure all have an impact on H_2 dissolution; generally speaking, H_2 dissolution rises with rising temperature and pressure but falls with rising brine salinity. As the temperature rose from 323 K to 372 K, the solubility increased from 0.000631 to 0.000702 at a given pressure (10.1 MPa) and brine salinity (3 mol/Kg NaCl) (Figure 1-13). H_2 solubility in brine from 3 mol/kg NaCl to 5 mol/kg at 323 K and 15.1 MPa (Figure 1-15) [**A. Raza et al., 2022**].

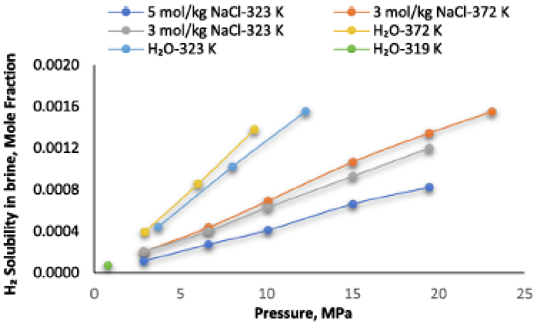

Figure 1-13: H_2 solubility in brine in function of pressure for different temperatures and salinities [A. Raza et al., 2022].

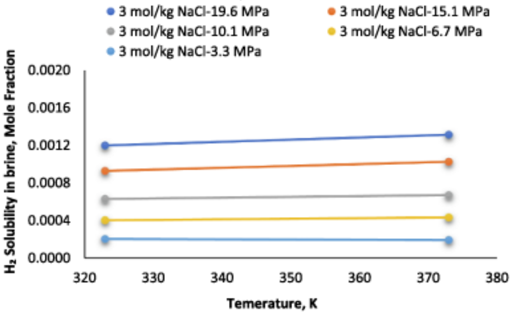

Figure 1-14: H_2 solubility in brine in function of temperature for different pressures. [A. Raza et al., 2022].

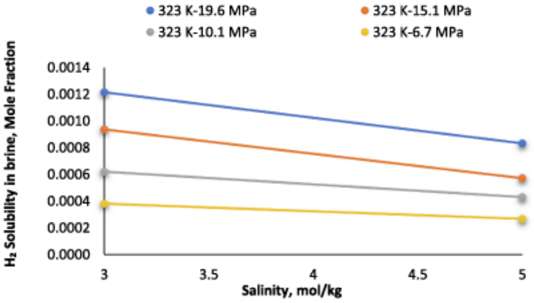

Figure 1-15: H_2 solubility in brine in function of salinity for different pressures. [A. Raza et al., 2022].

Since the H_2 loss in depleted non-aqueous liquids is roughly an order of magnitude more than that in H_2-aqueous liquids (e.g., 0.000215 in 3 mol/kg NaCl brine and 0.0269 in diesel at 3.3 MPa and 373 K), dissolution trapping can result in a considerable H_2 oil reservoir (as opposed to aquifers). Henry's law states that at a constant temperature, CO_2 solubility in formation water increases with increasing gas partial pressure (Figure 1-16).

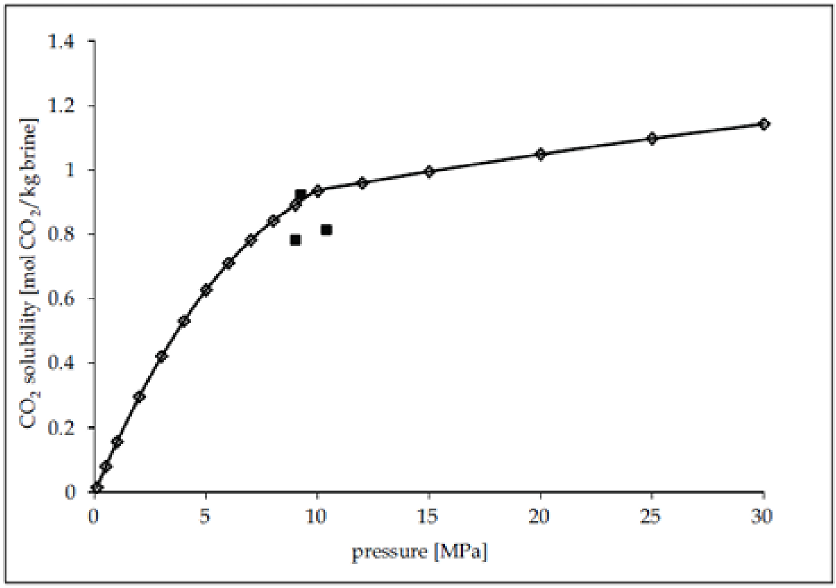

Figure 1-16: CO_2 solubility at 323K and 1 mol NaCl/kg brine as a function of pressure (Modelling and Experimental data) [Steel et al., 2016].

At constant pressure, the solubility of CO_2 in formation water falls as the temperature rises because thermal energy from adding heat to the solution overcomes the forces of attraction between the solvent molecules and the gas, which reduces the gas solubility (Figure 1-17).

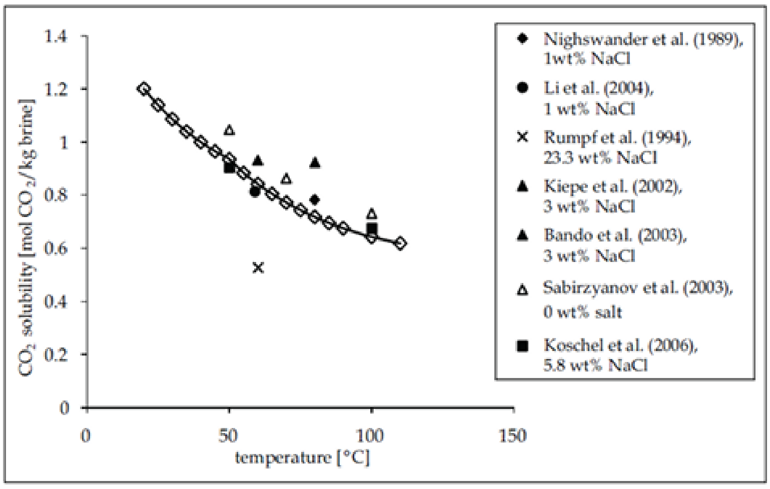

Figure 1-17: Temperature-dependent CO_2 solubility at 10 MPa and 1 mol NaCl/kg brine. (Modelling and Experimental data) [Steel et al., 2016].

At constant temperature and pressure, CO_2 solubility in formation water falls as salinity rises because the quantity of H^+ and O^{2-} ions that may absorb and dissociate gas molecules is decreased because the water molecules are drawn to the salt ions (Figure 1-18).

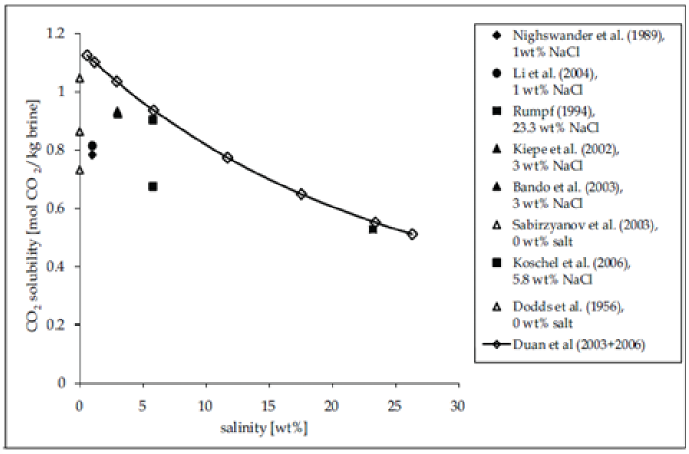

Figure 1-18: CO_2 solubility at 323K and 10MPa as a function of salinity. (Modelling and Experimental data) [Steel et al., 2016].

These fundamental property differences impact how each gas must be handled in storage designs.

1.3 Diffusion Theories: Fick vs. Maxwell-Stefan

The process of random molecule motion that propels mass movement from high to low concentration is known as molecular diffusion as described in the Figure 1-19 below.

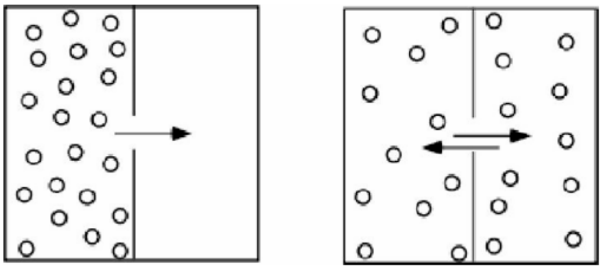

Figure 1-19: Molecular diffusion phenomenon.

While concentration gradients are the most common cause of diffusion, other causes include activity gradients (as in reverse osmosis), temperature gradients, total pressure gradients, and the application of an external force field (like in a centrifuge). Thermal diffusion is the diffusion of molecules caused by temperature; forced diffusion is the diffusion of molecules that produce an external field.

1.3.1 Fundamentals of Fick's Law

Over time, the concentration throughout a substance will become the same. When this occurs, the substance has reached a steady state. There are a few factors to consider while working with Fick's Law:

- The only evidence for Fick's Law comes from experimental observations. The formula for Fick's Law was developed using the data he gathered from his studies.
- All states of matter—solid, liquid, and gas—are covered by Fick's Law.
- From a high concentration to a low concentration, the diffused material travels in the direction of decreasing concentration.
- The system's constituents, temperature, and pressure all affect the diffusion coefficient. The diffusion coefficient is thought to stay constant within a specified range of temperature and pressure when ideal gases and diluted liquids are involved.

Fick's Law is stated formally as follows: The concentration gradient determines the molar flow resulting from diffusion. This indicates that the concentration of the substances and the region they must travel through determine the movement (flux) of mass (molecules) caused by diffusion. The number of molecules that go across a particular region in a given amount of time is known as the flux since one mole is equivalent to exactly $6.02214076 \times 10^{23}$ particles.

In a binary system, Fick's first law is written as [**Fick, 1855**]:

$$J = -D_{AB}\frac{dC_A}{dz} \qquad (1.8)$$

where:

- J: diffusion molar flux in mol/m^{2}s. The moles of a substance that will pass across a unit area in a unit amount of time are measured by J.
- D_{AB}: diffusion coefficient or diffusivity. It represents how much component A is compatible with component B. Given the details of the molecules, the diffusion constant can be calculated analytically or empirically. Since the flow is from a greater to a lower concentration, it is negative. It is expressed in m^2/s.
- C_A: molar concentration of component A in mol/m^3.
- d_z: distance in m.
- $\frac{dC_A}{dz}$: concentration gradient of A in the z direction (one dimension).

According to this law, the concentration gradient and the rate of diffusion are proportional. Put more simply, the differential in concentration across areas is what propels particle migration. In steady-state diffusion, the concentration gradient remains constant across time.

Fick's second law explains the time-varying nature of the concentration gradient itself. In essence, it is the rate at which the concentration gradient changes, showing how rapidly the system is approaching equilibrium. It is employed when the concentration gradient is not constant [**Fick, 1855**]:

$$\frac{dC_A}{dt} = D_{AB}\frac{d^2C_A}{dz^2} \tag{1.9}$$

We mostly rely on empirical correlations from the literature or experimental data to calculate the diffusivity D_{AB}. Direct laboratory measurements, such as pressure-decay or concentration-profile approaches, under carefully regulated temperature and pressure conditions, can be used to experimentally evaluate diffusivity [**Yan et al., 2024; Zhao et al., 2023**]. In essence, concentration profiles give a spatial perspective of the substance's distribution and how it changes over time, whereas the pressure decay approach observes the change in pressure to provide information on the diffusion process. However, semi-theoretical models are commonly used due to the inherent complexity and difficulties of precisely estimating diffusion in confined geological formations. Based on basic physical characteristics including molecular size, viscosity, temperature, and pressure, these correlations yield estimates of diffusivity that are almost as accurate as those obtained using direct experimental approaches. The availability of data and the level of precision needed for predictive modeling have a big impact on the method selection.

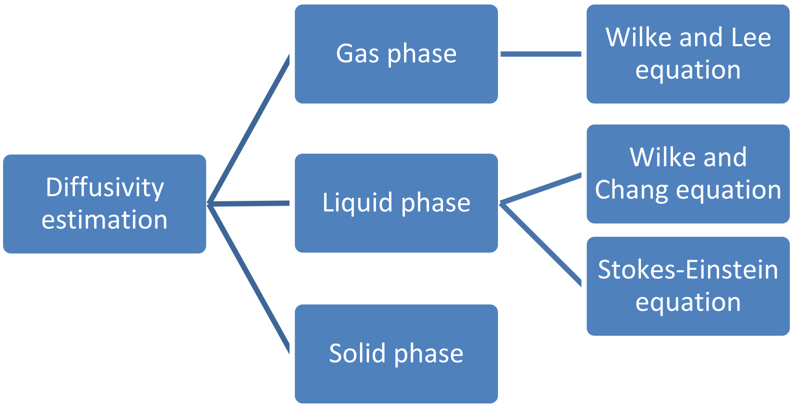

Diffusivity Estimation in Gas Phase

An example of a semi theoretical relation for estimating gas phase diffusivity is **Wilke & Lee, 1955**, which is one of the most widely techniques, and which has been demonstrated to be highly generic and accurate:

$$D_{AB} = \frac{\left[3.03 - \left(\frac{0.98}{M_{AB}^{\frac{1}{2}}}\right)\right](10^{-3})T^{\frac{3}{2}}}{PM_{AB}^{\frac{1}{2}}\sigma_{AB}^{2}\Omega_D} \qquad (1.10)$$

- D_{AB}: diffusion coefficient in cm^2/s.
- M_A, M_B: molecular weights of A and B, respectively and $M_{AB} = 2\left(\frac{1}{M_A} + \frac{1}{M_B}\right)^{-1}$.
- T: temperature in K.
- P: Pressure in bar.
- $\sigma_{AB} = \frac{\sigma_A + \sigma_B}{2}$: collision diameter, a Lennard-Jones parameter for nonpolar. molecules expressed in Angstrom (Å).
- Ω_D: diffusion collision integral, a dimensionless correction factor that takes into account the final deformation and it is in function of temperature and the energy of the molecular interaction between A and B (ϵ).

In the gas phase, there is a high interaction between molecules. The graph below in Figure 1-20 demonstrates the relationship between temperature and the change in molecular behaviour, highlighting how gas molecules, being soft and not rigid spheres, interact with high levels of intensity in the gas phase, with their collision diameter and diffusivity varying as a function of temperature. This must be considered when calculating diffusivity in gas systems. The collision diameter is typically associated with the point where the interaction potential energy is at its minimum, which represents the closest distance between two molecules before repulsive forces dominate.

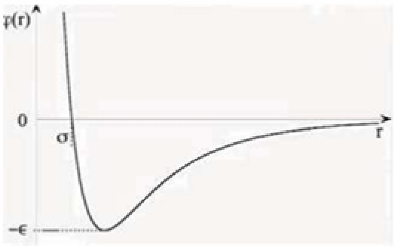

Figure 1-20: Graph showing the collision diameter between two molecules.

A very accurate approximation of Ω_D is derived from **Neufeld et al., 1972**:

$$\Omega_D = \frac{a}{(T^*)^b} + \frac{c}{\exp(dT^*)} + \frac{e}{\exp(fT^*)} + \frac{g}{\exp(hT^*)} \qquad (1.11)$$

The Table 1-1 below represents the parameters in the equation above [**Reid et al., 1987**]:

Table 1-1: Parameters of the correction factor equation.

$T^* = \frac{T}{\frac{\varepsilon_{AB}}{\kappa}} = \kappa T/\varepsilon_{AB}$	a=1.06036	b=0.15610
c=0.19300	d=0.47635	e=1.03587
f=1.52996	g=1.76474	h=3.89411

- T^*: dimensionless temperature.
- κ: Boltzmann constant $(1.38 \times 10^{-16} erg/K)$.
- $\varepsilon_{AB} = (\varepsilon_A \varepsilon_B)^{1/2}$: energy of molecular interaction for the binary system A and B (a Lennard-Jones parameter) expressed in erg $(10^{-7} J)$.

The Lennard-Jones constants for CO_2, H_2 and CH_4 are (Poling et al., 1987):

CO_2: $\sigma = 3.941$ Å , $\frac{\varepsilon}{\kappa} = 195.2$ K

H_2: $\sigma = 2.827$ Å , $\frac{\varepsilon}{\kappa} = 59.7$ K

CH_4: $\sigma = 3.758$ Å, $\frac{\varepsilon}{\kappa} = 148.6$ K

Nevertheless, these equations are substantially less effective at high pressures (for example at reservoir conditions where the pressure is 150 barsa) even though they accord with experiments at low pressures (approximately 15 bars). Few binary data are available at higher pressures; a reasonable empirical recommendation for self-diffusion is the corrective empirical equation [**Takahashi, 1974**]:

$$\frac{D_{AB}P}{(D_{AB}P)^+} = f(T_r, P_r) \qquad (1.12)$$

where:

- D_{AB}: diffusion coefficient in cm^2/s.
- P: pressure in bar.

The use of low-pressure values is indicated by the superscript $^+$. Figure 1-21 displays the function $f(T_r, P_r)$. Equations (1.13) to (1.16) are utilized to derive pseudocritical characteristics, which are then applied to compute the reduced temperatures and pressures [**Poling et al., 2001**].

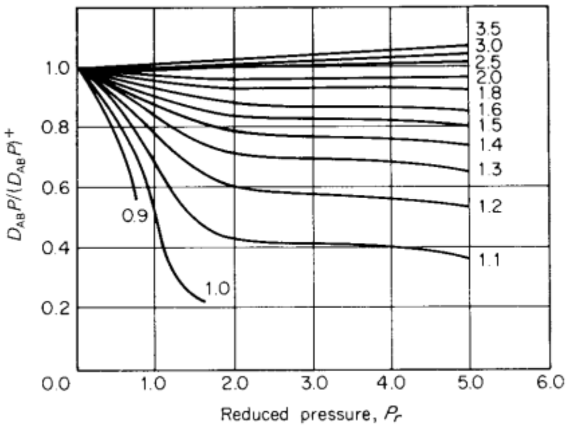

Figure 1-21: Takahashi correlation for the binary diffusion coefficient's response to temperature and pressure. The lines are at a constant reduced temperature [Poling et al., 2001].

$$T_r = \frac{T}{T_c} \tag{1.13}$$

$$T_c = y_A T_{cA} + y_B T_{cB} \tag{1.14}$$

$$P_r = \frac{P}{P_c} \tag{1.15}$$

$$P_c = y_A P_{cA} + y_B P_{cB} \tag{1.16}$$

Eq. (1.17) can depict both high-pressure liquid and high-pressure gas behavior, according to **Riazi & Whitson, 1993**. For the former, values from Figure 1-21 must be read. The latter does not reproduce the right value in the low-pressure limit and necessitates viscosity information.

$$\frac{\rho D_{AB}}{(\rho D_{AB})^+} = 1.07\left(\frac{\mu}{\mu^0}\right)^{b+cP_r} \tag{1.17}$$

where:

- $b = -0.27 - 0.38\omega$.
- $c = -0.05 + 0.1\omega$.
- μ^0: viscosity at low pressure.
- ω: acentric factor.
- $P_r = P/Pc$.
- $P_c = y_A P_{cA} + y_B P_{cB}$.
- $\omega = y_A \omega_A + y_B \omega_B$.

Diffusivity Estimation in Liquid Phase

Diffusion coefficient values for liquids are significantly lower than those for gases because molecules in liquids are closely packed and heavily influenced by the forcefields of diffusion coefficients of nearby molecules. Diffusion coefficient calculations using liquid state theories are highly idealized, and none of them adequately provide relations for D_{AB} calculation. However, in a number of instances, the structure of a theoretical equation has served as the foundation for practical prediction techniques. The examination of big spherical molecules diffusing in a diluted solution serves as an example. Then, according to hydrodynamic theory [**Bird et al., 1960; Gainer & Metzner, 1965**], the diffusion coefficient is written as (Stokes-Einstein equation):

$$D_{AB} = \frac{(RT)}{6\pi \eta_B r_A} \qquad (1.18)$$

where:

- D_{AB}: diffusion coefficient in cm^2/s.
- R: Boltzmann's constant: $1.38.10^{-16} g.\frac{cm^2}{s^2K}$ or $1.38.10^{-23} kg.\frac{m^2}{s^2K}$.
- η_B : viscosity of the solvent in Poise (g/cm.s or 0.1 kg/m.s).
- r_A: radius of "spherical" solute in cm.

The equation above strictly applies to macroscopic systems, and it applies to systems where the ratio of the radius of the solute to the radius of the solvent is higher than five.

Furthermore, the **Wilke-Chang, 1955** technique, an older but still popular correlation for diffusivity estimation, is essentially an empirical adaptation of the Stokes-Einstein relation (1.18):

$$D_{AB}^0 = \frac{7.4\times10^{-8}(\phi M_B)^{\frac{1}{2}}T}{\eta_B V_A^{0.6}} \qquad (1.19)$$

where:

- D_{AB}^0: mutual diffusion coefficient of solute A at very low concentrations in solvent B in cm^2/s.
- M_B: molecular weight of solvent B in g/mol.
- T: temperature in K.
- η_B: viscosity of solvent B in cP.
- V_A: molar volume of solute A at its normal boiling point in cm^2/mol.
- ϕ: association factor of solvent B (dimensionless).

The Wilke-Chang equation is applied to systems where the ratio of the radius of the solute to the radius of the solvent is lower than five. This correlation is proposed for nonelectrolytes in an infinitely dilute solution.

The diffusion in the solid phase, more specifically in the porous media, will be explained in detail in paragraph 1.3.3.

1.3.2 Maxwell-Stefan Equations for Multi-Component Diffusion

The more general Maxwell-Stefan equations offer a rigorous framework for multicomponent diffusion, whereas Fick's rules are empirical and the diffusion process in a complex system cannot be adequately described by Fick's law due to its complexity [**D'Agostino et al., 2011; D'Agostino et al., 2012**]. Maxwell-Stefan (M-S) theory describes diffusion as a force-balance between chemical potential gradients and frictional drag between different species. There are certain general ideas about diffusion in multicomponent liquid mixtures that apply to gas mixtures as well and are discussed later. The fact that even the binary diffusion coefficients are frequently highly composition-dependent is one of the issues with diffusion in liquids. Therefore, it is challenging to get numerical values of the diffusion coefficients connecting fluxes to concentration gradients for multicomponent liquid mixtures. D_{AB} is typically thought to be independent of composition in gases. The Stefan Maxwell equation [**James Maxwell, 1972; Josef Stefan, 2007**] can be used to describe multicomponent diffusion in gases with this mathematical relation:

$$-\frac{1}{RT}\nabla\mu_1 = \frac{x_2(u_1-u_2)}{D_{12}} \qquad (1.20)$$

where:

- $\nabla\mu_1$: chemical potential gradient of component 1 at constant temperature and pressure.
- $u_1 - u_2$: difference between the average velocities of components A and B, which is proportional to the frictional force between the two components.
- x_2: mole fraction of species 2.
- T: temperature.
- R: universal gas constant ($8.314462618\ \mathrm{J.mol^{-1}}K^{-1}$).
- D_{12}: Maxwell-Stefan binary diffusion coefficient in relation with the friction coefficient between components 1 and 2. In a binary system the Fick coefficient D and the Maxwell-Stefan diffusivity $\widetilde{D}$ are linked by $D = \widetilde{D}\Gamma$ where Γ is the thermodynamic factor. For gases at low-to-moderate pressures and for ideal liquid mixtures, Γ=1, so $D = \widetilde{D}$. Unlike the lumped Fick coefficient, the Maxwell-Stefan diffusivity has a clear physical meaning as an inverse drag (friction) coefficient and cleanly separates drag effects from non-ideal thermodynamics [**Krishna & Wesselingh, 1997**].

The negative sign indicates that diffusion proceeds from high to low chemical potential. M-S simplifies to Fick's equation in a binary mixture with an equivalent diffusivity, but the distinctions become significant in concentrated solutions or mixtures of many gases. Three models for diffusion are described by **Sistan et al., 2019**: the standard Fickian, Maxwell-Stefan, and a so-called "generalized Fick", which takes into account elements such as chemical potential gradients, external drifts, and non-local transport effects in addition to basic concentration gradients. They point out that the simpler Fickian formulas have typically been used in commercial reservoir simulators, but these can be unreliable when composition gradients are significant [**Sistan et al., 2019**], as shown in Figure 1-22 below.

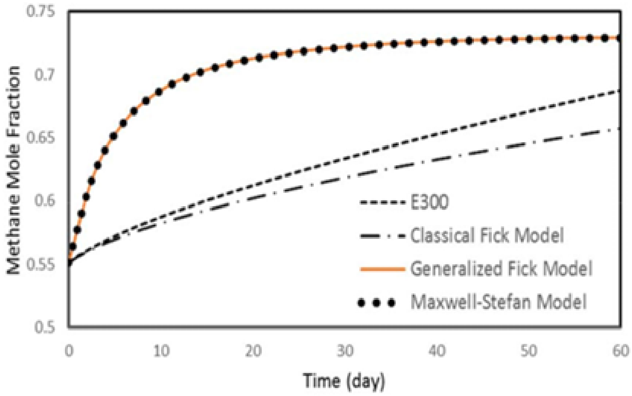

Figure 1-22: Mole fraction of methane in oil while injecting it in the matrix [Sistan et al., 2019].

According to research, multicomponent effects are better captured by Maxwell-Stefan and other sophisticated models (at the expense of complexity). For example, **Hoteit, 2013** enhanced gas injection modeling by including a Maxwell-Stefan diffusion model into a reservoir simulator. In conclusion, Maxwell-Stefan theory is required to rigorously treat diffusion in CO_2–H_2–CH_4 mixtures or other complicated subsurface fluids where interactions between species matter, even though Fick's law is sufficient for many applications.

1.3.3 Relevance in Porous Media: Effective Diffusion Coefficient

Diffusion happens through the linked pore space rather than an open fluid in porous reservoir rock or caprock. Diffusion only occurs through the small, twisted pores of the composite because the solid itself is impermeable and it effectively occurs over a greater distance than it would in a homogeneous material because the pores are not straight. It also takes place over a smaller cross-sectional area than that of a homogeneous material because the solid is impermeable. Due to the tortuous and partially constricted pore channels, the effective diffusion coefficient D_{eff} in rock is lower than the bulk diffusivity in free fluid and is expressed by **Boving et al., 2001**:

$$D_{eff} = \frac{D_{AB}\phi\delta}{\tau^2} \tag{1.21}$$

where:

- ϕ: porosity (dimensionless).

- τ: tortuosity (dimensionless) $\tau = \frac{L_{actual}}{L_{direct}}$.
- δ: constriction factor (dimensionless), only until the solute's size approaches that of the pore (less than 1 nm) does the constrictivity become significant [**Grathwohl, 1998**], otherwise, it is equal to 1 (Figure 1-23).

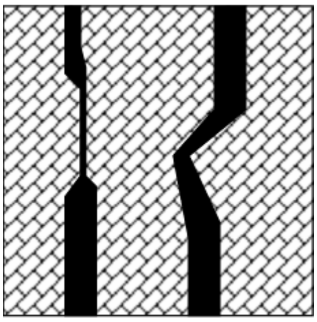

Figure 1-23: Diffusion cross sections are decreased by constrictivity [Frick, 1993].

D_{AB} can be found using either Wilke-Lee or Stokes-Einstein/Wilke-Chang relations as described before.

Therefore, we can conclude from the above relation that the more there are void spaces, the easier the diffusion and the higher the tortuosity, the more is undefined the shape and the longer and the more difficult is the diffusion (Figure 1-24).

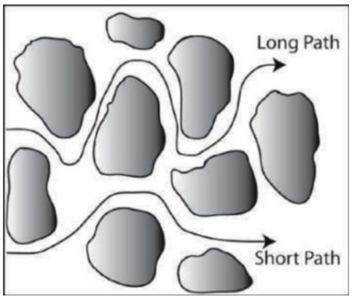

Figure 1-24: Diffusion pathways that are tortuous in porous materials. Mineral granules are represented by the color grey. Pore gaps are indicated by the white. When moving through porous medium, chemicals in the aqueous phase follow a tortuous route [Steefel & Maher, 2009].

The free-fluid diffusivity may be orders of magnitude higher than the effective diffusivity D_{eff} in highly tight rocks (low porosity and high tortuosity). For instance, only around 0.5% of the cross-section of a shale with a porosity of 0.05 and an effective tortuosity factor of 10 is available for straight-line diffusion.

When simulating caprock leakage, it is crucial to distinguish between bulk and effective diffusion: On a centimeter scale, CO_2 or H_2 may diffuse quite quickly in water-filled micropores, but the cumulative transfer is minuscule across a meter-thick shale. Core sample measurements in the lab verify that diffusion in brine-saturated rocks is extremely sluggish and heavily influenced by rock microstructure [**Kampan et al., 2016**]. Porosity, pore size distribution, and tortuosity must therefore be taken into consideration for an accurate assessment of diffusion in porous media, typically using an effective diffusivity calibrated to laboratory testing.

1.3.4 Impact of Reservoir Conditions on CO_2 and H_2 Diffusion

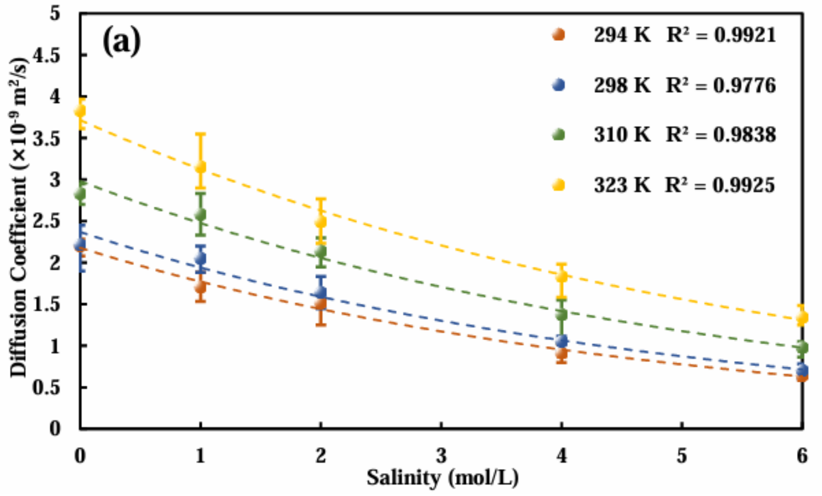

Figure 1-25: The diffusion coefficient of CO_2 in a 0 to 6 M NaCl solution at 10 MPa and temperatures between 294 and 323 K [Omrani et al., 2022].

Temperature, pressure, and fluid composition all affect a fluid's diffusion coefficient. Diffusion rates tend to increase at higher temperatures because of quicker molecular motion but they decrease as the salinity rises [**Omrani et al., 2022**]. Figure 1-25 illustrates how temperature and salinity changes together affect the CO_2 diffusion coefficient. Similarly, H_2 diffusivity increases with increasing temperature and decreases with increasing salinity [**Kerkache et al., 2025**], as shown in Figure 1-26.

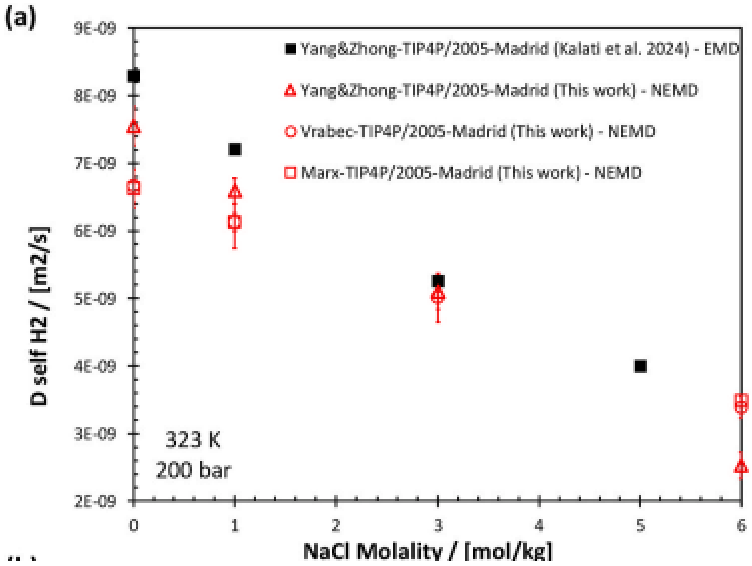

Figure 1-26: Different FF combinations and simulation techniques (EMD, NEMD) are used to show H_2 diffusion variation with the NaCl molality [Kerkache et al., 2025].

Most prior research indicates that pressure has no discernible impact on the diffusion coefficient, at least up to a certain temperature and pressure [**Cadogan et al., 2014; Tsimpanogiannis et al., 2021**]. However, **Zhang et al., 2015** asserted that although the diffusion coefficient of CO_2 rises linearly with pressure, this growth eventually diminishes. According to the findings of **Moultos et al., 2014**, the pressure effect on the diffusion coefficient increases with temperature but becomes insignificant before that. Figure 1-27 shows that there is neither a noteworthy trend suggesting the diffusion coefficients of CO_2 are trending toward higher or lower values with increasing pressure, nor is there a discernible shift in the coefficients at different pressures.

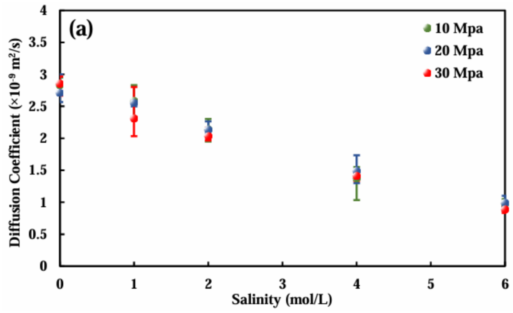

Figure 1-27: The CO_2 diffusion coefficient in a 0 to 6 M NaCl solution at 310 K and pressures of 10, 20, and 30 MPa.

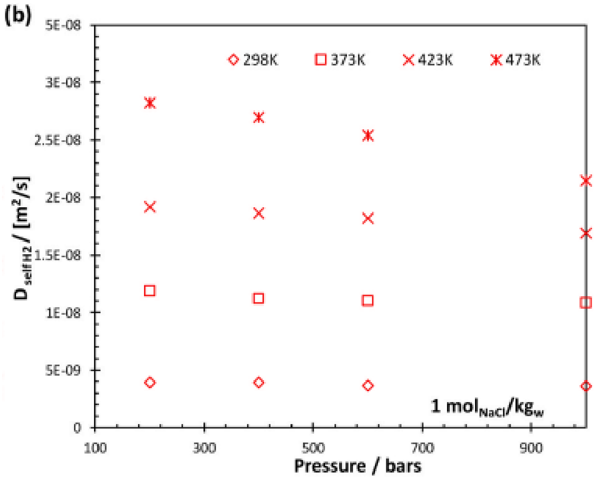

Figure 1-28: H_2 diffusion in water/brine MD simulation data are compiled at various pressures at a single salinity (1 molNaCl/kgw) [Kerkache et al., 2025].

As for the case of H_2, the solvent's structure around it becomes somewhat more organized with increasing pressure, which causes the H_2 self-diffusion coefficient to slightly drop as shown in Figure 1-28 [**Kerkache et al., 2025**].

As a ballpark, most tests show CO_2 diffusion in water on the order of 10^{-9} to 10^{-8} m²/s for reservoir conditions [**Shi et al., 2018**]. Hydrogen, being a smaller molecule, diffuses more swiftly. According to statistics from the USGS PHREEQC database, the diffusion coefficient of H_2 in pure water at 25 °C is around 5.13×10^{-9} m²/s, while that of CH_4 is 1.85×10^{-9}m²/s [**Hemme & Van Berk, 2018**]. That indicates hydrogen diffuses ~3 times faster than methane in water. The diffusivity of H_2 in air at NTP is around 6.1×10^{-5} m²/s [**Miocic et al., 2023**], while that of CO_2 is approximately 1.6×10^{-5} m²/s [**Marrero & Mason, 1972**]. Since diffusion is substantially accelerated by temperature, one may observe about twice as much diffusivity at 50 °C as at 20 °C because according to the equation (1.10) of Wilke-Lee, the diffusivity is proportional to $T^{1.5}$ for gases. The converse is true for salinity: dissolved salts make water more viscous and supply ions that interact with diffusing gas molecules, which marginally lowers gas diffusivity [**Polat et al., 2024].** For example, the common-ion effect causes CO_2 to diffuse a little more slowly in brine than in pure water [**Ma et al., 2019**]. In conclusion, if all else is equal, higher temperature results in faster diffusion and it has more effect on the diffusion than salinity and pressure. When predicting the diffusion of CO_2 or H_2 under the conditions of a particular reservoir, these considerations need to be taken into consideration. Particularly for hydrogen, its limited solubility in brine—only a little quantity of H_2 dissolves to take part in diffusive transport—partially offsets its high diffusivity. Diffusion of CO_2 and H_2 is generally very slow in subsurface settings, but knowing the exact rate in-situ is crucial for forecasting long-term mixing, plume evolution, or any sluggish escape through caprock.

1.4 Caprock Integrity and Leakage Mechanisms

1.4.1 Potential Leakage Pathways

Flow up defective wellbores, migration across faults or fractures, and slow permeation through the pore matrix (advection or diffusion) are examples of possible leakage mechanisms. It is generally accepted that rapid leakage in a well-selected location with intact caprock is more likely to occur through structural vulnerabilities, such as a reactivated fault or an unsealed old well, than through the intact rock matrix [**IEAGHG, 2024**]. If there are no transmissive faults and the caprock stays below its fracture pressure, buoyant gas is confined and there is very little advection. Although it functions on very long periods, diffusive leaking is theoretically possible. For instance, one calculation suggests molecular diffusion of dissolved gas might move on the order of only centimeters into a shale over thousands of years [**Kampman et al., 2016**]. Redox-sensitive mineral dissolution processes and carbonate precipitation slow the reaction front's progression, reducing its penetration into the caprock to about 7 cm in 10^5 years [**Kampman et al., 2016**]. While precipitates may form slightly deeper in, potentially decreasing permeability, some dissolution of carbonate cements or clays may occur at the reservoir interface, possibly enhancing local porosity [**Gaus et al., 2005; Johnson et al., 2004; Liu et al., 2012**]. **Ma et al.'s 2019** geochemical modeling demonstrates these connected effects: K-feldspar and albite dissolution caused CO_2–brine–rock interactions in a Jianghan Basin caprock to increase permeability at the caprock's base by 60% in a 1-D diffusion simulation. However, the model did not take into consideration any healing by mineral precipitation, and the overall caprock permeability remained exceedingly low (still $<10^{-18}$ m^2) and over a period of 5000 years, CO_2 diffused roughly 2.3 meters. These findings point to the worst-case scenario, in which prolonged exposure to CO_2 opens up the rock matrix just enough to allow for the formation of a linked leakage channel. Considering geomechanics, one could anticipate micro-fractures opening if dissolution did weaken the rock, but the evidence to far suggests very little weakening; some studies even suggest that CO_2-induced mineralization could strengthen the caprock [**IEAGHG, 2024**]. For hydrogen, long-term diffusion data are sparse (no million-year natural H_2 accumulations are known). And although there were worries that hydrogen would leak more quickly due to its increased diffusivity, its total loss through diffusion is still anticipated to be negligible over a geologic timescale. According to **Amid et al., 2016**, H_2 losses through diffusion would be less than 0.1% of the stored volume even over extended periods of time. In this project, we will use tNavigator, which is a widely-deployed reservoir simulator to see if its default diffusion implementation can actually capture these sub-percent, sub-centimeter effects under realistic reservoir conditions. In effect, biology could serve as an additional sink limiting H_2 escape, though it might introduce other risks (sulfide corrosion, etc.). This is supported by natural analogues: naturally accumulated CO_2 reservoirs have contained their gas for millions of years, indicating that any diffusive seepage is exceedingly small compared to the trapped volume [**Kampman et al., 2016**]. Therefore, on the scale of project lifetimes (decades to centuries), leakage rates are practically zero with a competent seal, and even over millennia, only negligible amounts of gas would escape by molecular diffusion. Instead, engineering or geomechanical failures (fault slip or well leakage) pose the most leakage risks, which storage projects reduce through careful site selection, injection control, and monitoring [**IEAGHG, 2024**].

1.4.2 Long-Term Performance and Monitoring

Decades of site monitoring show that well-chosen caprocks reliably confine injected gases. At Sleipner, 4-D seismic over 20 years reveals a nine-storey CO_2 plume that has spread laterally within the Utsira Sand yet remains trapped beneath the top seal, with models predicting progressive residual, solubility and eventual mineral trapping [**Bickle et al., 2007; Furre & Eiken, 2017; Furre et al., 2017**]. Elsewhere, a pressure-induced fracture at Krechba (In Salah) caused only minor uplift and was stopped by lowering injection rates [**White et al., 2014; Rucci et al, 2013**], while Austria's Underground Sun Storage pilot found no hydrogen above the caprock [**RAG, 2017**]. Across these projects, sensitive tracers and geochemical sampling detect essentially zero leakage, supporting the view that intact seals permit only negligible diffusion [**Gilfillan, 2017; Weber et al., 2023**]. Consequently, with prudent site selection and ongoing surveillance plus contingency measures such as pressure reduction or well re-sealing, subsurface CO_2 and H_2 can be stored safely and permanently, though regulators still mandate multi-decade monitoring to confirm long-term integrity [**IEAGHG, 2024**].

1.5 Reservoir Simulators

1.5.1 Black-Oil vs. Compositional Models

A crucial technique for forecasting the behavior of injected CO_2 or H_2 in the subsurface is numerical simulation. Black-oil simulators and compositional simulators are the two main categories of reservoir simulations. Black-oil models, which were originally created for the extraction of petroleum, employ a simplified method in which fluids are represented as pseudo-components (oil, gas, and water) with set properties and straightforward dissolution relationships (such as a gas–oil ratio). This method lacks equations of state (EOS) for phase behavior, making it difficult to handle the injection of a new component, such as CO_2, into water or multi-component gas mixtures, such as $H_2/CH_4/CO_2$. In contrast, compositional simulators employ an EOS (like Peng–Robinson) to calculate phase equilibria and fluid characteristics under reservoir conditions while tracking individual components (such H_2, CO_2, CH_4, H_2O, and N_2). Precise CCS and UHS simulations require compositional modeling. for instance, to record CO_2 evaporating into brine, H_2 combining with leftover methane, or exsolving gas. Contemporary simulators that are completely compositional and capable of modeling multi-phase, multi-component systems include Schlumberger's Eclipse 300, CMG's GEM, and tNavigator from RFD. They are ideal for simulating the injection of CO_2 or H_2 into depleted gas fields, since they can accommodate any number of components and phases (gas, aqueous and, where present, residual oil) [**Lekić et al., 2019; Sistan et al., 2018**]. Though the fidelity usually suffers, simpler "black-oil" versions (like Eclipse 100) can be utilized in certain restricted situations (for example, considering CO_2 as an "injected gas" phase with modified PVT tables) [**Dworak & Boukadi, 2024**]. The industry uses compositional simulation for thorough analysis of mixing, trapping, and flow.

1.5.2 Diffusion Implementation in Commercial Simulators

Although it adds numerical overhead, molecular diffusion is critical for long-term or quasi-static problems such as underground-gas storage, hydrogen blending and CO_2 sequestration. Modern compositional simulators therefore let the user activate an extra diffusive-flux term in each component’s mass balance via an input switch. In Eclipse and tNavigator, for example, the flag DIFFUSE switches diffusion on and the engineer supplies one coefficient per component and phase (e.g. DIFFCGAS, DIFFCOIL, DIFFCWAT for gas, oil and water respectively). These scalar values are treated as effective Fick diffusivities and multiplied internally by the concentration gradient. Because advection dominates most production-time forecasts, the default in many commercial packages is “diffusion off”, which can severely under-predict centuries-long gas mixing or the slow dissolution of a CO_2 plume; explicit activation is therefore mandatory for storage studies [**Rock Flow Dynamics, 2024**].For interactions between phases, tNavigator implements a dedicated cross-phase module: coefficients such as DIFFCWG (gas ↔ water) and DIFFCOG / DIFFCGO (oil ↔ gas) describe Fickian transfer across the interface (Figure 1-29).

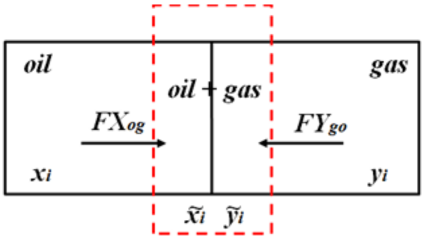

Figure 1-29: Cross-phase diffusion [Rock Flow Dynamics, 2024].

where:

- x_i: oil mole fraction of component i.
- y_i: gas mole fraction of component i.
- $\tilde{x}_i$: oil mole fraction in buffer zone.
- $\tilde{y}_i$: gas mole fraction in buffer zone.
- FX_{og}: flow of the component i from the block I to the buffer zone within the oil phase.
- FY_{og}: flow of the component i from the block J to the buffer zone within the gas phase.

Internally the code builds a thin buffer zone at each oil–gas or gas–water contact and applies the same concentration-gradient law, so no additional modelling effort is required. Note that cross-phase diffusion is handled only in the Fickian form; even when a more advanced formulation is chosen for the individual phases, the interface fluxes remain concentration-driven. A smaller group of simulators can solve the full Maxwell–Stefan (chemical-potential) formulation, which accounts for non-ideal thermodynamics and cross-coupling between species. tNavigator 24.3, for instance, switches to this rigorous treatment in the hydrocarbon phases when the user replaces the Fick blocks with DIFFAGAS / DIFFAOIL (or ticks Chemical Potential diffusion in the GUI); the water and cross-phase terms stay Fickian. The algorithm originally proposed by **Hoteit & Firoozabadi, 2006** demonstrated sharper and more realistic compositional profiles during miscible-gas injection, but commercial uptake is still limited because the method requires a full binary-diffusion matrix and adds Jacobian terms. Where Maxwell–Stefan is unavailable—or where only the gas phase requires it—practitioners often calibrate Fick coefficients to mimic multicomponent effects; for example, assigning hydrogen a gas-phase diffusivity one order of magnitude higher than methane captures its preferential migration in a CH_4 cushion [**Piszko et al., 2023**]. Regardless of the formulation, credible long-term forecasts hinge on realistic D_{eff} estimates derived from laboratory or field tracer data and, whenever possible, validation against observed mixing rates.

1.5.3 Specialized CO_2 Storage Options

Vendors have created CCS-specific modules and keyword options in recognition of the unique requirements of CO_2 storage. The CO2STORE option from Schlumberger's Eclipse, which was initially an Eclipse 300 version, is specifically made for two-phase CO_2–brine systems. The CO2STORE option in the ECLIPSE simulation program was applied in the Illinois Basin-Decatur Project model to replicate the real-world carbon dioxide injection into the reservoir. When CO2STORE is in operation, the simulator can handle storage-related mineral precipitation reactions and incorporates CO_2 dissolving in water and water vaporization into CO_2. Actually, up to 13 components can be used with the CO2STORE module: the primary gas and liquid components, H_2O and CO_2, as well as ions like Na^+, Cl^-, HCO_3^-, and others, and mineral solids (salt, calcite) to record geochemical changes. Reaction equations for carbonate precipitation and brine salting-out are included into it. The SACS/CO2STORE JIP lessons learned at Sleipner and other locations were used to build this functionality. If there is an oil phase in Eclipse, the CO2STORE option can also be used to activate the CO2SOL option, which allows CO_2 to dissolve in oil. tNavigator offers a more general mechanism: the GASSOL + SOLUHENRY pair. GASSOL activates three-phase (gas/oil/water) vapour–liquid–aqueous equilibrium, while SOLUHENRY states that gas solubility in water follows Henry's law:

$$f = xH \tag{1.22}$$

$$lnH = lnH^0 + \frac{v_\infty(P - P_{ref})}{RT} \tag{1.23}$$

where:

- f: fugacity
- x: mole fraction in water
- H: Henry's constant
- R: gas constant
- v_∞: partial molar volume of water at infinite dilution.

The default values for H^0 and v_∞ come from the Li & Nghiem correlation, but they can be overridden by a SOLUBILI table or tuned to match laboratory data. Compared with CO2SOL, and CO2STORE, the GASSOL+SOLUHENRY route lets multiple gases (e.g., CO_2, C_1, H_2, N_2) dissolve simultaneously with a modest set of parameters, making it attractive for large models where computational economy matters [**Dworak & Boukadi, 2024**]. Similarly, tNavigator has incorporated these features: it provides activity coefficient models for brine–CO_2 as well as oil-CO_2 mixes and supports the usage of the previous keywords [**Rock Flow Dynamics, 2024**]. By integrating the established physics (density, viscosity correlations, Henry's law, etc.) for CO_2-water systems, these tools effectively offer a simplified method of simulating CO_2 storage without having to manually build an entire geochemical model. CO2STORE, for instance, can be used to model the amount of

CO_2 that dissolves into the aqueous phase over time and the effects that this has on fluid density and trapping [**Dworak and Boukadi, 2024**]. The Table 1-2 below summarizes the CO_2 options that can be implemented in the model using tNavigator.

Table 1-2: CO_2 options implemented in tNavigator [Rock Flow Dynamics, 2024].

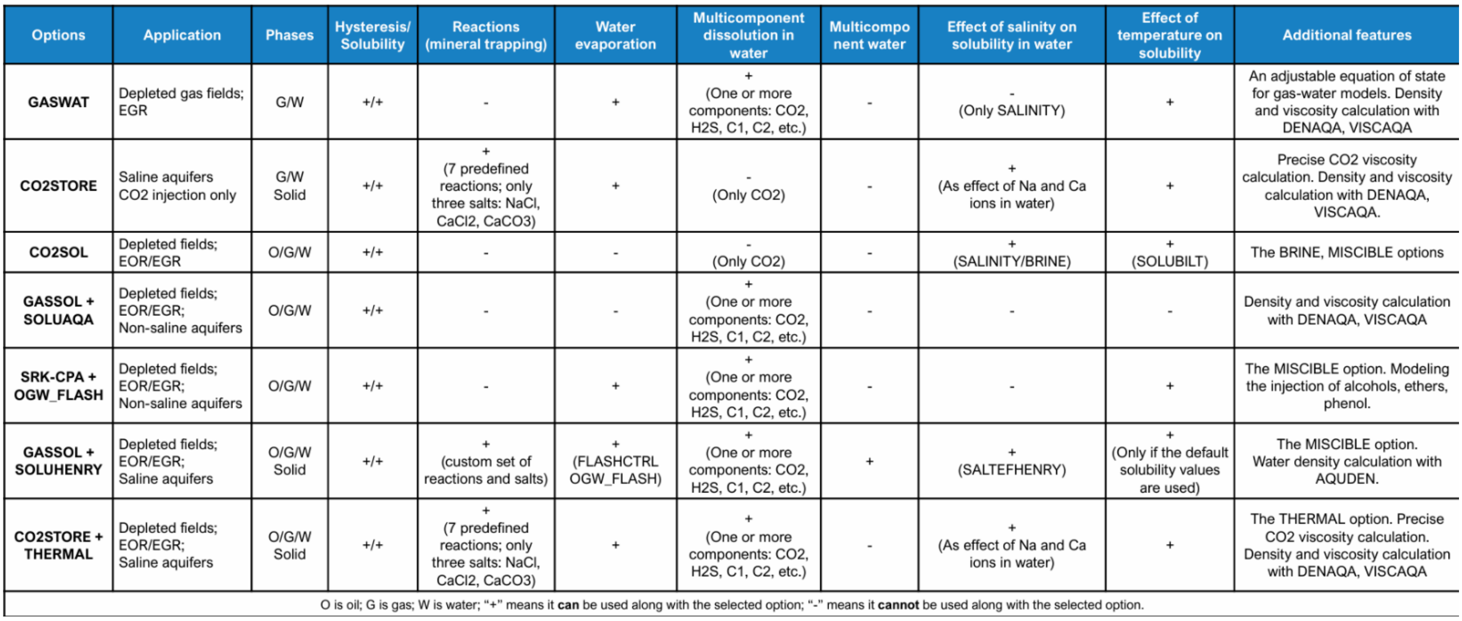

Options	Application	Phases	Hysteresis/ Solubility	Reactions (mineral trapping)	Water evaporation	Multicomponent dissolution in water	Multicomponent water	Effect of salinity on solubility in water	Effect of temperature on solubility	Additional features
GASWAT	Depleted gas fields; EGR	G/W	+/+	-	+	+ (One or more components: CO2, H2S, C1, C2, etc.)	-	- (Only SALINITY)	+	An adjustable equation of state for gas-water models. Density and viscosity calculation with DENAQA, VISCAQA
CO2STORE	Saline aquifers CO2 injection only	G/W Solid	+/+	+ (7 predefined reactions; only three salts: NaCl, CaCl2, CaCO3)	+	- (Only CO2)	-	+ (As effect of Na and Ca ions in water)	+	Precise CO2 viscosity calculation. Density and viscosity calculation with DENAQA, VISCAQA.
CO2SOL	Depleted fields; EOR/EGR	O/G/W	+/+	-	-	- (Only CO2)	-	+ (SALINITY/BRINE)	+ (SOLUBILT)	The BRINE, MISCIBLE options
GASSOL + SOLUAQA	Depleted fields; EOR/EGR; Non-saline aquifers	O/G/W	+/+	-	-	+ (One or more components: CO2, H2S, C1, C2, etc.)	-	-	-	Density and viscosity calculation with DENAQA, VISCAQA
SRK-CPA + OGW_FLASH	Depleted fields; EOR/EGR; Non-saline aquifers	O/G/W	+/+	-	+	+ (One or more components: CO2, H2S, C1, C2, etc.)	-	-	+	The MISCIBLE option. Modeling the injection of alcohols, ethers, phenol.
GASSOL + SOLUHENRY	Depleted fields; EOR/EGR; Saline aquifers	O/G/W Solid	+/+	+ (custom set of reactions and salts)	+ (FLASHCTRL OGW_FLASH)	+ (One or more components: CO2, H2S, C1, C2, etc.)	+	+ (SALTEFHENRY)	+ (Only if the default solubility values are used)	The MISCIBLE option. Water density calculation with AQUDEN.
CO2STORE + THERMAL	Depleted fields; EOR/EGR; Saline aquifers	O/G/W Solid	+/+	+ (7 predefined reactions; only three salts: NaCl, CaCl2, CaCO3)	+	+ (One or more components: CO2, H2S, C1, C2, etc.)	-	+ (As effect of Na and Ca ions in water)	+	The THERMAL option. Precise CO2 viscosity calculation. Density and viscosity calculation with DENAQA, VISCAQA

O is oil; G is gas; W is water; "+" means it **can** be used along with the selected option; "-" means it **cannot** be used along with the selected option.

1.5.4 Simulator Handling of CO_2 vs. H_2

The field of simulating CO_2 storage is generally better developed; several studies have compared several simulators (Eclipse, GEM, TOUGH2, tNavigator) on CO_2 injection scenarios [**Nassan et al., 2022**]. Although they differ in how they handle dissolution and convective mixing, they generally concur on the main findings. Simulations of hydrogen storage are becoming more popular; by include H_2 as a component with the correct EOS characteristics (critical properties, interaction coefficients), simulators can depict H_2. The necessity of taking cushion gas and compressibility into account is a significant distinction. With H_2 as the working gas, many H_2 storage studies make the assumption that a cushion gas (such as natural gas or N_2) is left in the reservoir to maintain pressure. This results in phenomena of gas mixing. Using CMG-GEM, **Kanaani et al., 2022** demonstrated that while employing CO_2 as a cushion gas can lower expenses, CO_2 and H_2 will partially mix due to diffusion and dispersion. Such results highlight that simulator must accurately model multi-component gas mixing – something compositional models do inherently, but proper diffusion/dispersion coefficients must be provided. One challenge is that diffusion-driven processes often require very fine grids or long run-times to simulate millennia. Some researchers use upscaled diffusion or focus on shorter periods (hundreds of years) and then analytically extrapolate the diffusive spread. Another challenge is coupling geochemistry and geomechanics. Fully coupling a reactive transport code (like PHREEQC or

TOUGHREACT) with reservoir simulators is an area of ongoing work. For now, a common approach is to do sequential modelling: first run a flow simulation (with diffusion) to get fluxes, then input those to a geochemical model to assess mineral changes. Integration of geochemical reactions into flow is still limited. Likewise, modelling stress changes (from pressure or temperature effects) in tandem with fluid flow is possible in some simulators (e.g. Eclipse has a GEO coupling, CMG has a geomech module), but it's computationally heavy and not routine for most storage studies. As an example of current capability, the IFP's Coupled THCM model, 2019 [**Ma et al., 2019**] simulated CO_2 diffusion into a caprock with geochemical reactions and found modest changes in permeability as discussed earlier. Overall, the available simulation tools (Eclipse, tNavigator, GEM, TOUGH2, etc.) are capable of modelling the key processes in CO_2 and H_2 storage, but careful input data (diffusion coefficients, reaction rates) and sometimes reduced-order modeling are needed to bridge the gap between lab/field scale and simulation scale.

1.6 Current Gaps in the Literature

Even with advancements, there are still a number of significant gaps, particularly with regard to scale-up and long-term concerns. One weakness with CO_2 storage is the inability to accurately forecast seal performance for periods ranging from thousands to millions of years. Even though models and analogs indicate that diffusion-driven leakage is negligible [**Kampman et al., 2016**], proof of containment over very long periods of time is frequently required by legislation. Additional field analog research that looks at old natural CO_2 traps could confirm that our models don't overlook any minute leakage mechanisms. Furthermore, we have few datasets on the interactions of caprock geochemistry, stress, and diffusion in situ across centuries, therefore coupled process modeling needs to be improved. Future lab studies and simulations could focus on how differing mineral compositions affect the degree to which mineralization self-seals a caprock (as shown in **Smith et al., 2012**). Wellbore leakage mitigation is another gap; although it is outside the purview of this assessment, it is mentioned that further research is needed in the fields of cement–CO_2 reactions and H_2 embrittlement of steels to guarantee that wells stay gas-tight [**Bihua et al., 2018**]. The gaps in understanding are greater for underground hydrogen storage. **Pan et al.'s 2021** evaluation emphasized the significant unknowns related to preserving hydrogen purity and managing subsurface interactions. Techniques to manage this (like segregated injection of cushion gas vs. working gas or using membranes at production) are still being studied. Another major gap is the microbial and geochemical fate of H_2**:** hydrogen can be consumed by subsurface microbes, but quantifying this consumption in a real reservoir is challenging. This uncertainty in biological behaviour translates to uncertainty in how much H_2 might effectively be "lost" (converted to other compounds) during storage. Field trials with monitoring of gas composition over time are needed to close this gap. Geochemical reactions unique to H_2 (like reaction with hematite or sulphates in the rock) also need study; these could potentially produce H_2O or H_2S and change porosity.

In summary, the literature calls for additional field-scale experiments and refined modelling in a few key areas: long-term caprock sealing performance (for

CO_2, to satisfy regulators and the public), reactive transport effects of hydrogen (to ensure no show-stoppers like excessive H_2S generation), and operational optimization for hydrogen storage (to maximize deliverability and purity, possibly via new simulation tools or cushion gas strategies). Addressing these gaps will enhance confidence in long-term CO_2 sequestration and enable the scale-up of hydrogen storage to the levels required for the energy transition. The good news is that none of these gaps appear insurmountable – they are being actively researched, and early results are encouraging. For instance, a 2024 study [**Gomez Mendez et al., 2024]** noted that “the primary knowledge gaps...are in maintaining hydrogen purity by controlling mixing and microbial activity” but found that careful site selection and system design can mitigate many of these issues. As more pilot projects come online (e.g. in Europe and Australia for H_2 storage) and CO_2 storage moves into a commercial scale, we can expect rapid advancement in closing these knowledge gaps and confirming the long-term safety and efficacy of subsurface gas storage.

2. Reservoir Model Definition

2.1 Overview of the Modeling Workflow

The dynamic study follows the closed-loop workflow sketched in Figure 2-1. We first build a Cartesian representation of the depleted gas reservoir, caprock and underlying aquifer (11 m × 11 m × 50 m) using uniform 1 m × 1 m × 0.5 m cells. A two-component gas phase (CH_4 plus the injected CO_2 / H_2 mixture) is described with the GERG equation of state, while the solid matrix and any aqueous phase are purposely neglected at this proof-of-concept stage. Multicomponent transport is handled by a fully implicit finite-volume solver that couples Darcy flow with Fickian diffusion to capture composition-driven spreading in both the reservoir and the caprock.

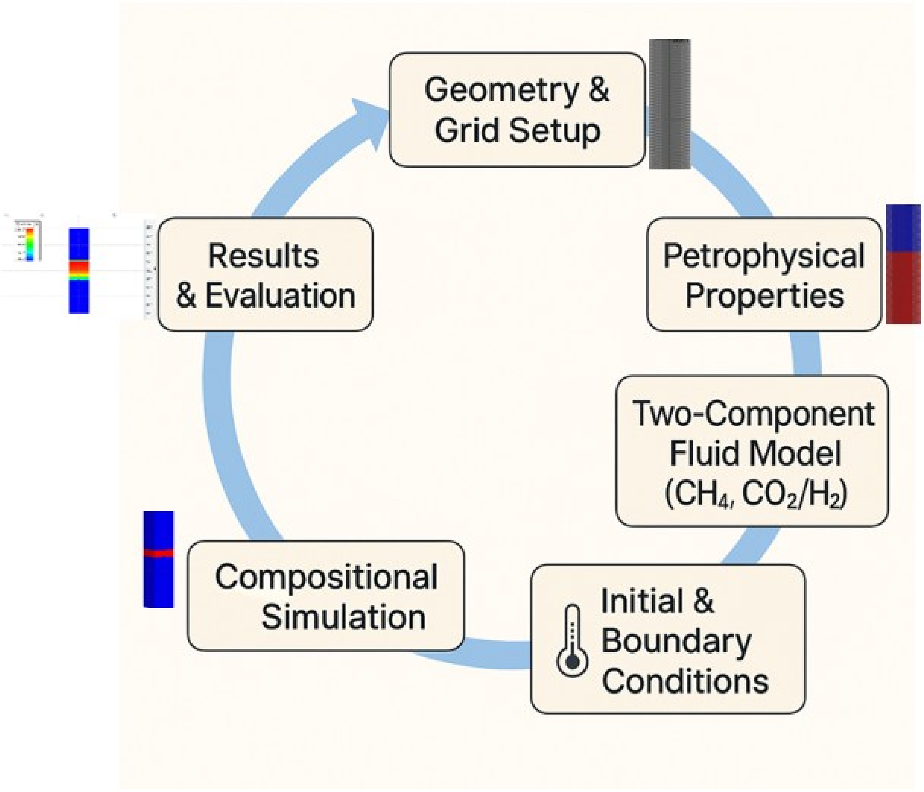

Figure 2-1: Compositional Reservoir-Simulation Workflow (CH_4 + CO_2/H_2 Two-Component Model).

The model is executed in four chronological steps:

1. Equilibrium initialization: hydrostatic pressures of 150 bar at 1500 m TVD and constant temperature of 50 °C.
2. Primary depletion to a target recovery factor of ≈ 70 %, establishing the pre-injection pressure draw-down.
3. Re-pressurization by gas injection (CO_2 / H_2) until the reservoir pressure approaches its original value Pi.

4. Post-injection monitoring, first at monthly timesteps for 10 years to resolve near-well transients, then at six-monthly timesteps for 5000 years to assess long-term plume migration and caprock exposure.

2.2 Grid Design and Petrophysical Properties

This section documents the static framework that underpins every dynamic run: the geometric discretization, the assignment of caprock-reservoir-aquifer regions, and the rock-property constants applied for the base cases and the planned cell-size sensitivity study.

2.2.1 Structural Framework and Layering

The geometric framework is described in Table 2-1 and Figure 2-2.

Table 2-1: Geometric Framework of the Reservoir Model.

Parameter	Value	Rationale
Model shape	Rectangular parallelepiped	Proof-of-concept → minimize structural complexity
External dimensions	11 m × 11 m × 50 m (X × Y × Z)	Matches laboratory-scale diffusion length yet keeps a realistic aspect ratio
Vertical stratigraphy	20 m caprock 10 m reservoir 20 m aquifer	Allows explicit tracking of plume entry into both seal and water leg
Base discretization (Cases A1, A2)	1 m × 1 m × 0.5 m cells → 11 × 11 × 100 ≡ 12 100 cells	Resolves diffusion fronts (~ cm–dm scale) while keeping runtime ≤ minutes
Coarse-grid test (Cases B1, B2)	11 m × 11 m × 0.5 m cells → 1 × 1 × 100 ≡ 100 cells	Quantifies numerical dispersion & global-mass balance sensitivity
Region IDs (k index)	1–40 caprock · 41–60 reservoir · 61–100 aquifer	Used by simulator’s EQLNUM

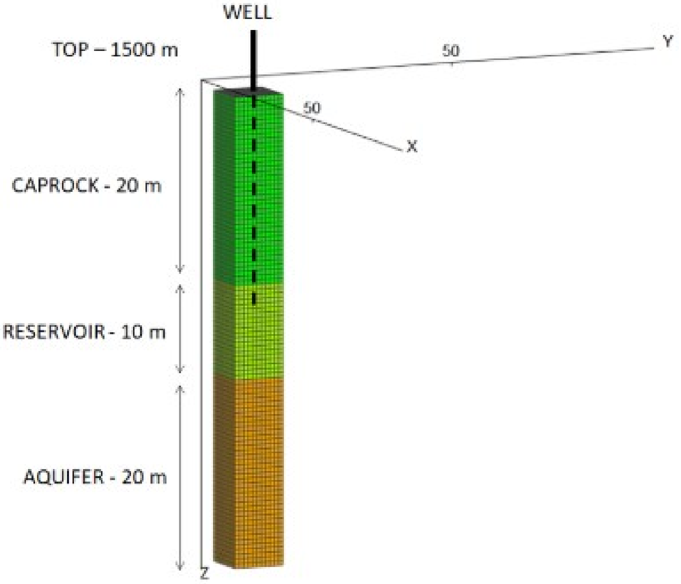

Figure 2-2: Geometric Framework of the Reservoir Model.

2.2.2 Static Properties (Porosity, Permeability, NTG, Facies)

Because the objective is to isolate multicomponent diffusion and EOS-controlled phase behavior, geological heterogeneity is intentionally suppressed in the baseline model. Table 2-2 describes the petrophysical properties of the reservoir. Table 2-3 describes the two equilibration regions:

Table 2-2: Petrophysical Properties of the Reservoir.

Property	Caprock	Reservoir and aquifer	Notes
Porosity (PORO)	0.02	0.2	Constant within each region; no compaction law applied
Permeability along X and Y (PERMXY)	10^{-4} mD	10^{2} mD	$k_x=k_y$
Permeability along Z (PERMZ)	10^{-5} mD	10 mD	Anisotropic medium, vertical permeability is reduced
Net-to-gross (NTG)	1	1	Homogeneous single-facies assumption
Rock compressibility (ROCK)	5 10^{-5} bars^{-1}	5 10^{-5} bars^{-1}	Small but non-zero value captures minor pore-volume expansion and pressure-dependent transmissibility around the 150 bar datum

Table 2-3: Equilibration Number Regions.

ID	Table Name	Datum Depth m	Datum Pressure bars	GWC/WOC Depth m
1	CAPROCK_EQUIL	1500	150	1450
2	RESERVOIR_EQUIL	1520	152.8257	1530

2.2.3 Cell-Size Sensitivity Matrix

To observe grid discretization influence on upward migration into the seal, four cases are pre-defined in the Table 2-4:

Table 2-4: Simulation Grid Cases.

House	Cell size (Δx × Δy × Δz)	Injected fluid*	Purpose
A1	1 m × 1 m × 0.5 m	CO_2	Base case for heavier molecule
A2	1 m × 1 m × 0.5 m	H_2	Base case for lighter molecule
B1	11 m × 11 m × 0.5 m	CO_2	Coarse-grid dispersion test
B2	11 m × 11 m × 0.5 m	H_2	Coarse-grid dispersion test

* CH_4 is present as the native gas in all scenarios; the table lists the injected component used in the re-pressurization stage.

During post-processing we compare:

- cumulative mass of CO_2 and H_2 that has entered the caprock
- vertical concentration profiles after 10 and 200 years
- pressure transient decay.

ASCII arrays for COORD, ZCORN, PORO, and PERMX/Y/Z are supplied in **Appendix 1**. A utility script for automatically generating the alternative cell sizes is listed in **Appendix 2**.

With the static grid and property framework established, Section 2.3 introduces the two-component GERG fluid model (CH_4, CO_2/H_2) that populates this matrix.

2.3 Fluid Characterization and Interaction Modeling

This section documents the two-component compositional description used in every dynamic run. We model only a single gas phase and neglect brine or solid minerals; multicomponent transport is therefore governed solely by the equation-of-state (EOS) and Fickian diffusion.

2.3.1 PVT Data and EOS Regression

describes the PVT properties of the fluids used in the simulation. Because each simulation run now uses pure CO_2 or pure H_2 as the injected gas**,** the model always contains exactly two components at a time.

Table 2-5: PVT properties of the fluids

Symbol	**Description**	**Role in a given run**	**Tc** K	**Pc** **bar**	**Vc** **m³/kg-m**	**Acentric factor**	**Molar mass** **g mol⁻¹**	**Boiling Point** K
CH_4	Methane (native gas)	resident gas	190.56	45.99	9.86 10^{-2}	0.012	16.043	111.67
CO_2	Carbon dioxide	Injected component in the CO_2-injection scenario (A1 B1)	304.19	73.8	9.4 10^{-2}-2	0.228	44.01	194.69
H_2	Hydrogen	Injected component in the H_2-injection scenario (Case A2 B2)	33.18	13.13	6.415 10^{-2}	-0.219	2.016	20.39

The equation of state (EOS) used is GERG-2008, which natively supports CH_4-CO_2 and CH_4-H_2 binary mixtures. Two base instances are actually carried out. Whereas Run-H_2 solely contains methane and hydrogen and no carbon dioxide, Run-CO_2 is made up of methane and carbon dioxide and no hydrogen at all. The GERG-2008 equation of state is employed with its unaltered, published binary-interaction parameters for each binary pair (CH_4–CO_2 or CH_4–H_2). The initial temperature in the reservoir is 50°C and the initial pressure at the datum depth is 152.83bars.

2.3.2 Relative Permeability & Capillary Pressure

At this stage we keep transport strictly diffusive; therefore, the capillary pressure is ignored (Pc=0) to prevent secondary flow mechanisms from masking molecular diffusion effects. Furthermore, a three-phase Corey Relative Permeability curve was used. Tables 2-6 and 2-7 describe the parameters used to draw the Relative Permeability curves in Figure 2-3.

Table 2-6: Water-Oil (Dense CO_2) Relative Permeability Curves data.

Parameter	Symbol / meaning	Value
Minimal water saturation	S_{WL}	0.10
Maximal water saturation	S_{WU}	1.00
Critical water saturation	S_{WCR}	0.10
Residual oil sat. in W–O system	S_{OWCR}	0.00
End-point k_r at S_{WL}	$k_{rOLW} = k_{rOW(SWL)}$	0.60
End-point kr at S_{WCR}	$k_{rORW} = k_{rOW(SWCR)}$	0.60
Connate-water kr	$k_{rWR} = k_{rW}(1 – S_{OWCR} – S_{GL})$	1.00
Maximum-water kr	$k_{rWU} = k_{rW(SWU)}$	1.00
Oil–water capillary pressure at S_{WCR}	$p_{cOW(SWCR)}$	0 bar
Corey exponent (oil curve)	n_{OW}	4
Corey exponent (water curve)	n_W	2
Corey exponent (cap-pressure)	n_{pc}	4
Saturation where $pc \rightarrow 0$	S_{pc} O	–1 (unused)

Note that the Oil phase represents the dense / liquid-like CO_2 phase that may appear during injection (treated as “heavy” component by the simulator). The gas phase includes CH_4 plus any injected phase component (pure CO_2 or pure H_2, depending on the run). Both water-oil and gas-oil branches now have matching end-point mobilities (k_r=0.60), ensuring consistency across phase pairs (Figure 2-3).

Table 2-7: Gas-Oil Relative Permeability Curves data.

Parameter	Symbol / meaning	Value
Minimal gas saturation	S_{GL}	0.00
Maximal gas saturation	S_{GU}	0.90
Critical gas saturation	S_{GCR}	0.15
Residual oil sat. in G–O system	S_{OGCR}	0.00
End-point kr at S_{GL}	$k_{rOLG} = k_{rOG(SGL)}$	0.60
End-point kr at S_{GCR}	$k_{rORG} = k_{rOG(SGCR)}$	0.60
Connate-gas kr	$k_{rGR} = k_{rG}(1 – S_{OGCR} – S_{WL})$	0.60
Maximum-gas kr	$k_{rGU} = k_{rG(SGU)}$	0.60
Oil–gas capillary pressure at connate gas	$p_{cOG}(1 – S_{OGCR} – S_{WL})$	0 bar
Corey exponent (oil curve in G–O system)	n_{OG}	4
Corey exponent (gas curve)	n_G	3

Corey exponent (cap-pressure)	n_{pc}	4
Saturation where *pc* → 0	S_{pc} G	−1 (unused)

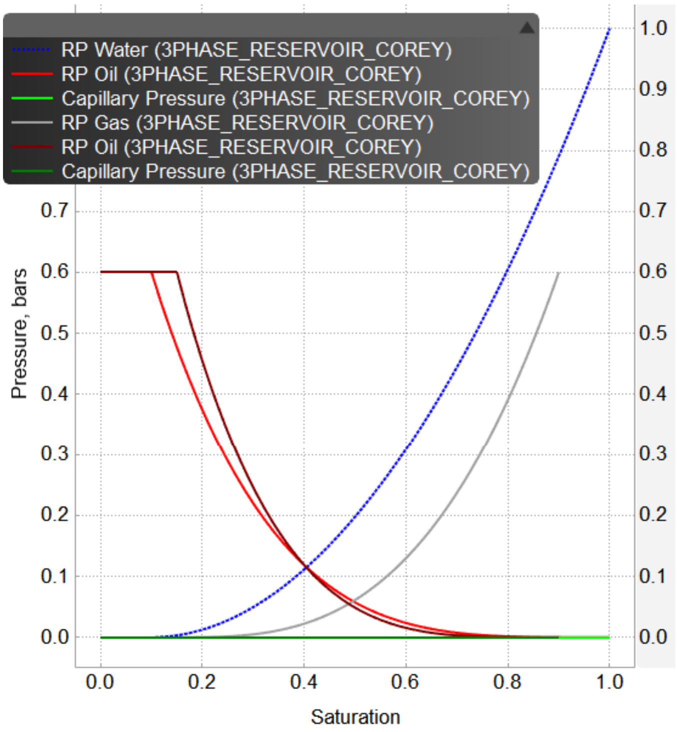

Figure 2-3: Relative Permeability Curves.

2.3.3 Multicomponent Diffusion Data

Diffusion is the main processes we want the model to capture, so we must supply numerical values for the binary-diffusion coefficients. I estimated gas-gas bulk diffusion coefficients with the Wilke-Lee correlation: the method yields sensible, order-of-magnitude results but becomes less reliable as pressure rises (50-150 bars). I therefore evaluated them at 50 bar, which is the pressure to which the reservoir is depleted before injection starts, and at the reservoir temperature of 50 °C. Furthermore, the bulk diffusivities in brine and in the dense CO_2, which was considered an oil phase by the software, were interpolated from literature and here are the results:

a. Bulk Diffusivities in gas phase:

- CO_2 diffusion in CH_4: $D_{AB} = 4.17 \times 10^{-3} cm^2/s$.
- H_2 diffusion in CH_4: $D_{AB} = 0.015516\ cm^2/s$.
- CH_4 self-diffusion: $D_A = 5.47 \times 10^{-3}\ cm^2/s$.

b. Bulk Diffusivities in water phase:

- CO_2 diffusion in H_2O: $D_{AB} = 1.28 \times 10^{-4}\ m^2/day$
- CH_4 diffusion in H_2O:$D_{AB} = 2.5 \times 10^{-4}\ m^2/day$ [**Sachs, 1998**].

- H_2 diffusion in H_2O: $D_{AB} = 5.7024 \times 10^{-4}\ m^2/day$ [**Wang et al., 2023**].

c. Bulk Diffusivities in oil phase (dense CO_2):

- CO_2 self-diffusion: $D_A = 21.92 \times 10^{-8}\ m^2/s$ [**Hulikal Chakrapani et al., 2024**].
- CH_4 diffusion in CO_2: $D_{AB} = 1.6 \times 10^{-8}\ m^2/s$ [**Guevara-Carrion et al., 2019**].
- H_2 diffusion in CO_2: $D_{AB} = 1.31 \times 10^{-6}\ m^2/s$ [**Hulikal Chakrapani et al., 2024**].

Because the reservoir is a porous medium, molecular-scale diffusion coefficients must be converted to effective diffusivities. We do so with Eq. (1.21) in Section 1.3.3, which scales the coefficient by the tortuosity. Using the Bruggeman correlation: $\tau^2 = \phi^{-0.5}$. The reservoir porosity is 0.2. Therefore $\tau^2 = 2.23$ [**Holzer et al., 2023**].

d. Effective Diffusivities in gas phase:

- CO_2 diffusion in CH_4: $D_{AB} = 3.23 \times 10^{-3}\ m^2/day$.
- H_2 diffusion in CH_4: $D_{AB} = 0.012\ m^2/day$.
- CH_4 self-diffusion: $D_A = 4.238 \times 10^{-3}\ m^2/s$.

e. Effective Diffusivities in water phase:

- CO_2 diffusion in H_2O: $D_{AB} = 1.15 \times 10^{-5}\ m^2/day$
- CH_4 diffusion in H_2O:$D_{AB} = 2.242 \times 10^{-5}\ m^2/day$.
- H_2 diffusion in H_2O: $D_{AB} = 5.114 \times 10^{-5}\ m^2/day$.

f. Effective Diffusivities in oil phase (dense CO_2):

- CO_2 self-diffusion: $D_A = 1.698 \times 10^{-3}\ m^2/day$.
- CH_4 diffusion in CO_2: $D_{AB} = 1.24 \times 10^{-4}\ m^2/day$.
- H_2 diffusion in CO_2: $D_{AB} = 0.01\ m^2/day$.

The detailed calculations made to find the gas diffusion coefficients (bulk) can be found in **Appendix 3**.

2.3.4 Gas dissolution in water (GASSOL + SOLUAQA)

To capture the dissolution of injected gas into formation brine, the **GASSOL + SOLUAQA** option set is activated. This option is available for depleted-gas reservoirs and EGR scenarios that contain resident brine, without solid precipitation. Gas dissolution is simulated for CH_4, CO_2 and H_2 via the **SOLUAQA** option, which interpolates the dissolution of components as a function of pressure at fixed temperature. In the current project, tables relative to CH_4 and CO_2 are obtained through numerical simulation of a Compositional Model in tNavigator.

Here the Peng- Robinson EOS and Henry's Law are used to calculate the concentration of the dissolved gas in water at decreasing pressure. The H_2 profile, on the other hand, comes from [**Tawil et al., 2024**].

2.4 Key Assumptions

The working assumptions underlying each run, discussed later in section 2.6, are compiled in this section (Table 2-8). The main sources of uncertainty in the baseline model cluster around four simplifying choices. First, the diffusion: although the Wilke–Lee estimates correlations reproduce experimental data at low pressures (≈ 15 bar), their accuracy deteriorates markedly at typical reservoir conditions around 150 bar. Second, zero capillary pressure: setting $Pc = 0$ cleanly isolates diffusive flux but can exaggerate CO_2 and H_2 breakthrough in very low-permeability seals. Third, two-phase simplification: omitting explicit water and solid phases removes mineral trapping and CH_4 solvation effects that would otherwise retard long-term CO_2 migration, meaning present forecasts represent a deliberate worst-case plume extent. Fourth, uniform rock properties: real-field laminations or anisotropy could either accelerate vertical fingering (high-k streaks) or impede it (tight streaks).

Table 2-8: Key modelling assumptions adopted in the base-case dynamic study.

Category	Adopted assumption	Rationale / expected impact
Geometry and Grid	Rectangular box 11 m × 11 m × 50 m, split into caprock (top 20 m), reservoir (mid 10 m), aquifer (bottom 20 m).	*Minimize structural ambiguity.* The box is large enough to let diffusion fronts develop beyond near-well cells yet keeps run-times < 5 min per case.
	Uniform Cartesian cells 1 m × 1 m × 0.5 m (Cases A1/A2); coarse 11 m × 11 m × 0.5 m (Cases B1/B2).	Resolves cm–dm diffusion length in fine runs and quantifies numerical dispersion in coarse runs.
Rock and Petrophysics	Constant porosity/permeability inside each direction.	Retaining only first-order anisotropy ($kx = ky \gg kz$) mimics sedimentary layering that restricts vertical flow; this slows upward plume migration while keeping the model free of lateral heterogeneity so diffusion effects remain easy to isolate.
	Rock compressibility $cr=5\times10^{-5}$ bar^{-1}	Keeps PV trend realistic over an 80–150 bar cycle without adding geomechanics.
Fluids and Phases	Two-component composition per run: $CH_4 + CO_2$ *or* $CH_4 + H_2$; no explicit water components or precipitated solids	Matches the planned depleted-gas / EGR scenario; water is introduced implicitly only when needed for gas dissolution.

	GERG-2008 EOS with published binary-interaction parameters; no tuning	Provides reliable CH_4-CO_2 and CH_4-H_2 thermodynamics up to 200 bar with full consistency across cases.
	Simulator treats dense CO_2 as an “oil” phase at high density	Accepted as built-in behavior; it merely affects internal phase labels, not mass balance.
Flow and Transport Physics	Darcy advection + Fickian multicomponent diffusion (fully implicit)	Captures composition-driven spreading; necessary to differentiate CO_2 vs H_2 plume growth.

2.5 Model Initialization and Equilibrium set-up

The starting state of every simulation is generated with **EQUIL**, the tNavigator keyword that prescribes pressure equilibrium initialization.

The grid is split into a Gas Zone (cells 41-60), Water Zone above and below, and no Oil Zone at t=0 (a dense-CO_2 “oil” phase can appear later during injection), since $H_{goc} = H_{woc} = -100$ (deactivated) produces a pure gas-water reservoir. The two equilibration regions are defined in Table 2-3 in section 2.2.2. Because CAPROCK_EQUIL and RESERVOIR_EQUIL have different reference pairs (H_{ref},P_{ref}), tNavigator draws two independent hydrostatic lines**,** one inside each equilibration region. For any phase α (gas or water) present in region r, the pressure is:

$$P_{\alpha,r}(z) = P_{DATUM} - (\mathrm{Z} - \mathrm{Z_{DATUM}})\rho_\alpha g \qquad [bar] \qquad (1.24)$$

where:

- $r = 1$: CAPROCK_EQUIL ($Z_{DATUM} = 1500\, m, P_{DATUM} = 150\, bar$).
- $r = 2$: RESERVOIR_EQUIL ($Z_{DATUM} = 1520\, m, P_{DATUM} = 152.826\, bar$).
- ρ_α is taken from the GERG EOS at 50°C (≈ 1000 kg m^{-3} for water, ≈ 106 kg m^{-3} for gas).
- $g = 9.81\, m.s^{-2}$.

Hence the complete pressure field can be written as:

$$P \begin{cases} P_{w,1(z)} & z \leq 1520\ (caprock\ and\ water\ column) \\ P_{g,2}(z) 1520 & < z \leq 1530\ (free - gas\ pay) \\ P_{w,2}(z) & z > 1530\ (aquifer\ water\ column) \end{cases}$$

In the initial pressure profile, a small step (≈ 1–2 bar) appears at 1520 m interface between caprock and reservoir, as observed in Figure 2-4. This discontinuity (observed in real cases) is the consequence of primary migration of gas during the formation of reservoirs. Capillary pressures are zero (P_{COW}=P_{COG}=0), so no further adjustments are made; saturations are assigned directly from the Corey end-point values

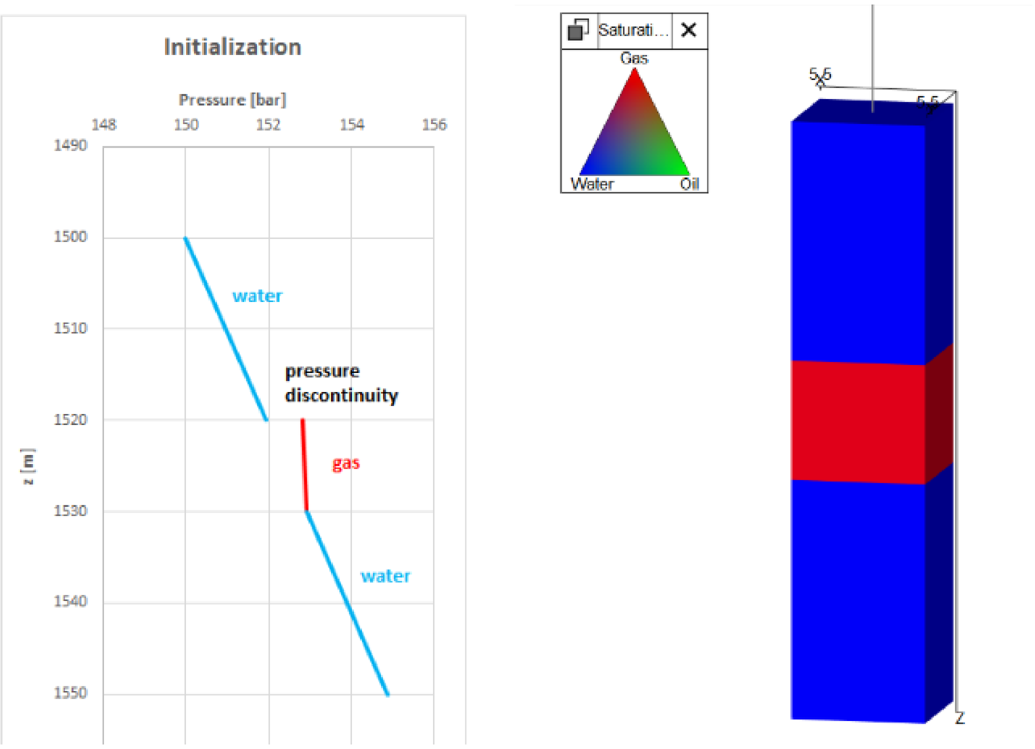

Figure 2-4: Initial hydrostatic state generated by the EQUIL keyword.

2.6 Production History

Two concise tables capture all well-related inputs that are hard-coded into the base-case schedule. Table 2-9 lists the geometric and operational specifications for the injector and producer, whereas Table 2-10 lays out the chronology of controls that drive depletion, conversion, injection, and long-term monitoring.

Table 2-9 : Well configuration and initial controls.

Well	Role	Surface location*	Perforated interval (MD)	Diameter (m)	Skin	Initial status	Control logic
WELL1	Injector (CO_2/ H_2)	model centre (i = 0, j = 0)	1525 – 1530 m	0.16	0	shut-in during depletion	Rate 125 Sm^3 d^{-1} for CO2 and 250 Sm^3 d^{-1} for H2 until BHP constraint is reached (250 bars for CO_2 and 150 bars for H_2)
WELL2	Producer (CH_4)	model centre (i = 0, j = 0)	1522 – 1527 m	0.16	0	open at t = 0	Rate 400 Sm^3 d^{-1} until average BHP 50 bar

							(until 70 % recovery factor) then shut-in

Table 2-10: Chronological schedule of well events.

Phase	Time window	Active well(s)	Target & keyword
Primary depletion	01/16/2025 → 07/15/2025	WELL2 only	**WCONPROD** BHP 50 bar until remaining GIP ≈ 30 %
Shut-in & conversion	07/15/2025→ 12/15/2025	BOTH	**WELOPEN** “SHUT” (WELL2 remains closed thereafter)
Gas injection	12/15/2025 → 12/15/2026	WELL1	**GRAT** 125 Sm^3 d^{-1} CO_2 or 250 Sm^3 H_2 until BHP=250 bar then shut-in
Post-injection monitoring	+5000 yr	NONE (both wells shut)	**TSTEP** 1 month for the first 10 years, 6 months for 200 years and 1 year until the end.

3. Simulation Results

3.1 Fine-grid results

Case A1

At about 150-155 bar, the reservoir column was near a single hydrostatic gradient, as seen in Figure 3-1. Water density fluctuated narrowly around 992.5 kg m^{-3} (Figure 3-6), dissolved-gas levels were minimal (CO_2 Rsw = 0 throughout), and CH_4 was only present as background brine gas with < 2.5 Sm^3 m^{-3} (Figure 3-3). The gas phase was initially at equilibrium. At the end of the observation period (5000 years) a discontinuous pressure profile is observed (Figure 3-2): pressure in Caprock (K= 0-40, 1500-1520 m) has increased to 180-183 bar whereas the reservoir and aquifer (K = 41–100, > 1520 m) have relaxed to 135-140 bar, roughly 15 bar below the initial gradient. Such a pressure distribution needs further investigations. 50–52 mol% of the free gas reached the structural crest and it is still made up of CO_2 gas molecular fraction (K ≈ 41-49; Figure 3-8). Above K=40, no mobile CO_2 is found, indicating structural and residual entrapment. The cumulative mass of CO_2 injected in the reservoir is 94324.1 kg , of which 21784 kg has diffused in the caprock and aquifer: approximately 99% diffused in the below formation (Figure 3-10), and a negligible quantity reached the overlying one (Figure 3-9). Furthermore, CO_2 has migrated about 3 m into the seal (6th layer of the caprock) in the fine grid run, in accordance with previous research, where CO_2 diffused roughly 2.3 meters in a Jianghan Basin caprock [Ma et. Al., 2019] (without taking into consideration any healing by mineral precipitation). In the lower aquifer, CO_2 dissolution raises the brine density from 992.5 to 1004 kg m^{-3} (Figure 3-7). The smoothed Rsw profile between K= 60 and 80 can be explained by slow convection triggered by the 1% density contrast between fluids. Figure 3-4 shows the vertical distribution of dissolved CO_2 after 5 000 years. Concentrations rise from < 0.1 sm^3 m^{-3} in the cap-rock to a peak of ≈ 26 sm^3 m^{-3} in the lower aquifer (K ≈ 70–90), then decline as the plume tail mixes. The shape of the curve confirms three distinct regimes:

- ✓ Diffusion-only in the overburden (flat, very low Rsw)
- ✓ Interface-controlled dissolution in the reservoir interval (moderate Rsw, yellow triangles)
- ✓ Convection-enhanced dissolution in the deep aquifer (steep red limb).

Figure 3-5 plots the CH_4 solubility. CO_2 invasion has displaced methane from the aquifer upward into the cap-rock brine, creating a weak CH_4 crest (2.3 Sm^3 m^{-3} at K ≈ 5). Deeper in the aquifer the CH_4 profile now mirrors the CO_2 curve but at an order-of-magnitude lower level (0.9–1.6 Sm^3 m^{-3}), illustrating competitive dissolution: as brine approaches CO_2 saturation its CH_4 capacity drops. These complementary curves emphasize that CO_2 dominates the aqueous phase wherever it is present, pushing CH_4 toward the overburden and leaving the lower aquifer CO_2-rich.

The density essentially stays the same above K= 40, supporting the very small amount of CO_2 that enters the cap-rock porewater. Table 3-1 describes the CO_2 mass distribution after 5000 years of observation.

Table 3-1: Mass balance and trapping proportions after 5000 years of observation

CO_2 mass distribution after 5 000 years	kg	% of injected mass
Mobile CO_2 gas	71540	75.9 %
Dissolved in aquifer	21700	23.0 %
Dissolved in caprock	84.9	0.09 %
Total	93324	99.0 %

The 1 % discrepancy is numerical rounding.

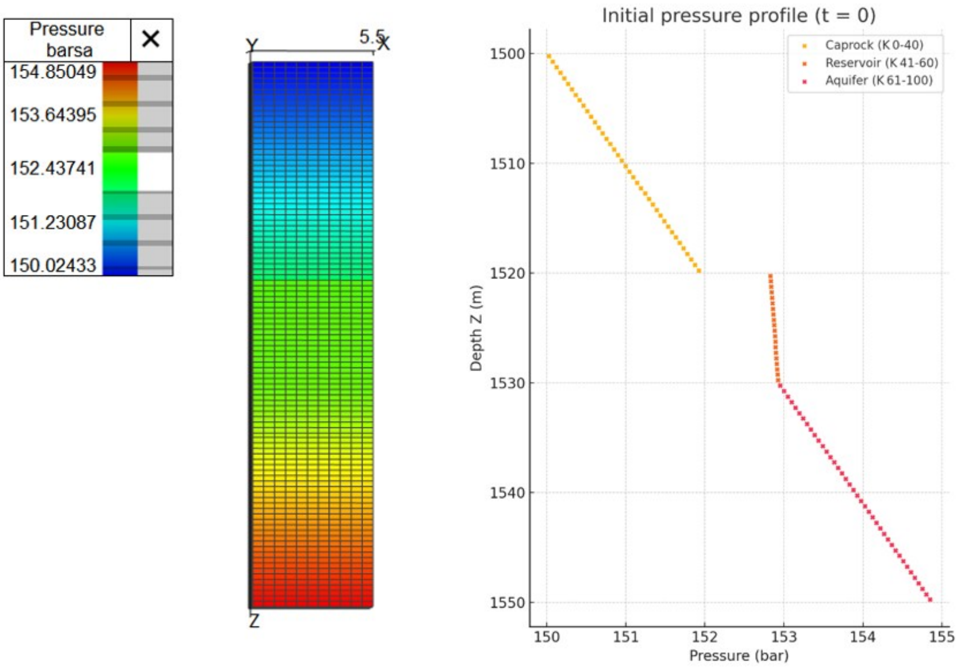

Figure 3-1: Initial pressure profile for all cases.

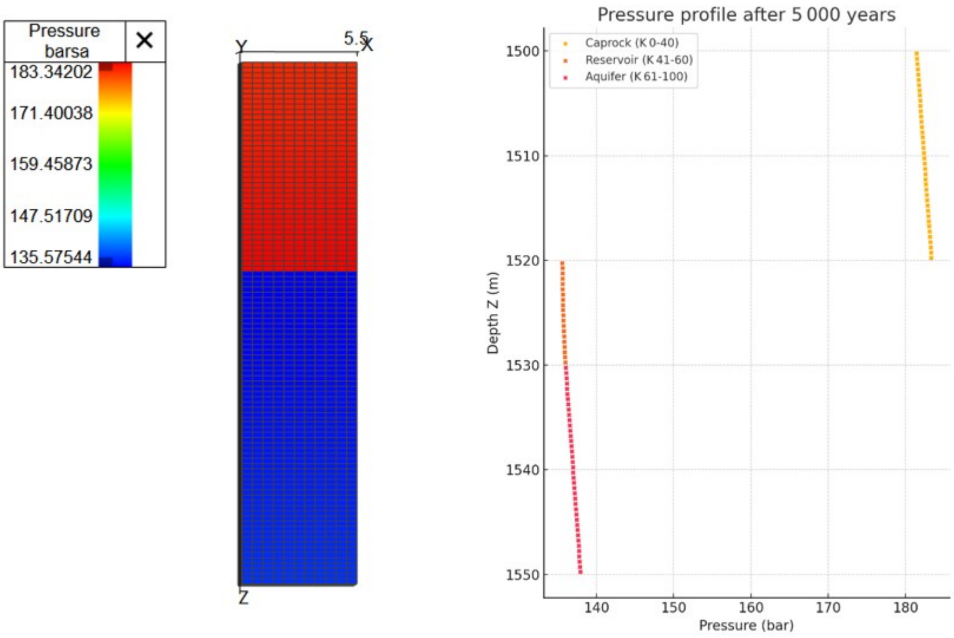

Figure 3-2: Pressure profile after 5000 years of observation.

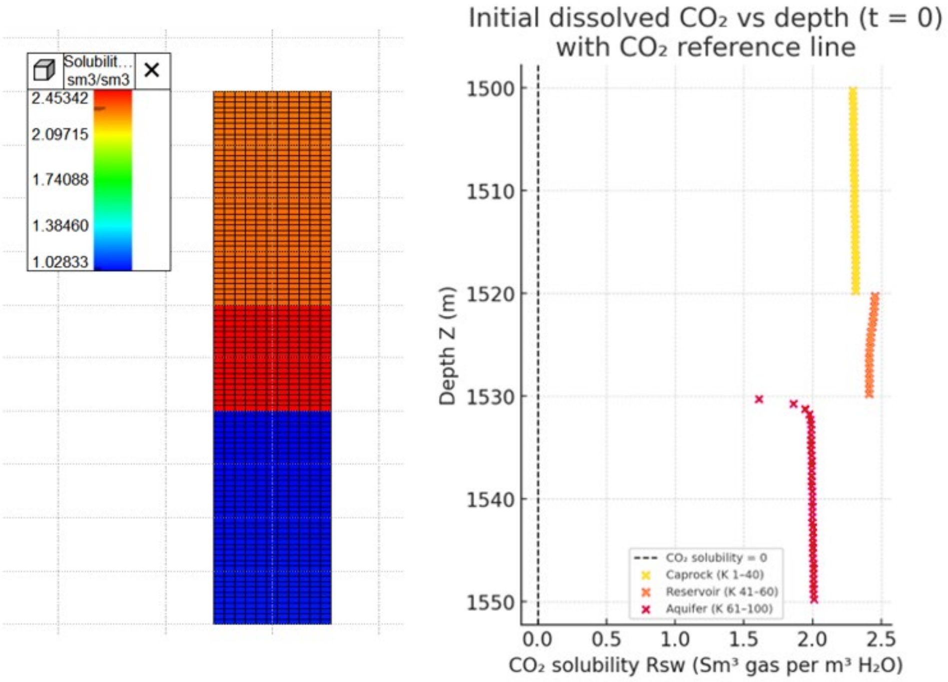

Figure 3-3: Initial gas dissolved in water vs depth (by filtering i=j=6).

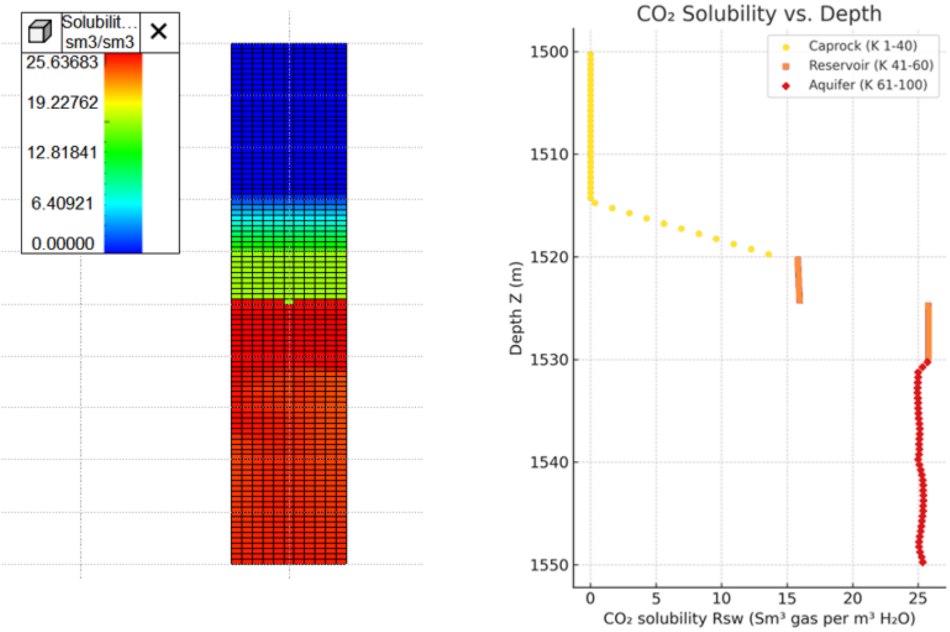

Figure 3-4: CO_2 solubility in water after 5000 years of observation (by filtering i=j=6).

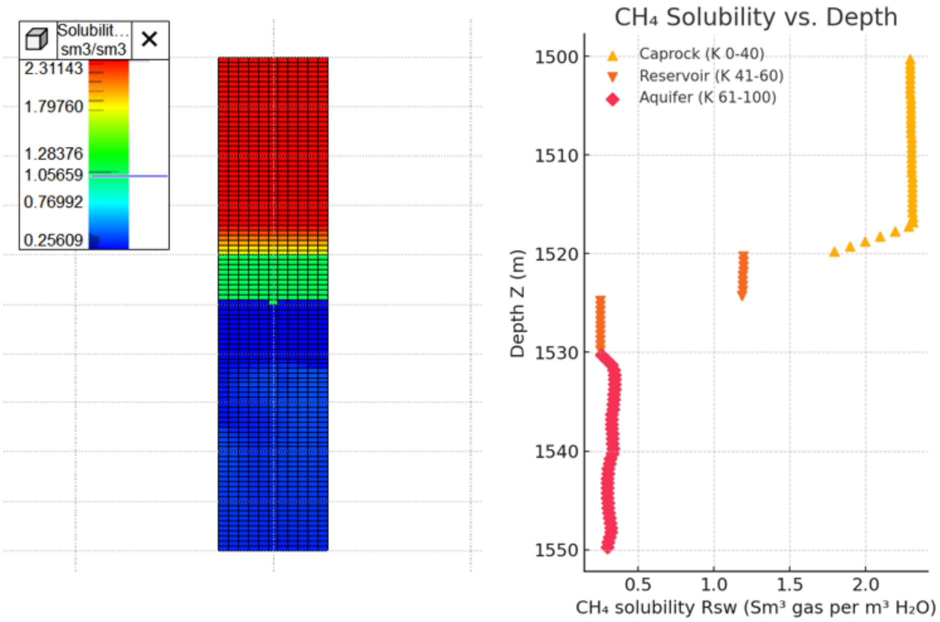

Figure 3-5: CH_4 solubility in water after 5000 years of observation (by filtering i=j=6).

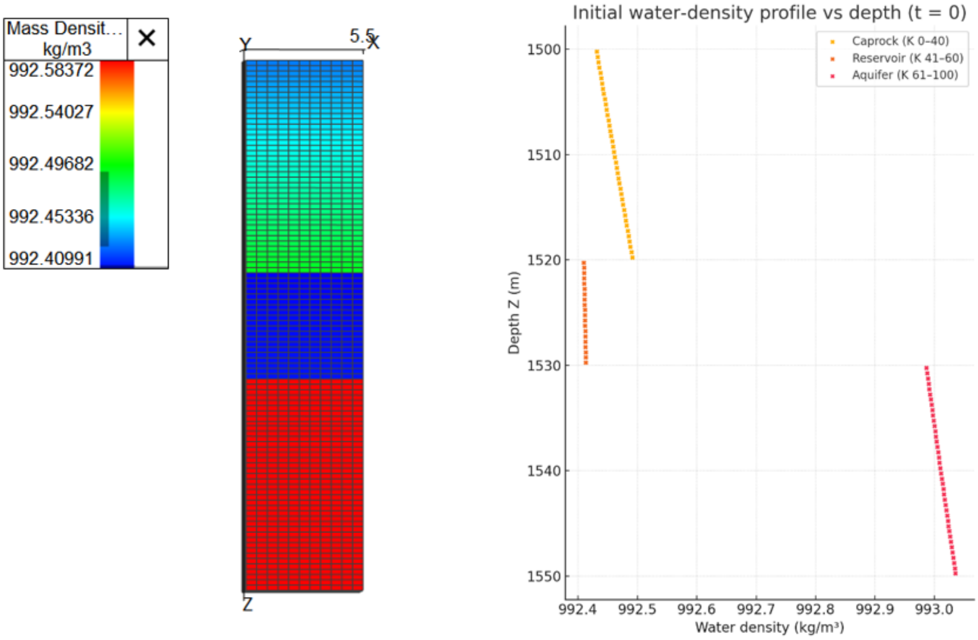

Figure 3-6: Initial water mass density profile for all cases.

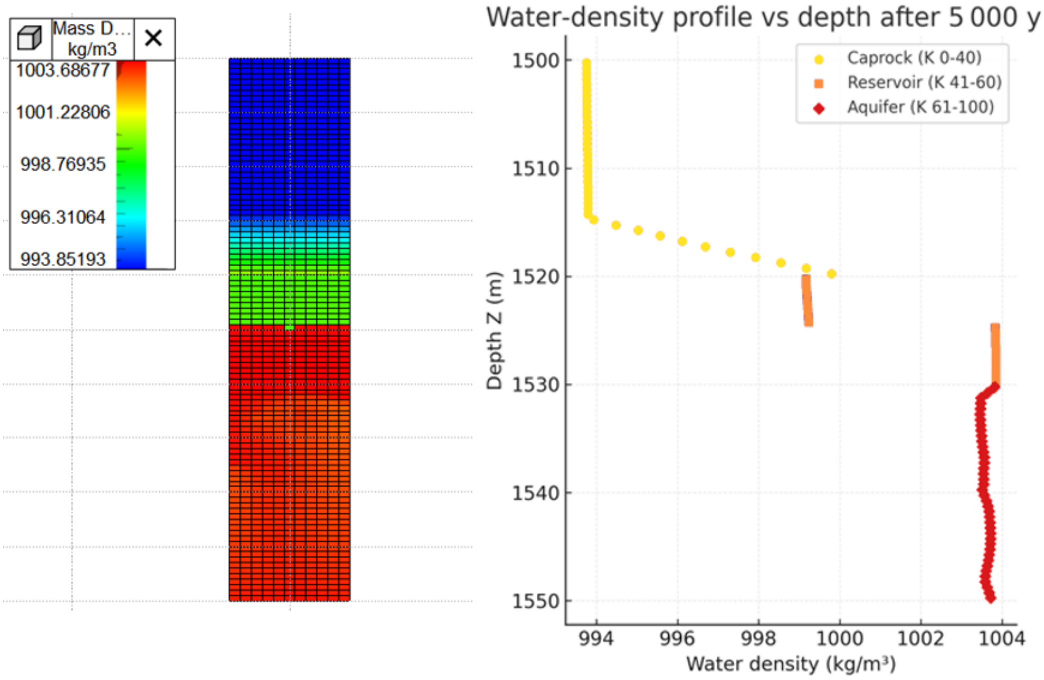

Figure 3-7: Water mass density profile after 5000 years (by filtering i=j=6).

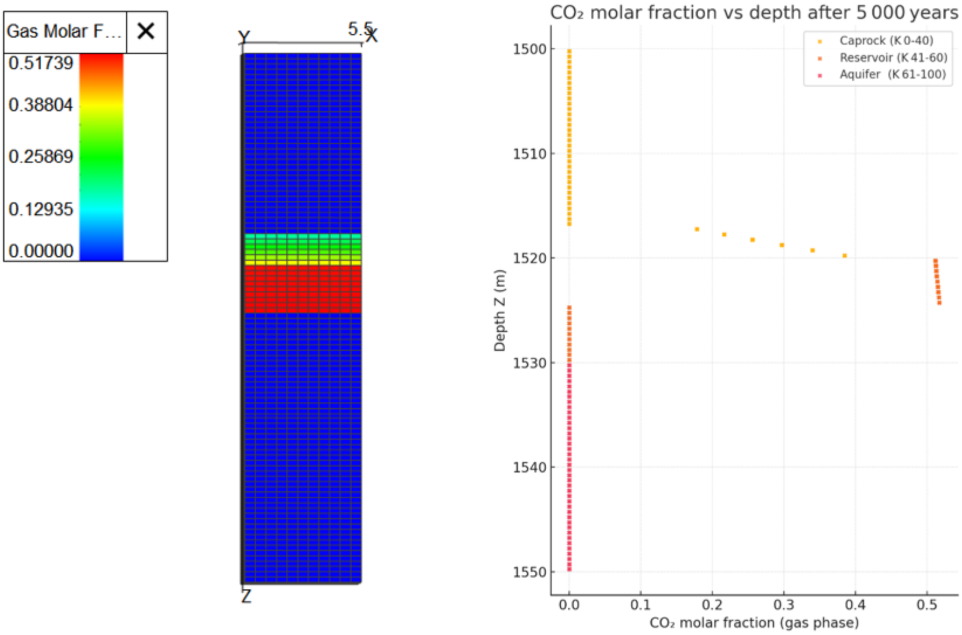

Figure 3-8: CO_2 gas molar fraction vs depth after 5000 years of observation.

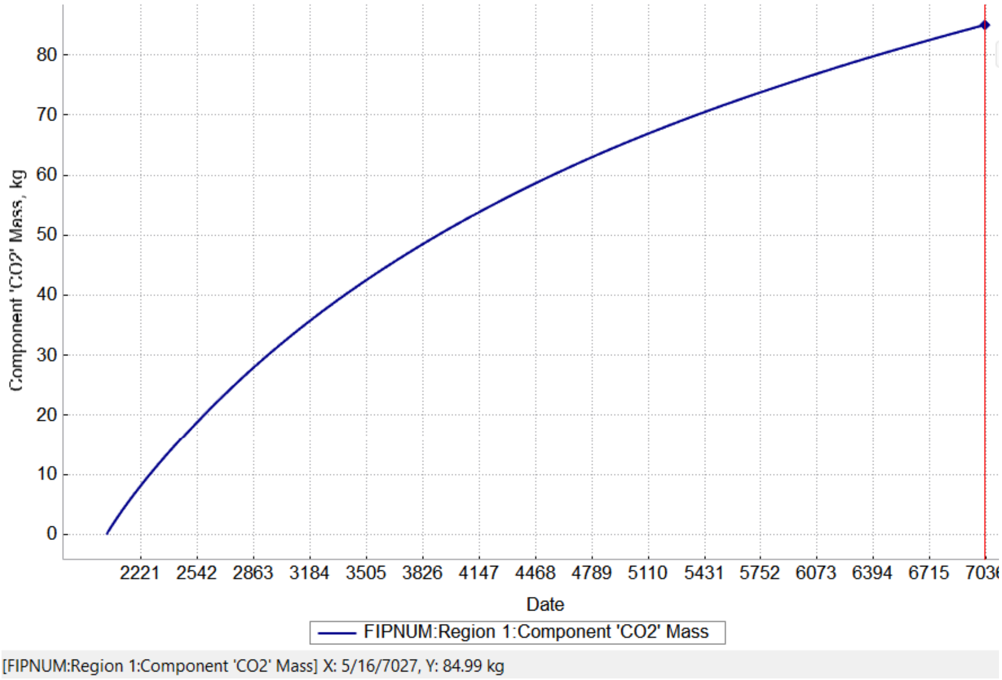

[FIPNUM:Region 1:Component 'CO2' Mass] X: 5/16/7027, Y: 84.99 kg

Figure 3-9: Mass of diffused CO_2 in the caprock after 5000 years of observation.

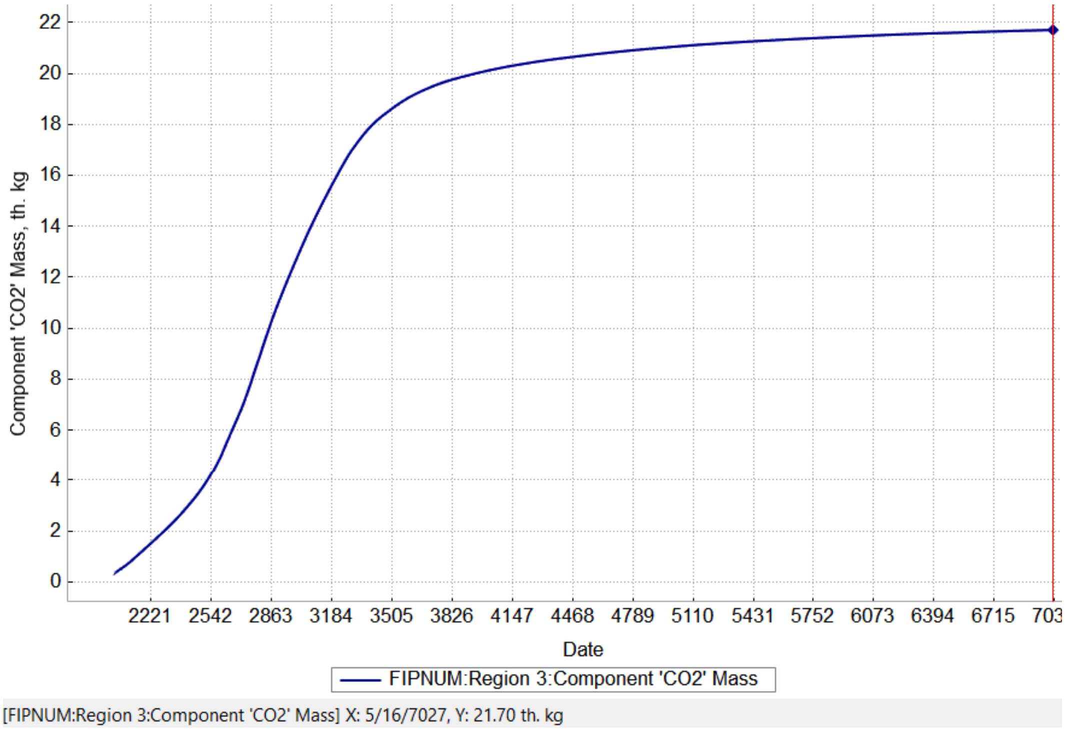

[FIPNUM:Region 3:Component 'CO2' Mass] X: 5/16/7027, Y: 21.70 th. kg

Figure 3-10: Mass of CO2 diffused in the aquifer after 5000 years of observation.

Case A2

In comparison to the initial hydrostatic trend (150–155 bar) (Figure 3-1), the H_2 storage interval five millennia following shut-in only exhibits a slight over-pressure (~152.2 bar). The underlying aquifer has somewhat softened to about 154 bar, while the cap-rock is still near its pre-injection gradient. Safe containment is confirmed by these gradients (Figure 3-11).

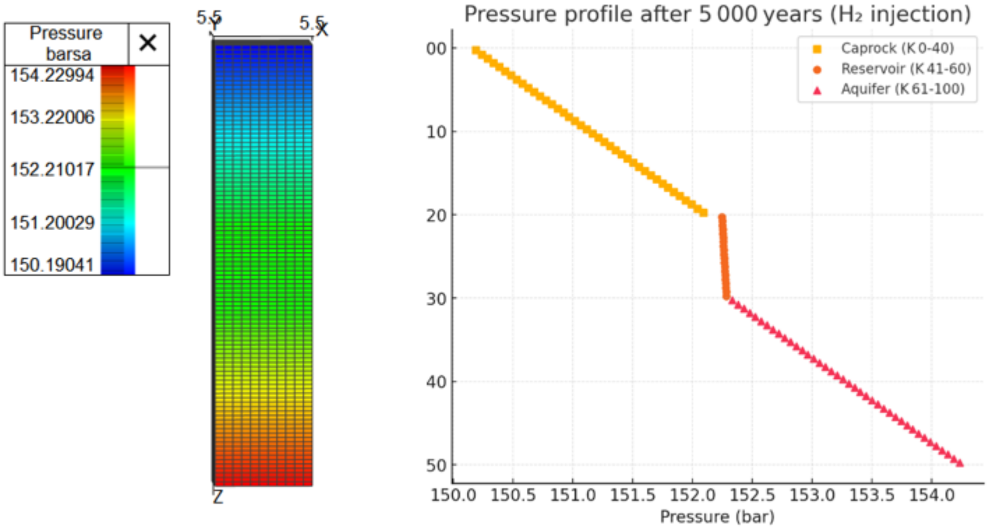

Figure 3-11: Pressure profile after 5000 years of observation.

H_2 R_{sw} peaks in the top aquifer (K ≈ 65–80) at 1.8 $Sm^3\ m^{-3}$ and decreases to $\lesssim$ 0.5 $Sm^3\ m^{-3}$ at deeper depths. The cap-rock records R_{sw} = 0.60429 in the first layer (Figure 3-12) and the reservoir's dissolved gas is limited to a small vertical band.

CO_2, on the other hand, reached 6.92712 $Sm^3\ m^{-3}$ in the sixth cap-rock layer and 26 $Sm^3\ m^{-3}$ in the deep aquifer (Figure 3-4).

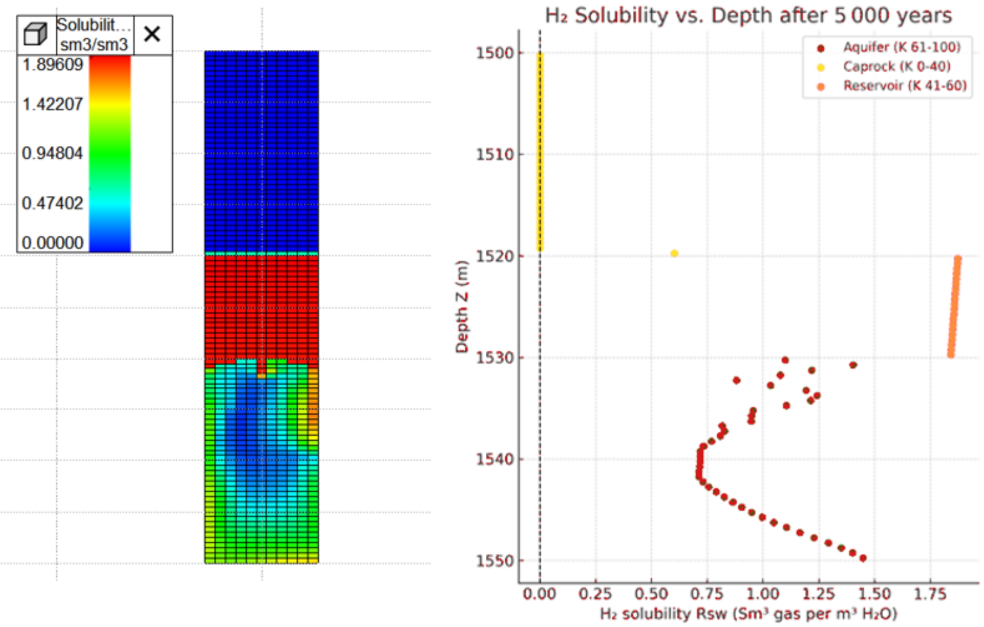

Figure 3-12: H_2 solubility in water after 5000 years of observation (by filtering i=j=6).

Initially the entire water column lay in a tight band of ≈ 992.40–992.58 kg m^{-3} (Figure 3-6). Five millennia after H_2 injection the cap-rock is essentially unchanged at ≈ 992.4–992.6 kg m^{-3}, but the underlying reservoir–aquifer system has densified: the reservoir clusters around ≈ 993.6 kg m^{-3}, while the aquifer now reads ≈ 993.1–993.7 kg m^{-3}, a rise of roughly +0.7–1.3 kg m^{-3} relative to the start (Figure 3-14). This densification is attributed to the back-dissolution of native CH_4, which increases brine density upon dissolution, whereas the modest amount of dissolved H_2 exerts only a minor counter-effect. Figure 3-13 fits in well with the density discussed above and combines the CH_4-solubility map (left) with its depth-profile (right).

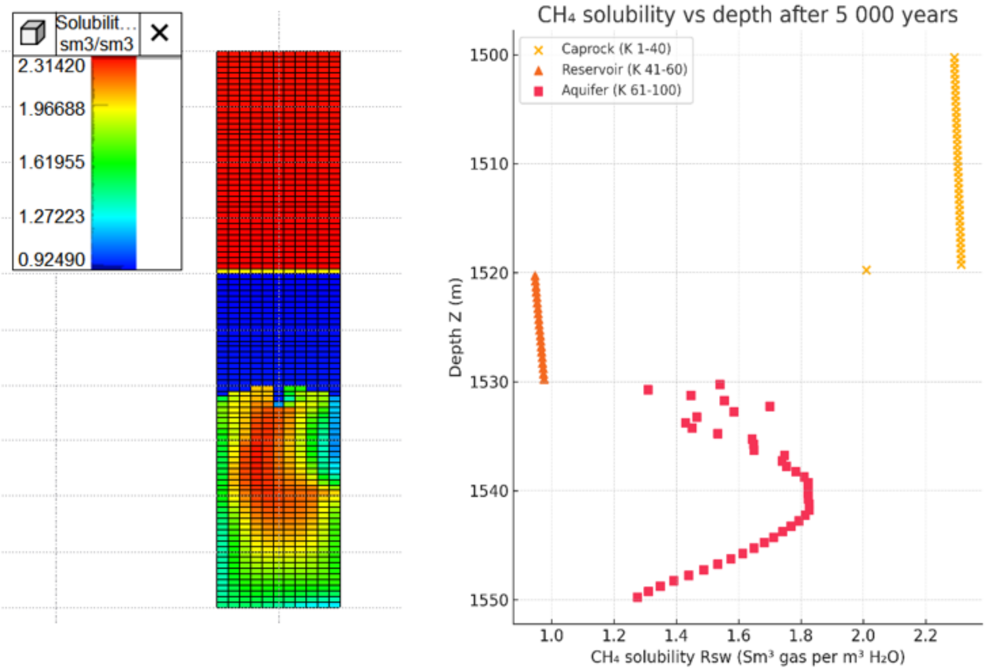

Figure 3-13: CH_4 solubility in water after 5000 years of observation (by filtering i=j=6).

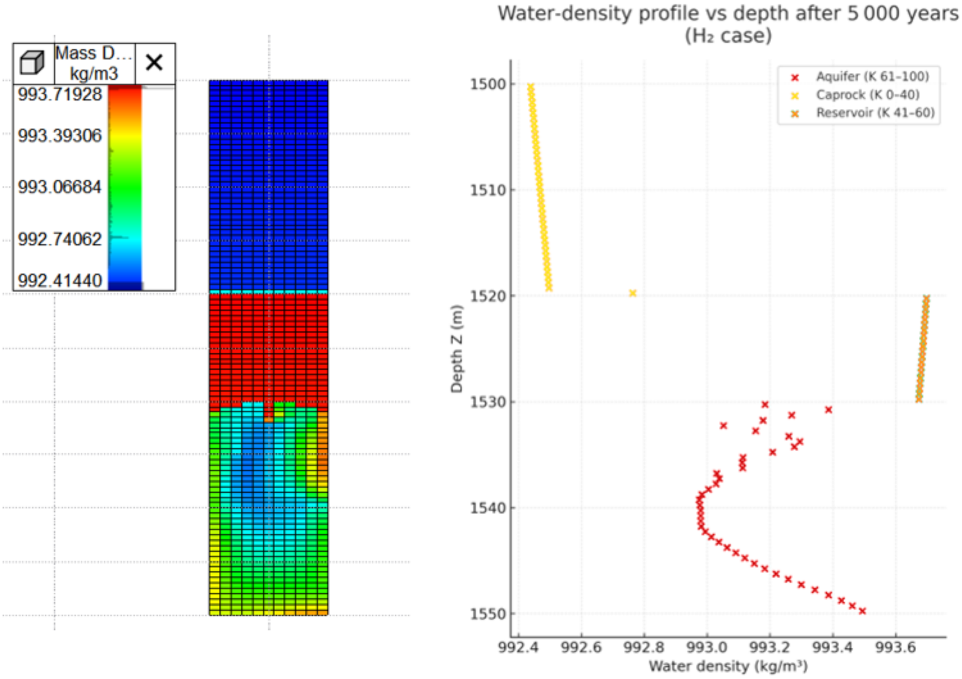

Figure 3-14: Water mass density profile after 5000 years (by filtering i=j=6).

60–65 mol % of the free gas perched at the structural crest is still made up of H_2 gas but drops abruptly to background in the cap-rock and aquifer (Figure 3-15).

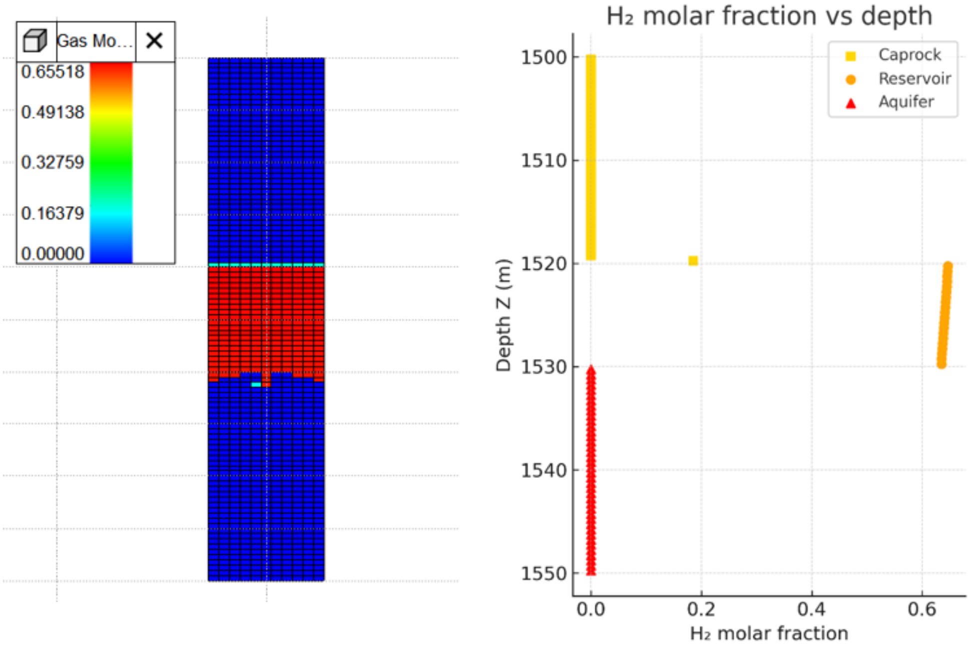

Figure 3-15: H_2 molar fraction distribution after 5000 years (by filtering i=j=6).

The cumulative mass of injected H_2 is 1550.79 kg. So, 55.46 kg of H_2 diffused outside the reservoir: most of it diffused in the aquifer (approx. 99.95%) (Figure 3-17) and a very negligible quantity diffused into the caprock (approx. 0.05%) (Figure 3-16). Furthermore, H_2 has migrated about 0.5 m into the seal (1st layer of the caprock). The Table 3-2 below compares both cases A1 and A2.

Table 3-2 : Mass balance and seal penetration for cases A1 and A2.

Case (fine grid)	Injected mass (kg)	Dissolved in aquifer (kg)	Dissolved in cap-rock (kg)	Seal penetration depth
CO_2 – A1	94324	21700	84.99	3 m (6-th layer)
H_2 – A2	1550.8	55.43	0.033	0.5 m (1-st layer)

Only 3.6 % of the injected H_2 has dissolved, compared with 23 % of the CO_2.

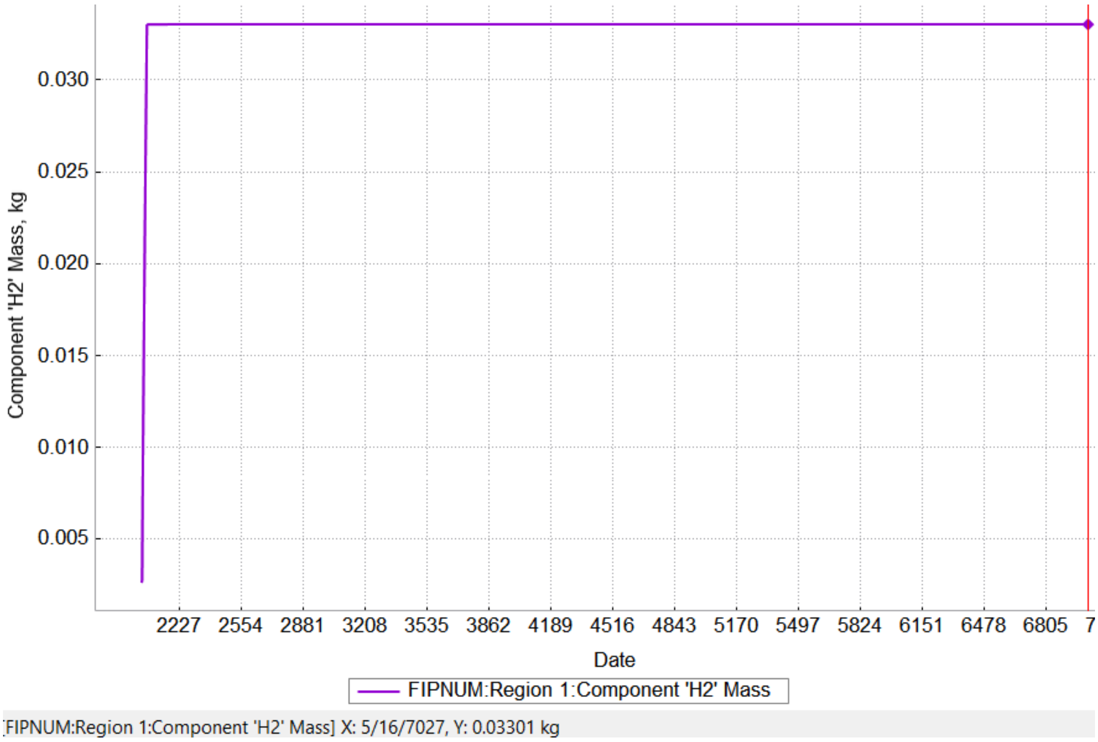

[FIPNUM:Region 1:Component 'H2' Mass] X: 5/16/7027, Y: 0.03301 kg

Figure 3-16: Mass of diffused H_2 in the caprock after 5000 years of observation.

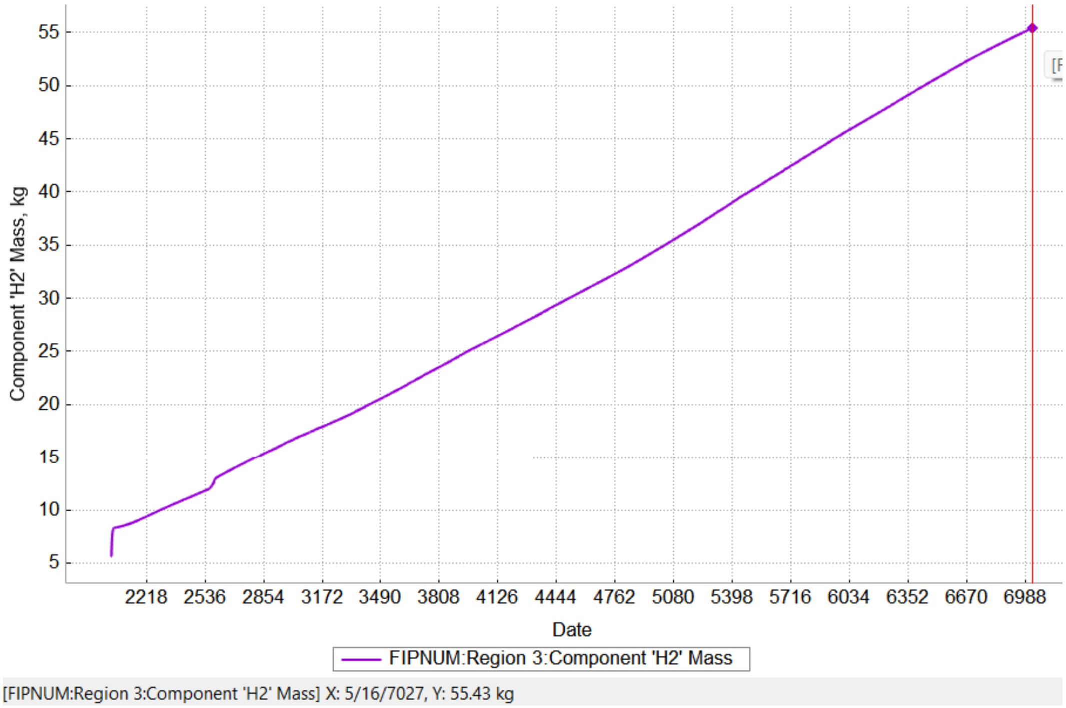

[FIPNUM:Region 3:Component 'H2' Mass] X: 5/16/7027, Y: 55.43 kg

Figure 3-17: Mass of diffused H_2 in the aquifer after 5000 years of observation.

3.2 Coarse-grid results

Case B1

The coarse model predicts a markedly simpler plume than the 1 × 1 m fine grid. Five millennia after shut-in the reservoir pressure is close to 146 bar, while the overlying cap-rock steps up to ≈ 191 bar (Figure 3-18); the aquifer has relaxed to

~147 bar. CO_2 dissolution, however, is strongly grid-sensitive: only 5640 kg has entered the aqueous phase, 98% of which resides in the aquifer (Figure 3-24) and 2% (Figure 3-23) in the first six caprock layers (Figure 3-22). That total is roughly ¼ of the CO_2 captured by the fine model, confirming that coarse cells (11 m × 11 m) under-represent the brine-gas dissolution phenomenon.

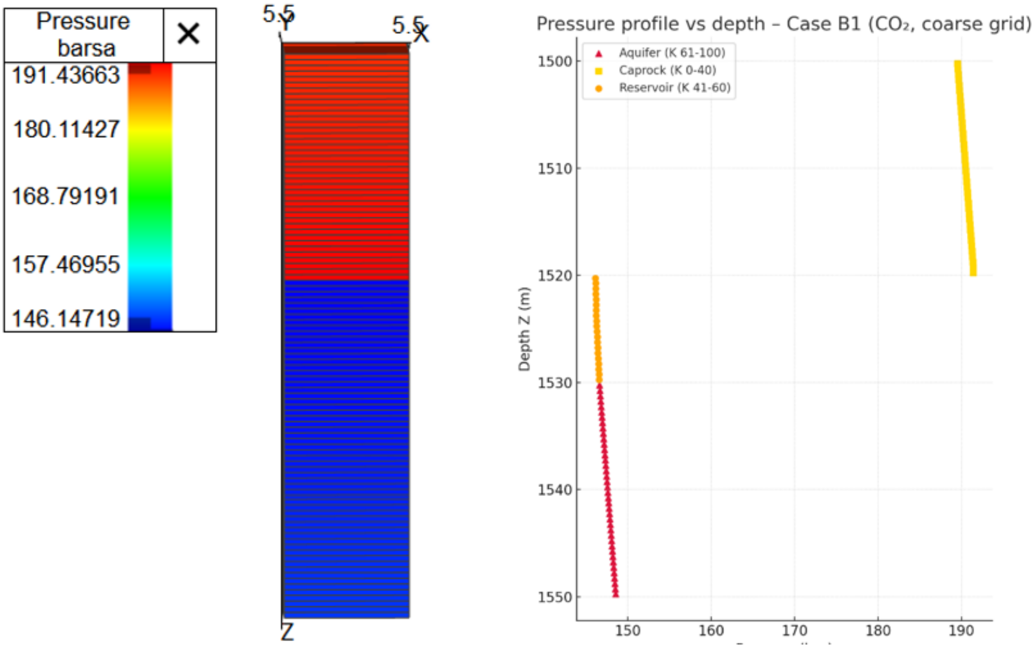

Figure 3-18: Pressure profile after 5000 years of observation.

The model still predicts a high-concentration border layer (≈ 2.3 $Sm^3\ m^{-3}$) in the cap-rock and a peak of ≈ 27 $Sm^3\ m^{-3}$ in the upper aquifer despite this underestimation (Figure 3-19). The dissolved gas equates to ~3 m vertical penetration, which is the same physical depth attained in the fine grid (Figure 3-22). The areal footprint varies because in the coarse mesh, the entire volume is contained in each 11 × 11 m cell. As a result, the dissolved mass is averaged over a considerably larger pore volume. In comparison to Case A1, the coarse model results in a flatter CH_4 counter-dissolution profile (Figure 3-20).

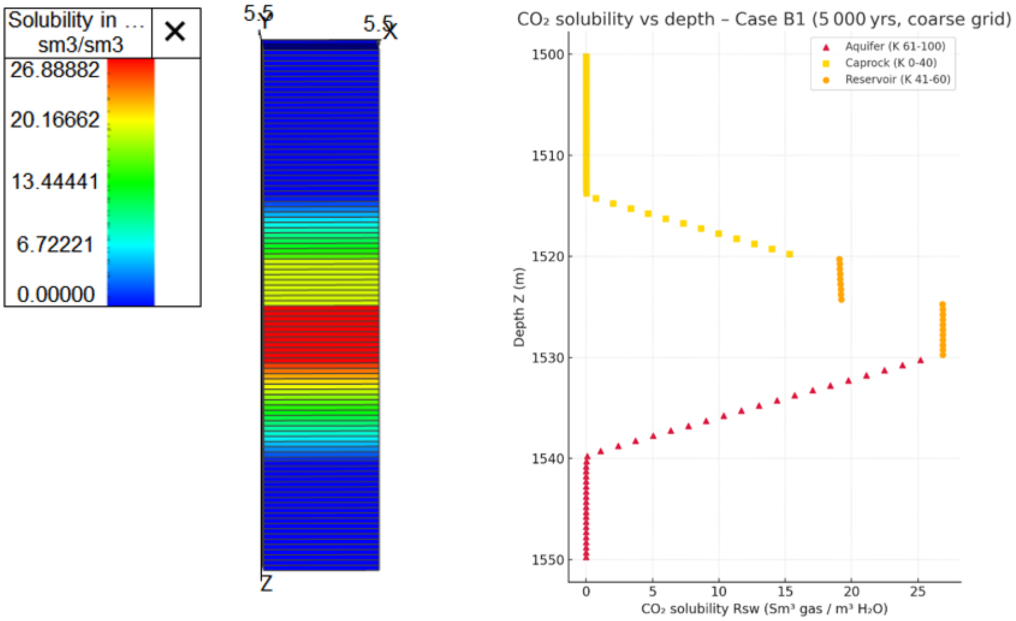

Figure 3-19: CO_2 solubility in water after 5000 years of observation.

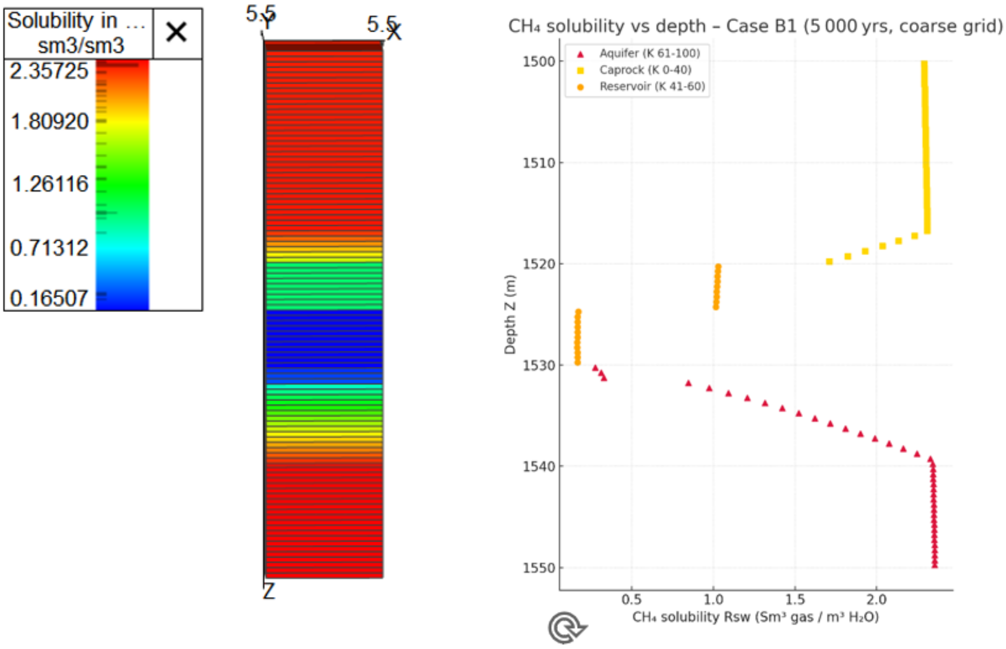

Figure 3-20: CH_4 solubility in water after 5000 years of observation.

The water-density profile (Figure 3-21) reinforces the dissolution process. Starting from an initial window of ≈ 992.3–992.6 kg m^{-3}, the caprock remains in its original range (≈ 992.3–992.6 kg m^{-3}), which is expected because only about 110 kg of CO_2 has entered that interval. Inside the storage interval the density steps up to 1000-1005 kg m^{-3}, mirroring the 27 Sm^3 m^{-3} peak in dissolved CO_2; below the plume tail the aquifer density gradually declines toward 992 kg m^{-3}. The absolute values are lower than in the fine-grid run, because the coarse cells dilute the dissolved gas over a 11 × 11 m pore volume. The correspondence confirms that the coarse mesh under-predicts the total dissolved mass.

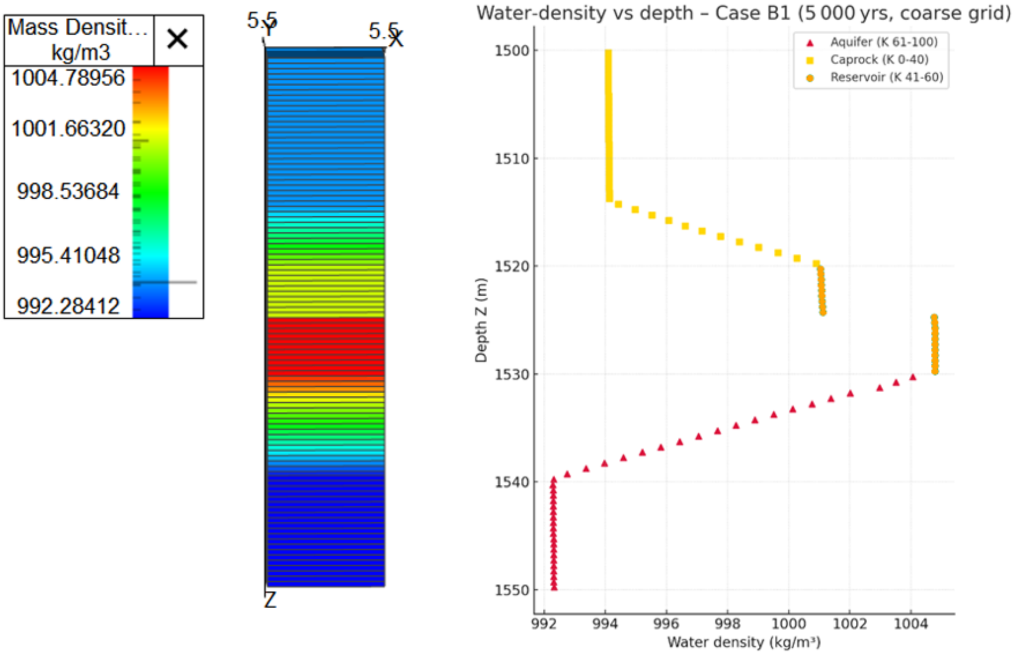

Figure 3-21: Water mass density profile after 5000 years.

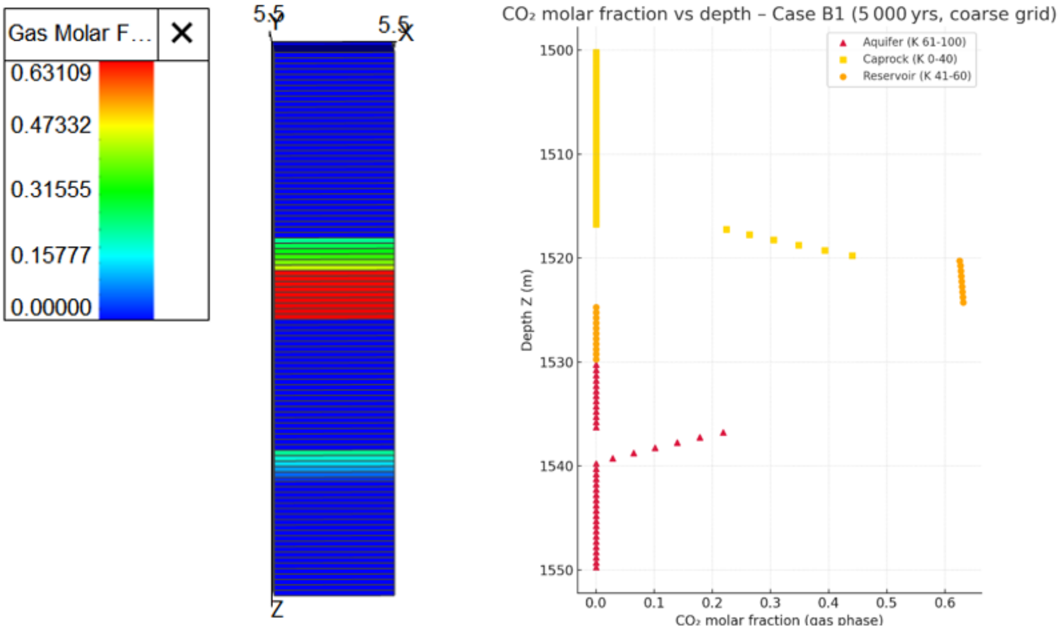

Figure 3-22: CO_2 molar fraction distribution after 5000 years.

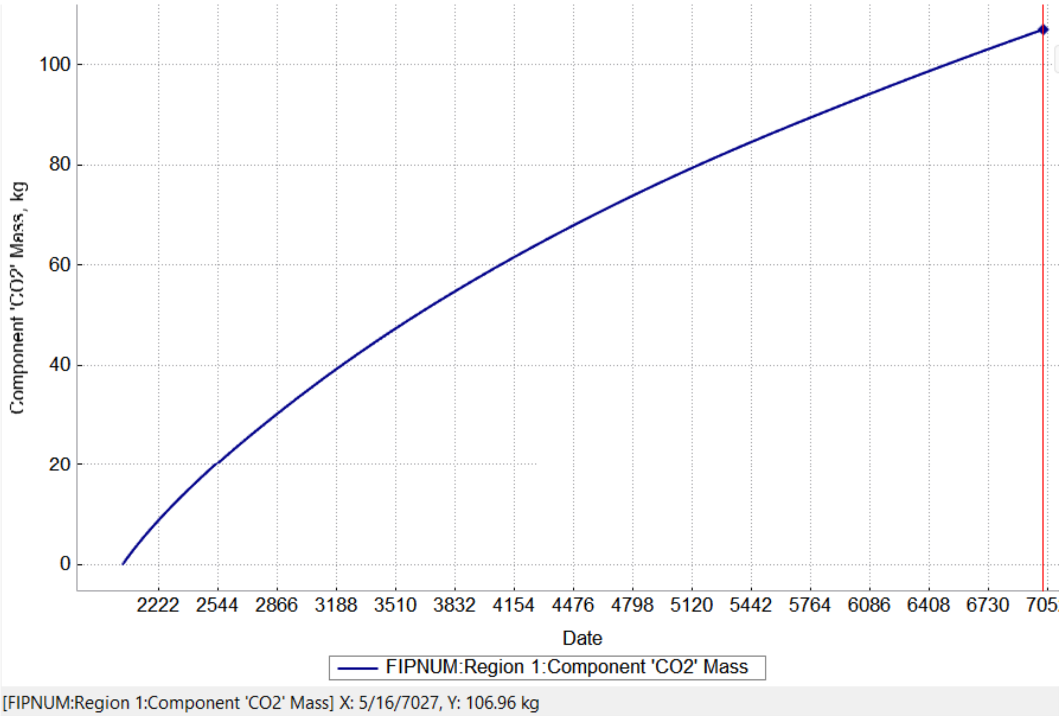

Figure 3-23: Mass of diffused CO_2 in the caprock after 5000 years of observation.

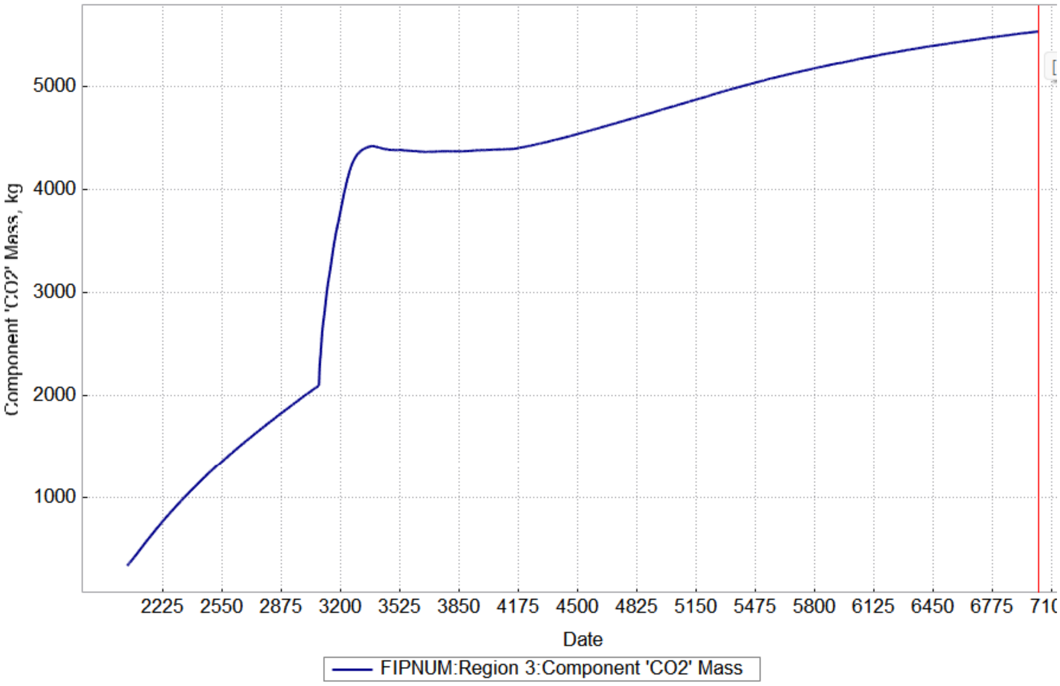

Figure 3-24: Mass of diffused CO_2 in the aquifer after 5000 years of observation.

Case B2

By the 5,000-year point, the pressure field has not significantly changed in the coarse-grid B2 scenario compared to case A2. As seen in Figure 3-25, the caprock still has a slight elastic over-pressure of about 150-152 bar that decays within the first thirty overlaying cells, while the H_2 storage interval five millennia of observation only exhibits a slight over-pressure (~152.2 bar). The underlying aquifer has somewhat softened to about 154 bar. In contrast to the 40 bar contrast observed in the same CO_2 experiment, the aquifer beneath the reservoir nearly exactly reflects the reservoir pressure.

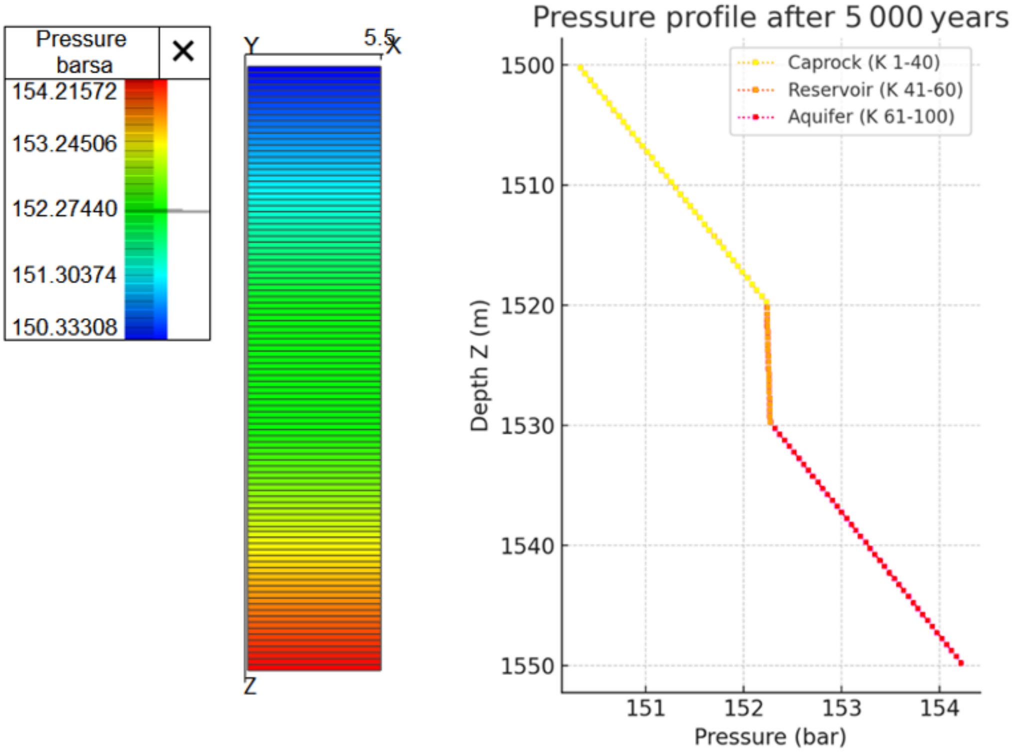

Figure 3-25: Pressure profile after 5000 years of observation.

Dissolution follows the opposite pattern to that seen in the fine-grid run. In case B2 the reservoir itself hosts the maximum dissolved H_2, reaching about 1.9 Sm^3 m^{-3} between K-layers 41 and 61 (uppermost layer of the aquifer) (Figure 3-26). Concentrations drop off sharply both upward and downward: within the first few caprock cells the value is already below 0.5 Sm^3 m^{-3}, while in the underlying aquifer the profile falls essentially to zero. This inversion relative to case A2, which showed its solubility peak in the aquifer, highlights how the coarse horizontal discretization limits the contact area for downward diffusion and instead traps most of the dissolved gas in the injection interval itself.

Figure 3-27 shows that CH_4 is most soluble outside the reservoir, with values of roughly 2.31-2.35 Sm^3 m^{-3} both in the lower caprock and in the top of the underlying aquifer, matching the colorbar maximum of 2.36 Sm^3 m^{-3}. Inside the reservoir interval, however, the solubility curve collapses to about 0.9-0.95 Sm^3 m^{-3}. This depression coincides with the zone that now hosts the highest dissolved-H_2 concentration, confirming an almost one-to-one trade-off: as hydrogen replaces methane in solution, the local CH_4 solubility falls, while the surrounding formations continue to hold close to their pre-injection equilibrium with CH_4-rich gas.

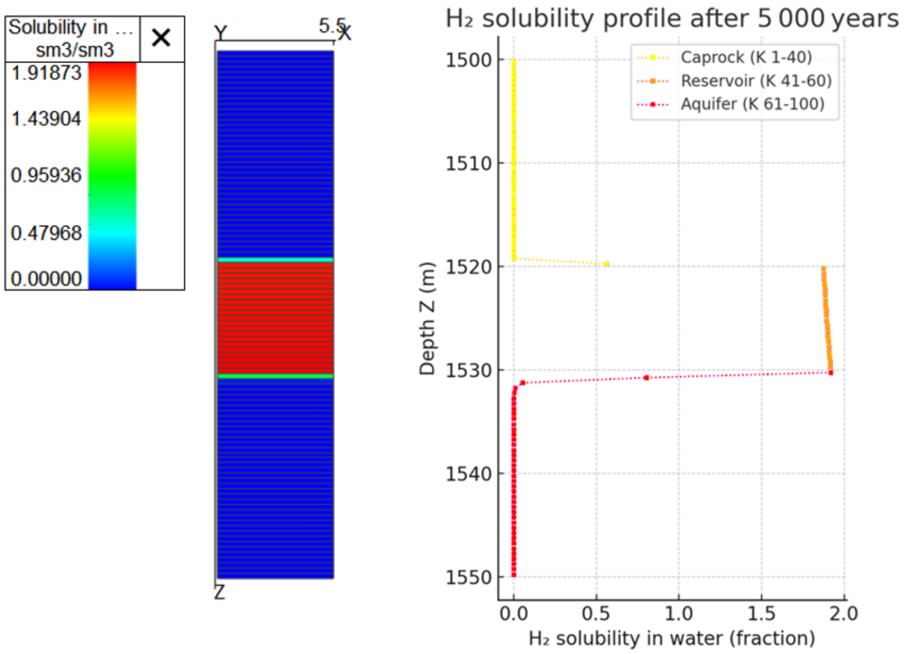

Figure 3-26: H_2 solubility in water after 5000 years of observation.

The brine-density profile varies very little because there is very little dissolved gas. The underlying aquifer and caprock both plot about 992.5 kg m⁻³, whereas the reservoir brine is the heaviest, clustering around 993.7 kg m⁻³, which is virtually their original value, as seen Figure 3-28. The increase is much too tiny to cause any noticeable convective mixing. Therefore, the highest mass density is in the reservoir due to the highest H_2 solubility in water.

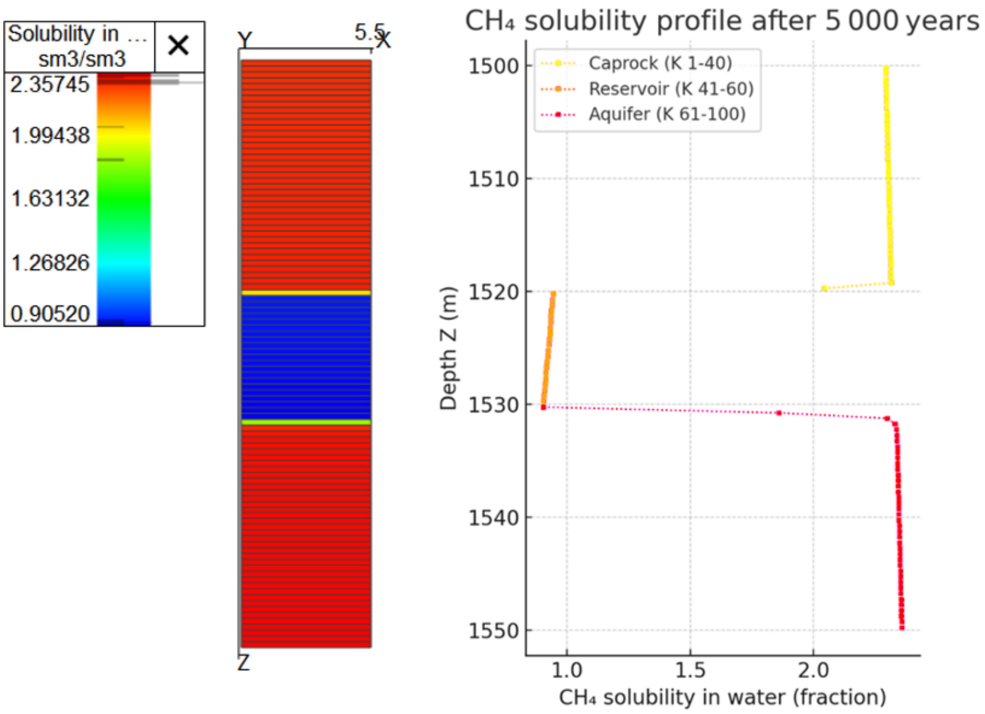

Figure 3-27: CH_4 solubility in water after 5000 years of observation.

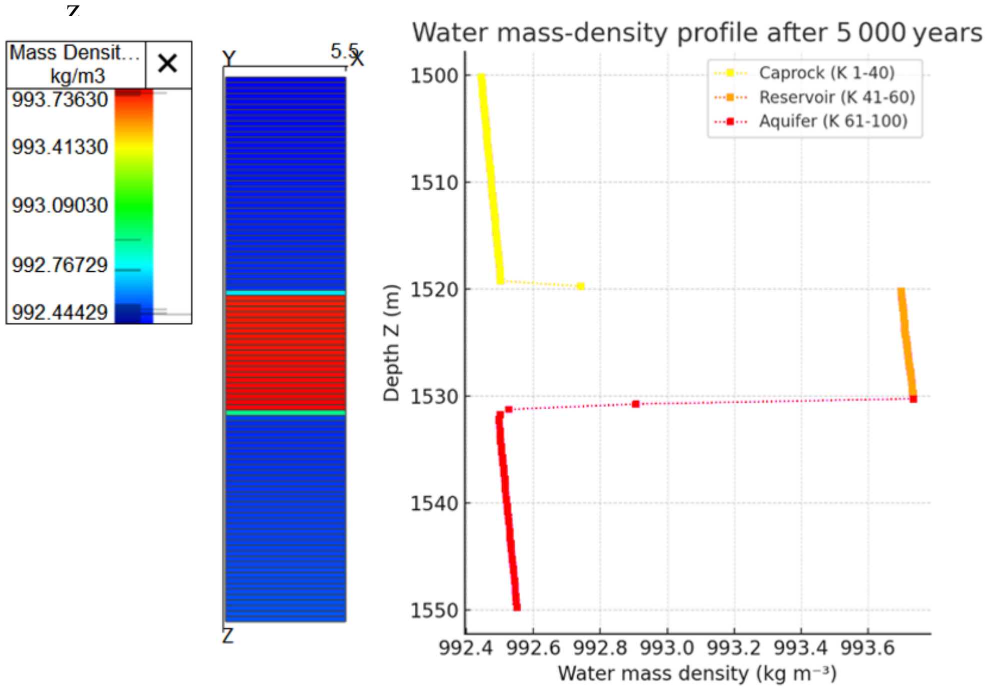

Figure 3-28: Water mass density profile after 5000 years.

Hydrogen continues to dominate the gas-phase composition in the free plume. In the reservoir, Figure 3-29 shows molar fractions of about 65-66% H_2, which drastically decrease with depth and reveal no mobile hydrogen in the caprock at all. Thus, the only upward transfer mechanism has been diffusion. This image is supported by mass-balance calculations, which show that only 8.657 kg of the 1533.12 kg injected have reached the aquifer water (Figure 3-31) and a negligible 0.031 kg (Figure 3-30) have diffused into the caprock, for a total loss of only 0.57% of the inventory. Despite the coarser discretization, vertical migration into the seal is restricted to the first half-meter of shale, which is the same penetration length as the fine-grid H_2 instance.

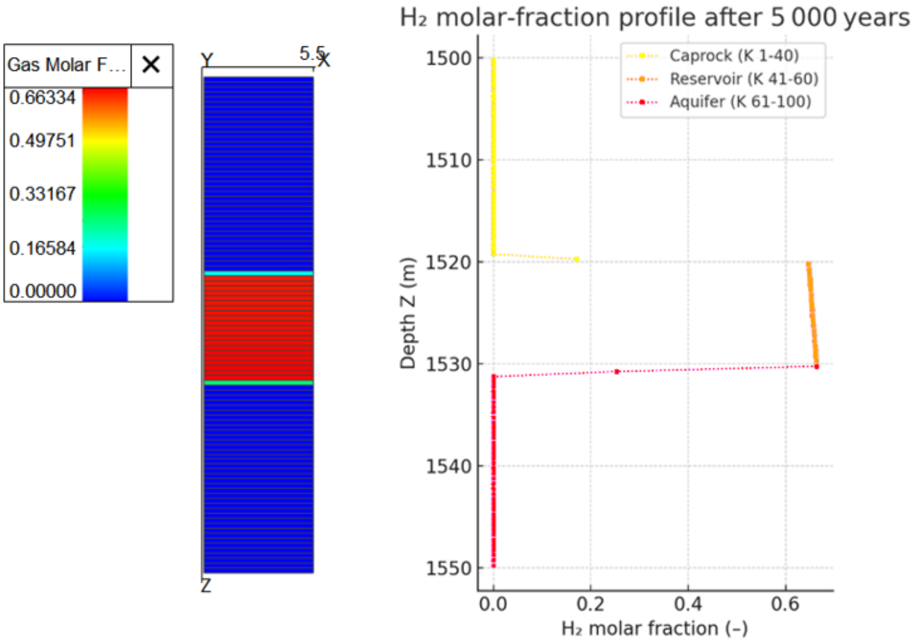

Figure 3-29: H_2 molar fraction distribution after 5000 years.

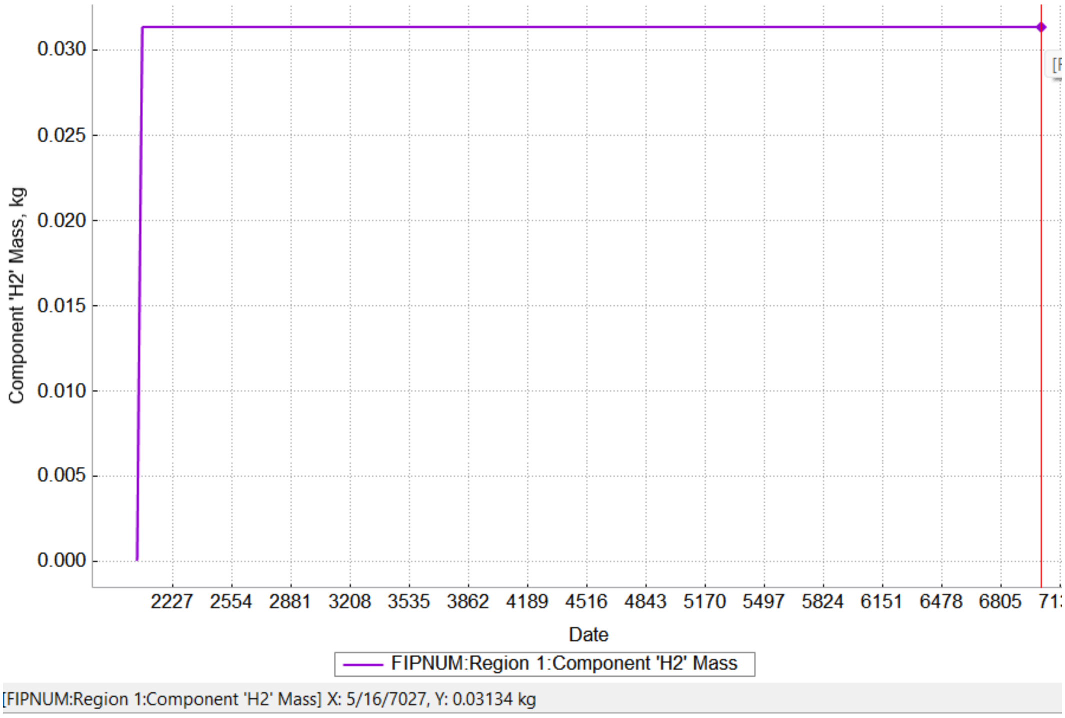

[FIPNUM:Region 1:Component 'H2' Mass] X: 5/16/7027, Y: 0.03134 kg

Figure 3-30: Mass of diffused H2 in the caprock after 5000 years of observation.

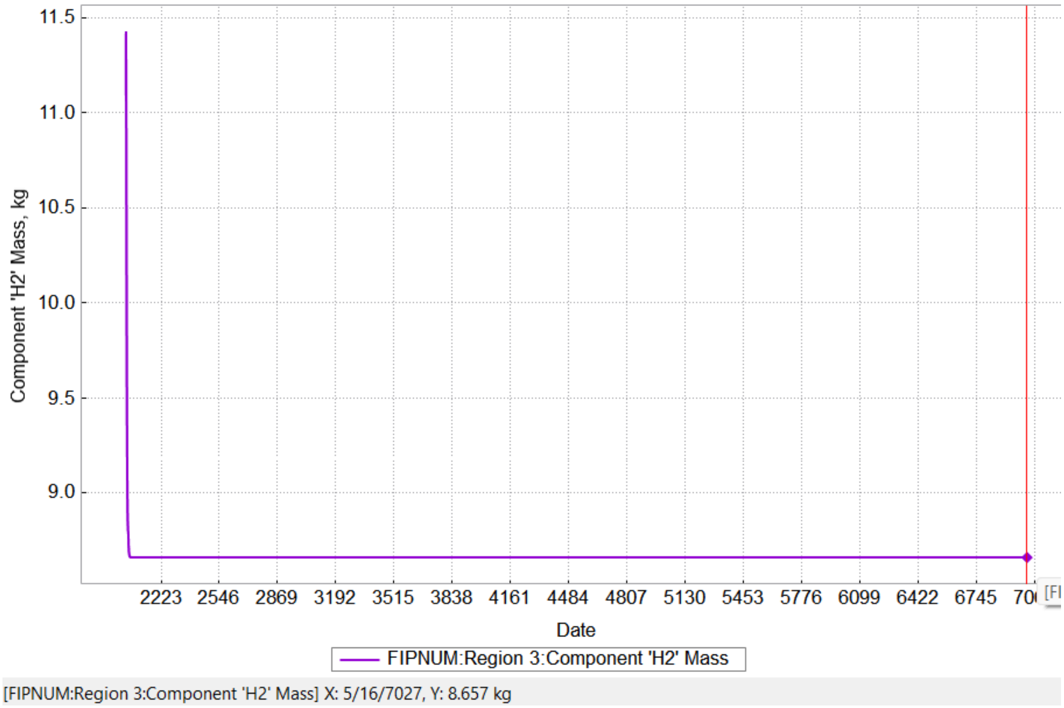

[FIPNUM:Region 3:Component 'H2' Mass] X: 5/16/7027, Y: 8.657 kg

Figure 3-31: Mass of diffused H_2 in the aquifer after 5000 years of observation.

3.3 Cross-case comparison and implications

A comparison of the four simulations shows how grid resolution and molecule type affect long-term predictions (Table 3-3). The most detailed image is always provided by the fine 1 m model (cases A1 and A2, forecasts stronger dissolution, and, for CO_2, depicts the beginning of convection in the deep aquifer. Even while penetration lengths (about 3 m for CO_2 and 0.5 m for H_2) stay the same, cumulative dissolved mass decreases by about a factor of four for CO_2 and a factor of six for H_2 when the mesh is coarsened to 11 m (cases B1 and B2).

The result is obvious: because each cell has considerably higher volume cannot resolve adequately the dissolution and, consequently, coarse grids significantly underestimate diffusive flux while preserving diffusive length-scale. Local refining around the reservoir/caprock interface is therefore crucial. The control of gas identity is similarly powerful. Because of its much larger Henry-law constant and the persistent over-pressure provided by the dense CO_2 phase, which promotes molecular diffusion, CO_2 dissolves an order of magnitude more easily than H_2 in both meshes. In other words, CO_2 provides the advantage of density-driven self-sealing in the aquifer but at the cost of greater aqueous uptake, whereas H_2 exhibits two simultaneous benefits for underground storage: restricted dissolving losses and nearly minimal upward migration beyond the first half-meter of shale.

These concepts are reinforced by pressure behavior. The necessity of active pressure management at saline-aquifer CCS sites is shown by the persistent 40 bar step that CO_2 injection leaves across the seal in both A1 and B1.

Additionally, model-input priorities are flagged by the cross-case exercise. Since diffusion completely regulates the minute mass loss into the seal, variability in effective diffusivity is more important for H_2 than uncertainty in solubility or density. The hierarchy is reversed for CO_2: laboratory-derived ρ(P,T,C) correlations and brine-salinity data become the high-value inputs because dissolved density contrast dominates aquifer convection. The 0.5-3 m diffusive fronts observed here require a vertical resolution of $\leq$ 0.5 m. The results support various confinement tactics from an operational perspective. Thick, impermeable seals and pressure management help to reduce cap-rock stress and delay density-driven fingering in CO_2 storage. Contrarily, H_2 storage depends on preserving gas purity and reducing microbiological or geochemical sinks; diffusion-mediated losses of less than 1% over five millennia indicate that multi-cycle storage should be possible even in reservoirs without convective trapping mechanisms if a competent seal is in place. For initial H_2 screening, regulators can therefore accept coarser static models; however, in order to prevent systematic under-prediction of dissolved mass and brine-density implications, CO_2 projects should use fine grids.

In summary, gas type determines how quickly, seal quality determines how far, and grid resolution determines how much gas dissolves. H_2 projects can concentrate computational efforts on well integrity and cyclic deliverability, confident that diffusion through an intact shale seal will remain a second-order concern even on millennial horizons, while CO_2 store designers must precisely resolve dissolution physics to quantify long-term brine alteration.

Table 3-3: Key outcomes after 5000 years.

Case	Grid Δx, Δy m	Injected gas	Free-phase remaining	Dissolved in aquifer	Dissolved in cap-rock	Seal penetration
A1	1 × 1	CO_2	75.9 %	23.0 % (21.7 10^3 kg)	0.09 % (85 kg)	3 m
A2	1 × 1	H_2	96.4 %	3.57 % (55 kg)	0.002 % (0.03 kg)	0.5 m
B1	11 × 11	CO_2	94.4 %	5.53 % (5.5 10^3 kg)	0.11 % (11 10^3 kg)	3 m
B2	11 × 11	H_2	99.4 %	0.565 % (8.66 kg)	0.002 % (0.03 kg)	0.5 m

Conclusion

This work compared four high-resolution ($\Delta z = 0.5$ m) simulations to clarify how molecule type and mesh size affect the long-term distribution of injected gases in a depleted reservoir. In the fine 1 m grid, ~23 % of CO_2 dissolved into brine but only ~3.6 % of H_2 did so; yet both gases diffused only a few meters into surrounding formations (≈3 m for CO_2, 0.5 m for H_2). Coarsening the horizontal mesh to 11 m cut dissolved mass by a factor of four to six while leaving penetration depths unchanged. Because the vertical discretization is unchanged, this shows that depth of diffusion is governed by rock-fluid properties, while the total dissolved mass is sensitive to grid volume resolution (larger cell underestimate dissolution phenomenon). Across every case the caprock limited losses to <1 % of inventory after 5 000 years, indicating that an intact seal remains an effective barrier on geologic time-scales.

Behavior diverged sharply between gases. CO_2 maintained a 40 bar over-pressure step and generated a dense-brine lens, so its storage security hinges on pressure management and accurate density modelling. H_2 re-equilibrated to within 2–3 bar of hydrostatic conditions, showed virtually no density contrast, and retained > 99 % of the injected mass as free gas, advantages that favor multi-cycle energy storage but place the burden on ensuring gas purity and limiting microbial or geochemical sinks. Consequently, CO_2 projects require fine local grids to capture dissolution-driven convection and to satisfy regulatory mass-balance accounting, whereas preliminary H_2 assessments can accept coarser meshes provided laboratory diffusivity data are reliable.

The study omits reactive geochemistry and large-scale structural heterogeneity; future work should couple diffusion to reactions and geomechanics in field-scale, multi-well settings. Even so, the results show that grid coarsening mainly under-predicts how much gas dissolves, not how far it travels: CO_2 trades mass for self-sealing density gradients, while H_2 remains nearly intact and diffusion-limited. With appropriate design focus, pressure control for CO_2, purity maintenance for H_2, both gases can be stored securely in depleted reservoirs over millennial horizons.

References

Amid, A., Mignard, D., & Wilkinson, M. (2016). Seasonal storage of hydrogen in a depleted natural gas reservoir. *International Journal of Hydrogen Energy, 41*(12), 5549–5558. https://doi.org/10.1016/j.ijhydene.2016.02.036.

Basniev, K. S., Omelchenko, R. J., & Adzynova, F. A. (2010). Underground hydrogen storage problems in Russia. In D. Stolten & T. Grube (Eds.), *Proceedings of the 18th World Hydrogen Energy Conference (WHEC 2010), Parallel Sessions Book 4: Storage Systems / Policy Perspectives, Initiatives and Co-operations* (pp. 47–53). Forschungszentrum Jülich GmbH, Zentralbibliothek, Verlag.

Benetatos, C.; Bocchini, S.; Carpignano, A.; Chiodoni, A.; Cocuzza, M.; Deangeli, C.; Eid, C.; Ferrero, D.; Gerboni, R.; Giglio, G.; et al. How underground systems can contribute to meet the challenges of energy transition. GEAM Geoing. Ambient. Mineraria 2021, 58, 65–80. https://doi.org/10.19199/2021.163-164.1121-9041.065.

Bird, R. B., W. E. Stewart, and E. N. Lightfoot: Transport Phenomena, Wiley, New York, 1960, chap. 16.

Bentham, M., & Kirby, G. A. (2005). CO_2 storage in saline aquifers. *Oil & Gas Science and Technology – Revue de l'IFP, 60*(3), 559–567. https://doi.org/10.2516/ogst:2005038.

Bickle, M., Chadwick, A., Huppert, H., Hallworth, M. & Lyle, S. "Modelling Carbon Dioxide Accumulation at Sleipner: Implications for Underground Carbon Storage." *Earth and Planetary Science Letters* 255 (2007): 164-176.

Bihua, X., Bin, Y., Yongqing, W. Anti-corrosion cement for sour gas (H_2S-CO_2) storage and production of HTHP deep wells. Applied Geochemistry, 2018, 96(1): 155-163. BloombergNEF. The Hydrogen Economy Outlook. March 2020.

Boving, T.B.; Grathwohl, P. Tracer diffusion coefficients in sedimentary rocks: Correlation to porosity and hydraulic conductivity. J. Contam. Hydrol. 2001, 53, 85–100. https://doi.org/10.1016/S0169-7722(01)00138-3.

Budisa, N., & Schulze-Makuch, D. (2014). Supercritical carbon dioxide and its potential as a life-sustaining solvent in a planetary environment. *Life, 4*(4), 331–340. https://doi.org/10.3390/life4030331.

Buttler, A. & Spliethoff, H., "Current Status of Water Electrolysis for Energy Storage, Grid Balancing and Sector Coupling via Power-to-Gas and Power-to-Liquids: A Review," *Renewable & Sustainable Energy Reviews*, 82, pp. 2440-2454, 2018 — Introduction, p. 2440-2442.

Cadogan, S.P., G.C. Maitland, and J.M. Trusler, Diffusion coefficients of CO_2 and N_2 in water at temperatures between 298.15 K and 423.15 K at pressures up to 45 MPa. Journal of Chemical & Engineering Data, 2014. 59(2): p. 519-525.

Carneiro, J. F., Matos, C. R., & van Gessel, S. (2019). Opportunities for large-scale energy storage in geological formations in mainland Portugal. *Renewable and Sustainable Energy Reviews, 99*, 201–211. https://doi.org/10.1016/j.rser.2018.09.036.

Chadwick, A., Arts, R., Eiken, O., Williamson, P., Williams, G. (2006). GEOPHYSICAL MONITORING OF THE CO_2 PLUME AT SLEIPNER, NORTH SEA. In: Lombardi, S., Altunina, L., Beaubien, S. (eds) Advances in the Geological Storage of Carbon Dioxide. Nato Science Series: IV: Earth and Environmental Sciences, vol 65. Springer, Dordrecht. https://doi.org/10.1007/1-4020-4471-2_25.

Cornot-Gandolphe, S. (2019). *Underground gas storage in the world—2019 status* (Cedigaz Insights No. 35). Cedigaz.

Crotogino, F., Donadei, S., Bünger, U., & Landinger, H. (2010). Large-scale hydrogen underground storage for securing future energy supplies. In D. Stolten & T. Grube (Eds.), *Proceedings of the 18th World Hydrogen Energy Conference (WHEC 2010)* (Vol. 78-4, pp. 37–45). Institute of Energy Research – Fuel Cells, Forschungszentrum Jülich.

D'Agostino, C., Mantle, M. D., Gladden, L. F., & Moggridge, G. D. (2011). Prediction of binary diffusion coefficients in non-ideal mixtures from NMR data: Hexane–nitrobenzene near its consolute point. *Chemical Engineering Science, 66*(17), 3898–3906. https://doi.org/10.1016/j.ces.2011.05.014.

D'Agostino, C., Mantle, M. D., Gladden, L. F., & Moggridge, G. D. (2012). Prediction of mutual diffusion coefficients in non-ideal mixtures from pulsed field gradient NMR data: Triethylamine–water near its consolute point. *Chemical Engineering Science, 74*, 105–113. https://doi.org/10.1016/j.ces.2012.02.025.

Dworak, K., Boukadi, F. (2024). Impact Analysis of Simulation Parameters on Supercritical Carbon Dioxide Storage Modeling in Aquifers. Petro Chem Indus Intern, 7(2), 01-14.

Equinor. (2019, 12 June). *Sleipner partnership releases CO_2 storage data*. Available at: https://www.equinor.com/news/archive/2019-06-12-sleipner-co2-storage-data.

Equinor ASA. (n.d.). *Sleipner area*. Retrieved May 21, 2025, from https://www.equinor.com/energy/sleipner.

European Commission. (2009). *Directive 2009/31/EC on the Geological Storage of Carbon Dioxide*. Official Journal of the European Union.

Feldmann, F., Hagemann, B., Ganzer, L. and Panfilov, M. 2016. Numerical simulation of hydrodynamic and gas mixing processes in underground hydrogen storages. Environmental Earth Sciences, 75, 1165. 10.1007/s12665-016-5948-z.

Fick, A. (1855). Ueber Diffusion. *Annalen der Physik und Chemie*, *170*(1), 59–86. https://doi.org/10.1002/andp.18551700105.

FRICK, U. (1993): An Evaluation of Diffusion in the Groundwater of Crystalline Rocks. Nagra unpublished Internal Report, Nagra, Wettingen, Switzerland.

Furre, A-K. & Eiken, O. "An Inverse Method for Estimating Thickness and Volume with Time of a Thin CO_2 Layer at the Sleipner Field." *Journal of Geophysical Research: Solid Earth* 122 (2017): 3382-3400.

Furre, A-K., Hansen, H., et al. "20 Years of Monitoring CO_2 Injection at Sleipner." *Energy Procedia* 114 (2017): 3916-3926.

Gainer, J. L., and A. B. Metzner: AIChE-Chem E Symp. Ser., no. 6, 1965, p. 74

Gas Infrastructure Europe. (2022, May). *Underground hydrogen storage projects* [Map]. Retrieved January 17, 2025, from https://www.h2inframap.eu/.

Gąska, K. J. (2012). *Monograph of underground gas storage in Poland* (1st ed.) [in Polish]. Oficyna Wydawnicza ASPRA-JR.

Gaus, I., Azaroual, M. & Czernichowski-Lauriol, I. Reactive transport modelling of the impact of CO2 injection on the clayey cap rock at Sleipner (North Sea). *Chem. Geol.* 217, 319–337 (2005).

Gilfillan, S., Sherk, G., Poreda, R. & Haszeldine, R. "Using Noble-Gas Fingerprints at the Kerr Farm to Assess CO_2 Leakage Allegations Linked to the Weyburn-Midale Storage Project." *International Journal of Greenhouse Gas Control* 63 (2017): 215-225.

Gomez Mendez, I.; El-Sayed, W. M. M.; Menefee, A. H.; & Karpyn, Z. T. (2024). *Insights into Underground Hydrogen Storage Challenges: A Review on Hydrodynamic and Biogeochemical Experiments in Porous Media.* Energy & Fuels. Advance online publication. https://doi.org/10.1021/acs.energyfuels.4c03142.

Government of Western Australia, Department of Energy, Mines, Industry Regulation and Safety. (2025, March 25). *Gorgon carbon dioxide injection project*. https://www.wa.gov.au/organisation/resource-and-environmental-regulation/gorgon-carbon-dioxide-injection-project.

Global CCS Institute. (2022). *Global Status of CCS 2022: Ambition to Action.* Melbourne: Global CCS Institute. Available at: https://status22.globalccsinstitute.com/.

Global CCS Institute, *Global Status of CCS 2024: Collaborating for a Net-Zero Future*. Accessed: Apr. 15, 2025. [Online]. Available: https://www.globalccsinstitute.com/resources/global-status-report/.

Goulart, M. B. R., Costa, P. V. M. da, Costa, A. M. da, Miranda, A. C. O., Mendes, A. B., Ebecken, N. F. F., Meneghini, J. R., Nishimoto, K., & Assi, G. R. S. (2020). Technology readiness assessment of ultra-deep salt caverns for carbon capture and storage in Brazil. *International Journal of Greenhouse Gas Control, 99*, Article 103083. https://doi.org/10.1016/j.ijggc.2020.103083.

Grathwohl, P.: Diffusion in natural porous media: contaminant transport, sorption/desorption and dissolution kinetics, 1st edn. Springer, New York (1998). https://doi.org/10.1007/978-1-4615-5683-1.

Ground Water Protection Council, & Interstate Oil and Gas Compact Commission. (2017). *Underground gas storage regulatory considerations: A guide* *for state and federal regulatory agencies*. GWPC & IOGCC. https://gwpc.org/wp-content/uploads/2022/12/2017_GasStorageRegulatoryConsiderations_reduce.pdf.

Guevara-Carrion, G., Ancherbak, S., Mialdun, A., Vrabec, J., & Shevtsova, V. (2019). *Diffusion of methane in supercritical carbon dioxide across the Widom line*. Scientific Reports, 9, 8466. https://doi.org/10.1038/s41598-019-44687-1.

Hagemann, B., Rasoulzadeh, M., Panfilov, M., Ganzer, L., & Reitenbach, V. (2016). Hydrogenization of underground storage of natural gas: Impact of hydrogen on the hydrodynamic and bio-chemical behavior. *Computational Geosciences, 20,* 595–606. https://doi.org/10.1007/s10596-015-9515-6.

Heinemann, N., Alcalde, J., mic, J. M., Hangx, S., Kallmeyer, J., Ostertag-Henning, C., et al. (2021). *Enabling large-scale hydrogen storage in porous media—the subsurface H_2 storage challenge*. Energy & Environmental Science, 14(2), 853-864. https://doi.org/10.1039/D0EE03536J.

Hemme, C., & Van Berk, W. (2018). Hydrogeochemical modeling to identify potential risks of underground hydrogen storage in depleted gas fields. *Applied Sciences, 8*(11), 2282. https://doi.org/10.3390/app8112282.

Holzer, L., Marmet, P., Fingerle, M., Wiegmann, A., Neumann, M., & Schmidt, V. (2023). *Tortuosity and microstructure effects in porous media: Classical theories, empirical data and modern methods* (Springer Series in Materials Science, Vol. 333). Cham, Switzerland: Springer Nature. https://doi.org/10.1007/978-3-031-30477-4.

Hoteit, H. (2013). Modeling diffusion and gas–oil mass transfer in fractured reservoirs. *Journal of Petroleum Science and Engineering, 105*, 1–17. https://doi.org/10.1016/j.petrol.2013.03.007.

Hoteit, H. & Firoozabadi, A. (2006) *Compositional modeling by the combined discontinuous Galerkin and mixed methods*. SPE Journal, 11 (1), 19–34. https://doi.org/10.2118/90276-PA.

Hulikal Chakrapani, T., Hajibeygi, H., Moultos, O. A., & Vlugt, T. J. H. (2024). *Mutual diffusivities of mixtures of carbon dioxide and hydrogen and their solubilities in brine: Insight from molecular simulations*. Industrial & Engineering

Chemistry Research, 63(23), 10456–10481. https://doi.org/10.1021/acs.iecr.4c01078.

IEAGHG, “Geological Storage of CO_2: Seal Integrity Review”, 2024-06, September 2024. https://doi.org/10.62849/2024-06.

International Energy Agency. (2019). *The future of hydrogen: Seizing today’s opportunities*. International Energy Agency. https://www.iea.org/reports/the-future-of-hydrogen.

International Energy Agency (IEA). (2020). *CCUS in clean energy transitions*. Paris: IEA. Available at: https://iea.blob.core.windows.net/assets/181b48b4-323f-454d-96fb-0bb1889d96a9/CCUS_in_clean_energy_transitions.pdf.

International Energy Agency (IEA). (2024). *Global Hydrogen Review 2024: Hydrogen demand*. Available at: https://www.iea.org/reports/global-hydrogen-review-2024/hydrogen-demand.

International Energy Agency (IEA). (2024). *Hydrogen – Low-emission fuels, Energy system*. Available at: https://www.iea.org/energy-system/low-emission-fuels/hydrogen.

International Energy Agency. (2024). *The energy sector is central to efforts to combat climate change*. Available at: https://www.iea.org/spotlights/the-energy-sector-is-central-to-efforts-to-combat-climate-change.

Ilgen, A. G., & Cygan, R. T. (2016). Mineral dissolution and precipitation during CO_2 injection at the Frio-I Brine Pilot: Geochemical modeling and uncertainty analysis. *International Journal of Greenhouse Gas Control, 44*, 166–174. https://doi.org/10.1016/j.ijggc.2015.11.022.

Ivandic, M., Juhlin, C., Lüth, S., Bergmann, P., Kashubin, A., Sopher, D., Ivanova, A., Baumann, G., & Henninges, J. (2015). Geophysical monitoring at the Ketzin pilot site for CO_2 storage: New insights into the plume evolution. *International Journal of Greenhouse Gas Control, 32,* 90–105. https://doi.org/10.1016/j.ijggc.2014.10.015.

Intergovernmental Panel on Climate Change (IPCC). (2005). *IPCC Special Report on Carbon Dioxide Capture and Storage* (B. Metz, O. Davidson, H. C. de Coninck, M. Loos & L. A. Meyer, Eds.). Prepared by Working Group III of the IPCC. Cambridge, United Kingdom & New York, NY: Cambridge University Press, 442 pp. ISBN 978-0-521-86643-9. Retrieved from https://www.ipcc.ch/report/carbon-dioxide-capture-and-storage/.

Johnson, J. W., Nitao, J. J. & Morris, J. P. Reactive transport modeling of cap-rock integrity during natural and engineered CO2 storage. *Carbon Dioxide Capture for Storage in Deep Geologic Formations* 2, 787 (2004).

Kanaani, M., Sedaee, B., & Asadian-Pakfar, M. (2022). *Role of cushion gas on underground hydrogen storage in depleted oil reservoirs*. Journal of Energy Storage, 45, 103783. https://doi.org/10.1016/j.est.2021.103783.

Kampman, J. F., Evans, J. P., Maskell, A., Chapman, H. J., & Bickle, M. J. (2016). Observational evidence confirms modelling of the long-term integrity of CO_2-reservoir caprocks. *Nature Communications, 7*, 12268. https://doi.org/10.1038/ncomms12268.

Kerkache, H., Hoang, H., Nguyen, T. K. N., Geoffroy-Neveux, A., Nieto-Draghi, C., Cézac, P., Chabab, S., & Galliéro, G. (2025). Assessment of H_2 diffusivity in water and brine for underground storage: A molecular dynamics approach. *International Journal of Hydrogen Energy, 128*, 279–290. https://doi.org/10.1016/j.ijhydene.2025.04.157.

Krevor, S. C. M., Blunt, M. J., Benson, S. M., *et al.* (2015). *Capillary trapping for geologic carbon dioxide storage – from pore-scale physics to field-scale implications*. **International Journal of Greenhouse Gas Control, 40,** 221–237. https://doi.org/10.1016/j.ijggc.2015.04.006.

Krishna, R., & Wesselingh, J. A. (1997). The Maxwell–Stefan approach to mass transfer. *Chemical Engineering Science, 52*(6), 861–911. https://doi.org/10.1016/S0009-2509(96)00458-7.

Kruck, O., & Crotogino, F. (2013). *Benchmarking of selected storage options* (HyUnder Project Deliverable 3.3). HyUnder. https://hyunder.eu/wp-content/uploads/2016/01/D3.3_Benchmarking-of-selected-storage-options.pdf.

Langmi, H.W.; Engelbrecht, N.; Modisha, P.M.; Bessarabov, D. Hydrogen storage. In Electrochemical Power Sources: Fundamentals, Systems, and Applications, Elsevier: Amsterdam, The Netherlands, 2022; pp. 455–486. https://doi.org/10.1016/B978-0-12-819424-9.00006-9.

Lake, L. W., Johns, R. T., Rossen, W. R., & Pope, G. A. (2014). *Fundamentals of enhanced oil recovery*. Society of Petroleum Engineers. https://doi.org/10.2118/9781613993286.

Land CS. Calculation of imbibition relative permeability for two- and three-phase flow from rock properties. Soc Pet Eng J 1968;8:149–56. https://doi.org/10.2118/1942-PA.

Lekić, A., Jukić, L., Arnaut, M. & Macenić, M. (2019). “Simulation of CO_2 injection in a depleted gas reservoir: A case study for Upper Miocene sandstone, Northern Croatia.” *Rudarsko-geološko-naftni zbornik*, 34 (1), 139–149. https://doi.org/10.17794/rgn.2019.1.12.

Li D, Beyer C, Bauer S. A unified phase equilibrium model for hydrogen solubility and solution density. Int J Hydrogen Energy 2018;43(1):512–29.

Liu, F. et al. CO2–brine–caprock interaction: reactivity experiments on Eau Claire shale and a review of relevant literature. *Int. J. Greenhouse Gas Control* **7**, 153–167 (2012).

Lewandowska-Śmierszchalska, J., Tarkowski, R., & Uliasz-Misiak, B. (2018). Screening and ranking framework for underground hydrogen storage site selection in Poland. *International Journal of Hydrogen Energy, 43*(9), 4401–4414. https://doi.org/10.1016/j.ijhydene.2018.01.089.

Lord, A. S., Kobos, P. H., & Borns, D. J. (2014). Geologic storage of hydrogen: Scaling up to meet city transportation demands. *International Journal of Hydrogen Energy*, **39**, 15570–15582.

Majer, A., Stoneman, B., & Vikalo, V. (2018, December 6). *Weyburn Unit—Extending the horizon* [Conference presentation]. 24th Annual CO_2 & ROZ Conference, Midland, TX, United States. Retrieved May 21, 2025, from https://www.co2conference.net/wp-content/uploads/2018/12/Th8-Update-on-the-Weyburn-Project-in-Canada-Dec-6-2018.pdf.

Ma, X., Yang, G., Li, X., Yu, Y., & Dong, J. (2019). Geochemical modeling of changes in caprock permeability caused by CO_2–brine–rock interactions under the diffusion mechanism. *Oil & Gas Science and Technology – Revue d'IFP Energies nouvelles, 74*, 83. https://doi.org/10.2516/ogst/2019055.

Mao, S., Chen, B., Morales, M. M., Malki, M. L., & Mehana, M. (2024). Cushion gas effects on hydrogen storage in porous rocks: Insights from reservoir simulation and deep learning. *International Journal of Hydrogen Energy, 68*, 1033–1047. https://doi.org/10.1016/j.ijhydene.2024.04.288.

Marrero, T. R., & Mason, E. A. (1972). Gaseous diffusion coefficients. *Journal of Physical and Chemical Reference Data, 1*(1), 3–118. https://doi.org/10.1063/1.3253094.

Matos, C. R., Carneiro, J. F., & Silva, P. P**.** (2019). Overview of large-scale underground energy storage technologies for integration of renewable energies and criteria for reservoir identification. *Journal of Energy Storage, 21*, 241–258. https://doi.org/10.1016/j.est.2018.11.023.

Maxwell, J.C., 1972. On the dynamical theory of gases. Phil. Mag. 157, 49-88.

Miocic, J., Heinemann, N., Edlmann, K., Scafidi, J., Molaei, F., & Alcalde, J. (2023). Underground hydrogen storage: a review. Geological Society Special Publications, 528, 73–86. https://doi.org/10.1144/SP528-2022-88.

Morris, J. P., Hao, Y., Foxall, W., & McNab, W. (2011). In Salah CO_2 storage JIP: Hydromechanical simulations of surface uplift due to CO_2 injection at In Salah. *Energy Procedia, 4*, 3269–3275. https://doi.org/10.1016/j.egypro.2011.02.246.

Moultos, O.A., et al., Atomistic molecular dynamics simulations of CO_2 diffusivity in H_2O for a wide range of temperatures and pressures. The Journal of Physical Chemistry B, 2014. 118(20): p. 5532-5541.

Nassan, T., Alkan, H., Solbakken, J., Zamani, N., Burachok, O., & Amro, M. (2022, May 1). *A review of reservoir engineering tools and procedures to design and operate geological carbon storage sites* (ISBN 978-3-947716-41-8) [Conference paper]. DGMK/ÖGEW Frühjahrtagung 2022—Geo-Energy-Systems and Subsurface Technologies: Key Elements toward a Low-Carbon World, Celle, Germany. SSRN.

National Institute of Standards and Technology (NIST). (2025). *Thermophysical properties of fluid systems*. Retrieved May 23, 2025, from https://webbook.nist.gov/chemistry/fluid/.

Neufeld, P. D., Janzen, A. R., & Aziz, R. A. (1972). Empirical equations to calculate 16 of the transport collision integrals $\Omega^{(l,s)*}$ for the Lennard-Jones (12–6) potential. *Journal of Chemical Physics, 57*(3), 1100–1102. https://doi.org/10.1063/1.1678363.

NOAA Climate.gov (2023) *CO_2 emissions vs. atmospheric concentration, 1750-2023*. National Oceanic and Atmospheric Administration. Available at: https://www.climate.gov/media/14596.

Omrani, S., Ghasemi, M., Mahmoodpour, S., Shafiei, A., & Rostami, B. (2022). Insights from molecular dynamics on CO_2 diffusion coefficient in saline water over a wide range of temperatures, pressures, and salinity: CO_2 geological storage implications. *Journal of Molecular Liquids, 345*, Article 117868. https://doi.org/10.1016/j.molliq.2021.117868.

Pan, B., Yin, X., Ju, Y., & Iglauer, S. (2021). *Underground hydrogen storage: Influencing parameters and future outlook.* Advances in Colloid and Interface Science, 294, 102473. https://doi.org/10.1016/j.cis.2021.102473.

Panfilov M. Underground and pipeline hydrogen storage. Compend. Hydrog. Energy. 1st ed., vol. 2. Elsevier; 2016. p. 91–115. https://doi.org/10.1016/b978-1-78242-362-1.00004-3.

Paterson, L. 1983. The implications of fingering in underground hydrogen storage. International Journal of Hydrogen Energy, 8, 53–59. https://doi.org/10.1016/0360-3199(83)90035-6.

Pfeiffer, W.T. and Bauer, S. 2015. Subsurface porous media hydrogen storage – scenario development and simulation. Energy Procedia, 76, 565–572. https://doi.org/10.1016/j.egypro.2015.07.872.

Piszko, M., Schmidt, P. S., Rausch, M. H., & Fröba, A. P. (2023). "Thermal Diffusivity and Fick Diffusion Coefficient in Mixtures of Hydrogen and Methane by Dynamic Light Scattering." *International Journal of Thermophysics*, 44, 146. https://doi.org/10.1007/s10765-023-03250-x.

Polat, H. M., Coelho, F. M., Vlugt, T. J. H., Mercier Franco, L. F., Tsimpanogiannis, I. N., & Moultos, O. A. (2024). Diffusivity of CO_2 in H_2O: A review of experimental studies and molecular simulations in the bulk and in confinement. *Journal of Chemical & Engineering Data, 69*(10), 3296–3329. https://doi.org/10.1021/acs.jced.3c00778.

Poling, B. E., Prausnitz, J. M., & O'Connell, J. P. (2001). *Properties of gases and liquids* (5th ed.). McGraw-Hill.

Pottier, J. D., & Blondin, E. (1995). Mass storage of hydrogen. In Y. Yürüm (Ed.), *Hydrogen energy system: Production and utilization of hydrogen and future aspects* (pp. 167–179). Springer. https://doi.org/10.1007/978-94-011-0111-0_11.

RAG Austria AG and partners. *Underground Sun Storage – Final Public Report* (2017): Sections 4.2 & 4.7 (cap-rock integrity and gas analyses).

Raza, A., Arif, M., Glatz, G., Mahmoud, M., Al Kobaisi, M., Alafnan, S., & Iglauer, S. (2022). A holistic overview of underground hydrogen storage: Influencing factors, current understanding, and outlook. *Fuel, 330*, 125636. https://doi.org/10.1016/j.fuel.2022.125636.

Reid, R. C., Prausnitz, J. M., & Poling, B. E. (1987). *The properties of gases and liquids* (4th ed.). McGraw-Hill.

Rhodes, R. Explosive Lessons in Hydrogen Safety. Apple Knowl. Serv. ASK Mag. NASA 2011, 41, 46–50.

Riazi, M. R., and C. H. Whitson: Ind. Eng. Chem. Res., 32: 3081 (1993).

Riddiford, F., Wright, I., Bishop, C., Espie, T. & Tourqui, A. (2005). *Monitoring geological storage: The In Salah Gas CO_2 Storage Project.* In E.S. Rubin, D.W. Keith, C.F. Gilboy & T. Morris (Eds.), Greenhouse Gas Control Technologies **7** – Proceedings of the 7th International Conference on Greenhouse Gas Control Technologies (GHGT-7), Vancouver, Canada, 5–9 September 2004 (pp. 1353–1359). Oxford: Elsevier. https://doi.org/10.1016/B978-008044704-9/50149-X.

Rock Flow Dynamics. 2024. *tNavigator Simulation User Manual: Dynamic Modelling & Simulation Keywords* (Release 24.3). Rock Flow Dynamics Ltd., Moscow & Houston, 2 300 pp. Available to licensed users via the RFD Client-Portal “Resources Hub”.

Rucci, A., Vasco, D. W., & Novali, F. “Surface Deformation Induced by CO_2 Injection at In Salah: InSAR Analysis and Geomechanical Modelling.” *Geophysical Journal International* 193 (2013): 197-208.

Sachs, W. (1998). *The diffusional transport of methane in liquid water: Method and result of experimental investigation at elevated pressure. Journal of Petroleum Science and Engineering, 21*(3–4), 153–164. https://doi.org/10.1016/S0920-4105(98)00048-5.

Shi, Z., Wen, B., Hesse, M. A., Tsotsis, T. T., & Jessen, K. (2018). Measurement and modeling of CO_2 mass transfer in brine at reservoir conditions. *Advances in Water Resources, 113*, 100–111. https://doi.org/10.1016/j.advwatres.2017.11.002.

Sistan, M., Ghazanfari, M. H., & Jamshidi, S. (2019). Investigating the performance of generalized Fick and Maxwell–Stefan molecular diffusion models for simulation of oil recovery from fractured reservoirs during CO_2 and methane gas injection processes. *Petroleum Research, 29*(98-1), 16–28. https://doi.org/10.22078/pr.2018.3447.2574.

Smith, M. M., Sholokhova, Y., Hao, Y., & Carroll, S. A. (2013). *Evaporite caprock integrity: An experimental study of reactive mineralogy and pore-scale heterogeneity during brine–CO_2 exposure.* Environmental Science & Technology, 47(1), 262–268. https://doi.org/10.1021/es3012723.

Steel, L., Liu, Q., Mackay, E. J., & Maroto-Valer, M. (2016). CO_2 solubility measurements in brine under reservoir conditions: A comparison of experimental and geochemical modeling methods. *Greenhouse Gases: Science and Technology, 6*(2), Article 1590. https://doi.org/10.1002/ghg.1590.

Steefel, C. I., and K. Maher (2009), Fluid-Rock Interaction: A Reactive Transport Approach, *Rev Mineral Geochem*, *70*, 485-532.

Stefan, J., 2007. Über das Gleichgewicht und die Bewegung insbesondere die Diffusion von Gasmengen. Sitzber.akad.wiss.wien.

Takahashi, S. (1974). Preparation of a generalized chart for the diffusion coefficients of gases at high pressures. *Journal of Chemical Engineering of Japan, 7*(6), 417–420.

Tarkowski, R. (2019). Underground hydrogen storage: Characteristics and prospects. *Renewable and Sustainable Energy Reviews, 105*, 86–94. https://doi.org/10.1016/j.rser.2019.01.051.

Tawil, M.; Salina Borello, E.; Bocchini, S.; Pirri, C.F.; Verga, F.; Coti, C.; Scapolo, M.; Barbieri, D.; Viberti, D. Solubility of H2-CH4 Mixtures in Brine at Underground Hydrogen Storage Thermodynamic Conditions. *Frontiers in Energy Research* **2024**, *Volume 12-2024*, doi:10.3389/fenrg.2024.1356491.

Tsimpanogiannis, I.N., et al., Engineering Model for Predicting the Intradiffusion Coefficients of Hydrogen and Oxygen in Vapor, Liquid, and Supercritical Water based on Molecular Dynamics Simulations. Journal of Chemical & Engineering Data, 2021.

Uliasz-Misiak, B., & Chruszcz-Lipska, K. (2017). Hydrogeochemical aspects associated with the mixing of formation waters injected into the hydrocarbon reservoir. *Gospodarka Surowcami Mineralnymi – Mineral Resources Management, 33*(2), 69–80. https://doi.org/10.1515/gospo-2017-0017.

United Nations Framework Convention on Climate Change (UNFCCC). (2015). *The Paris Agreement*. Available at: https://unfccc.int/process-and-meetings/the-paris-agreement.

U.S. Environmental Protection Agency (EPA). (2010). *Federal Requirements Under the Underground Injection Control (UIC) Program for Carbon Dioxide (CO_2) Geologic Sequestration (GS) Wells; Final Rule.* Federal Register, 75(237), 77230–77303. Issued 10 December 2010 (effective 10 January 2011). Retrieved from https://www.federalregister.gov/documents/2010/12/10/2010-29954/federal-requirements-under-the-underground-injection-control-uic-program-for-carbon-dioxide-co2.

Wallace, R. L., Cai, Z., Zhang, H., Zhang, K., & Guo, C. (2021). Utility-scale subsurface hydrogen storage: UK perspectives and technology. *International Journal of Hydrogen Energy, 46*(49), 25137–25159. https://doi.org/10.1016/j.ijhydene.2021.05.034.

Wang, S., Zhou, T., Pan, Z., & Trusler, J. P. M. (2023). *Diffusion coefficients of N_2O and H_2 in water at temperatures between 298.15 and 423.15 K with pressures up to 30 MPa*. *Journal of Chemical & Engineering Data, 68*(6), 1313–1319. https://doi.org/10.1021/acs.jced.3c00085.

Warren, J. K. (2016). **Solution mining and salt cavern usage**. In *Evaporites: A geological compendium* (2nd ed., pp. 1303–1374). Springer International Publishing. https://doi.org/10.1007/978-3-319-13512-0_13.

Weber, U. W., Rinaldi, A. P., et al. "In-situ Experiment Reveals CO_2-Enriched Fluid Migration in Faulted Caprock." *Scientific Reports* 13 (2023): 17006.

White, J. A., Chiaramonte, L., et al. "Geomechanical Behavior of the Reservoir and Caprock System at the In Salah CO_2 Storage Project." *PNAS* 111 (2014): 8747-8752.

White, C. M., Smith, D. H., Jones, K. L., Goodman, A. L., Jikich, S. A., LaCount, R. B., DuBose, S. B., Ozdemir, E., Morsi, B. I., & Schroeder, K. T. (2005). *Sequestration of carbon dioxide in coal with enhanced coalbed methane recovery—A review*. **Energy & Fuels, 19**(3), 659–724.

Wilke, C. R., & Lee, C.-Y. (1955). Estimation of diffusion coefficients for gases and vapors. *Industrial & Engineering Chemistry, 47*(6), 1253–1257. https://doi.org/10.1021/ie50546a056.

Wilson, M., & Monea, M. (2004). *IEA GHG Weyburn CO_2 Monitoring & Storage Project Summary Report 2000–2004*. Petroleum Technology Research Centre.

Xie, L. H., Zhang, H., & Li, H. L. (2009). Accident analysis and risk identification of underground gas storage rebuilt upon depleted oil and gas reservoirs. *Natural Gas Industry, 29*(11), 116–119.

Yan, W., Yang, Y., & Stenby, E. H. (2024). Determination of diffusion coefficients from constant volume diffusion tests through numerical simulation. *Fluid Phase Equilibria, 576*, 113944. https://doi.org/10.1016/j.fluid.2023.113944.

Zhang, L., Allendorf, M. D., Broom, D. P., et al. (2022). "Fundamentals of hydrogen storage in nanoporous materials." *Progress in Energy,* 4, 042013. https://doi.org/10.1088/2516-1083/ac8d44.

Zhang, W., et al., The modeling and experimental studies on the diffusion coefficient of CO_2 in saline water. Journal of CO_2 Utilization, 2015. 11: p. 49-53.

Zhao, W., Jang, H. W., & Yang, D. (2023). Determination of concentration-dependent effective diffusivity of each gas component of a binary mixture in porous media saturated with heavy oil under reservoir conditions. *SPE Reservoir Evaluation & Engineering, 26*(4), 1197–1211. https://doi.org/10.2118/215832-PA.

Zivar, D.; Kumar, S.; Foroozesh, J. Underground hydrogen storage: A comprehensive review. Int. J. Hydrog. Energy 2021, 46, 23436–23462. https://doi.org/10.1016/j.ijhydene.2020.08.138.

Appendix 1

```
NOECHO

COORD
 2*-5.5  1500 2*-5.5  1550  -4.5  -5.5  1500  -4.5  -5.5  1550  -3.5  -5.5  1500
-3.5  -5.5  1550  -2.5  -5.5
  1500  -2.5  -5.5  1550  -1.5  -5.5  1500  -1.5  -5.5  1550  -0.5  -5.5  1500
-0.5  -5.5  1550   0.5  -5.5
  1500   0.5  -5.5  1550   1.5  -5.5  1500   1.5  -5.5  1550   2.5  -5.5  1500
2.5  -5.5  1550   3.5  -5.5
  1500   3.5  -5.5  1550   4.5  -5.5  1500   4.5  -5.5  1550   5.5  -5.5  1500
5.5  -5.5  1550  -5.5  -4.5
  1500  -5.5  -4.5  1550 2*-4.5  1500 2*-4.5  1550  -3.5  -4.5  1500  -3.5  -4.5
1550  -2.5  -4.5  1500  -2.5
  -4.5  1550  -1.5  -4.5  1500  -1.5  -4.5  1550  -0.5  -4.5  1500  -0.5  -4.5
1550   0.5  -4.5  1500   0.5
  -4.5  1550   1.5  -4.5  1500   1.5  -4.5  1550   2.5  -4.5  1500   2.5  -4.5
1550   3.5  -4.5  1500   3.5
  -4.5  1550   4.5  -4.5  1500   4.5  -4.5  1550   5.5  -4.5  1500   5.5  -4.5
1550  -5.5  -3.5  1500  -5.5
  -3.5  1550  -4.5  -3.5  1500  -4.5  -3.5  1550 2*-3.5  1500 2*-3.5  1550  -2.5
-3.5  1500  -2.5  -3.5  1550
  -1.5  -3.5  1500  -1.5  -3.5  1550  -0.5  -3.5  1500  -0.5  -3.5  1550   0.5  -
3.5  1500   0.5  -3.5  1550
   1.5  -3.5  1500   1.5  -3.5  1550   2.5  -3.5  1500   2.5  -3.5  1550   3.5  -
3.5  1500   3.5  -3.5  1550
   4.5  -3.5  1500   4.5  -3.5  1550   5.5  -3.5  1500   5.5  -3.5  1550  -5.5  -
2.5  1500  -5.5  -2.5  1550
  -4.5  -2.5  1500  -4.5  -2.5  1550  -3.5  -2.5  1500  -3.5  -2.5  1550 2*-2.5
1500 2*-2.5  1550  -1.5  -2.5
  1500  -1.5  -2.5  1550  -0.5  -2.5  1500  -0.5  -2.5  1550   0.5  -2.5  1500
0.5  -2.5  1550   1.5  -2.5
  1500   1.5  -2.5  1550   2.5  -2.5  1500   2.5  -2.5  1550   3.5  -2.5  1500
3.5  -2.5  1550   4.5  -2.5
  1500   4.5  -2.5  1550   5.5  -2.5  1500   5.5  -2.5  1550  -5.5  -1.5  1500  -
5.5  -1.5  1550  -4.5  -1.5
  1500  -4.5  -1.5  1550  -3.5  -1.5  1500  -3.5  -1.5  1550  -2.5  -1.5  1500
-2.5  -1.5  1550 2*-1.5  1500
 2*-1.5  1550  -0.5  -1.5  1500  -0.5  -1.5  1550   0.5  -1.5  1500   0.5  -1.5
1550   1.5  -1.5  1500   1.5
  -1.5  1550   2.5  -1.5  1500   2.5  -1.5  1550   3.5  -1.5  1500   3.5  -1.5
1550   4.5  -1.5  1500   4.5
  -1.5  1550   5.5  -1.5  1500   5.5  -1.5  1550  -5.5  -0.5  1500  -5.5  -0.5
1550  -4.5  -0.5  1500  -4.5
  -0.5  1550  -3.5  -0.5  1500  -3.5  -0.5  1550  -2.5  -0.5  1500  -2.5  -0.5
1550  -1.5  -0.5  1500  -1.5
```

```
  -0.5   1550 2*-0.5   1500 2*-0.5   1550    0.5   -0.5   1500    0.5   -0.5   1550    1.5
-0.5   1500    1.5   -0.5   1550
   2.5   -0.5   1500    2.5   -0.5   1550    3.5   -0.5   1500    3.5   -0.5   1550    4.5   -
0.5   1500    4.5   -0.5   1550
   5.5   -0.5   1500    5.5   -0.5   1550   -5.5    0.5   1500   -5.5    0.5   1550   -4.5
0.5   1500   -4.5    0.5   1550
  -3.5    0.5   1500   -3.5    0.5   1550   -2.5    0.5   1500   -2.5    0.5   1550   -1.5
0.5   1500   -1.5    0.5   1550
  -0.5    0.5   1500   -0.5    0.5   1550 2*0.5   1500 2*0.5   1550    1.5    0.5   1500
1.5    0.5   1550    2.5    0.5
  1500    2.5    0.5   1550    3.5    0.5   1500    3.5    0.5   1550    4.5    0.5   1500
4.5    0.5   1550    5.5    0.5
  1500    5.5    0.5   1550   -5.5    1.5   1500   -5.5    1.5   1550   -4.5    1.5   1500   -
4.5    1.5   1550   -3.5    1.5
  1500   -3.5    1.5   1550   -2.5    1.5   1500   -2.5    1.5   1550   -1.5    1.5   1500   -
1.5    1.5   1550   -0.5    1.5
  1500   -0.5    1.5   1550    0.5    1.5   1500    0.5    1.5   1550 2*1.5   1500 2*1.5
1550    2.5    1.5   1500    2.5
   1.5   1550    3.5    1.5   1500    3.5    1.5   1550    4.5    1.5   1500    4.5    1.5   1550
5.5    1.5   1500    5.5
   1.5   1550   -5.5    2.5   1500   -5.5    2.5   1550   -4.5    2.5   1500   -4.5    2.5
1550   -3.5    2.5   1500   -3.5
   2.5   1550   -2.5    2.5   1500   -2.5    2.5   1550   -1.5    2.5   1500   -1.5    2.5
1550   -0.5    2.5   1500   -0.5
   2.5   1550    0.5    2.5   1500    0.5    2.5   1550    1.5    2.5   1500    1.5    2.5   1550
2*2.5   1500 2*2.5   1550
   3.5    2.5   1500    3.5    2.5   1550    4.5    2.5   1500    4.5    2.5   1550    5.5    2.5
1500    5.5    2.5   1550
  -5.5    3.5   1500   -5.5    3.5   1550   -4.5    3.5   1500   -4.5    3.5   1550   -3.5
3.5   1500   -3.5    3.5   1550
  -2.5    3.5   1500   -2.5    3.5   1550   -1.5    3.5   1500   -1.5    3.5   1550   -0.5
3.5   1500   -0.5    3.5   1550
   0.5    3.5   1500    0.5    3.5   1550    1.5    3.5   1500    1.5    3.5   1550    2.5    3.5
1500    2.5    3.5   1550
 2*3.5   1500 2*3.5   1550    4.5    3.5   1500    4.5    3.5   1550    5.5    3.5   1500
5.5    3.5   1550   -5.5    4.5
  1500   -5.5    4.5   1550   -4.5    4.5   1500   -4.5    4.5   1550   -3.5    4.5   1500   -
3.5    4.5   1550   -2.5    4.5
  1500   -2.5    4.5   1550   -1.5    4.5   1500   -1.5    4.5   1550   -0.5    4.5   1500   -
0.5    4.5   1550    0.5    4.5
  1500    0.5    4.5   1550    1.5    4.5   1500    1.5    4.5   1550    2.5    4.5   1500
2.5    4.5   1550    3.5    4.5
  1500    3.5    4.5   1550 2*4.5   1500 2*4.5   1550    5.5    4.5   1500    5.5    4.5
1550   -5.5    5.5   1500   -5.5
   5.5   1550   -4.5    5.5   1500   -4.5    5.5   1550   -3.5    5.5   1500   -3.5    5.5
1550   -2.5    5.5   1500   -2.5
   5.5   1550   -1.5    5.5   1500   -1.5    5.5   1550   -0.5    5.5   1500   -0.5    5.5
1550    0.5    5.5   1500    0.5
   5.5   1550    1.5    5.5   1500    1.5    5.5   1550    2.5    5.5   1500    2.5    5.5   1550
3.5    5.5   1500    3.5
   5.5   1550    4.5    5.5   1500    4.5    5.5   1550 2*5.5   1500 2*5.5   1550 /
```

```
NOECHO

ZCORN
   484*1500   968*1500.5        968*1501   968*1501.5        968*1502   968*1502.5
968*1503 968*1503.5   968*1504 968*1504.5   968*1505
 968*1505.5        968*1506   968*1506.5        968*1507   968*1507.5        968*1508
968*1508.5   968*1509 968*1509.5   968*1510 968*1510.5
   968*1511   968*1511.5        968*1512   968*1512.5        968*1513   968*1513.5
968*1514 968*1514.5   968*1515 968*1515.5   968*1516
 968*1516.5        968*1517   968*1517.5        968*1518   968*1518.5        968*1519
968*1519.5   968*1520 968*1520.5   968*1521 968*1521.5
   968*1522   968*1522.5        968*1523   968*1523.5        968*1524   968*1524.5
968*1525 968*1525.5   968*1526 968*1526.5   968*1527
 968*1527.5        968*1528   968*1528.5        968*1529   968*1529.5        968*1530
968*1530.5   968*1531 968*1531.5   968*1532 968*1532.5
   968*1533   968*1533.5        968*1534   968*1534.5        968*1535   968*1535.5
968*1536 968*1536.5   968*1537 968*1537.5   968*1538
 968*1538.5        968*1539   968*1539.5        968*1540   968*1540.5        968*1541
968*1541.5   968*1542 968*1542.5   968*1543 968*1543.5
   968*1544   968*1544.5        968*1545   968*1545.5        968*1546   968*1546.5
968*1547 968*1547.5   968*1548 968*1548.5   968*1549
 968*1549.5   484*1550 /

PORO
 4840*0.01  7260*0.2 /
PERMX
 4840*0.0001    7260*100 /
PERMY
 4840*0.0001    7260*100 /
PERMZ
 4840*0.00001      7260*10 /
```

Appendix 2

For Cases A1 and A2:

```
DIMENS
 11 11 100 /



TABDIMS
 1 1 50 50 8* 1 /



WELLDIMS
 2 60 1 2 /

EQLDIMS
         2 1* 4 /
```

For Cases B1 and B2:

```
DIMENS
 1 1 100 /



TABDIMS
 1 1 50 50 8* 1 /



WELLDIMS
 2 60 1 2 /

EQLDIMS
 2 1* 4 /
```

Appendix 3

$$D_{AB} = \frac{\left[3.03 - \left(\frac{0.98}{M_{AB}^{\frac{1}{2}}}\right)\right](10^{-3})T^{\frac{3}{2}}}{P M_{AB}^{\frac{1}{2}} \sigma_{AB}^{2} \Omega_D}$$

T=50℃

P=50 barsa

1. CO_2 diffusion in CH_4

$\sigma_{CO_2} = 3.941$ Å
$\sigma_{CH_4} = 3.758$ Å

$$\rightarrow \sigma_{AB} = \frac{\sigma_{CO_2} + \sigma_{CH_4}}{2} = 3.8495 \text{ Å}$$

$M_{CO_2} = 44.0095\ kg/kmol$
$M_{CH_4} = 16.0425\ kg/kmol$

$$\rightarrow M_{AB} = 2\left(\frac{1}{M_{CO_2}} + \frac{1}{M_{CH_4}}\right)^{-1} = 23.5137\,\frac{kg}{kmol}$$

$\Omega_D = \frac{a}{(T^*)^b} + \frac{c}{\exp(dT^*)} + \frac{e}{\exp(fT^*)} + \frac{g}{\exp(hT^*)}$

$T^* = \frac{T}{\frac{\varepsilon_{AB}}{\kappa}} 1.897$
$\varepsilon_{CO_2} = 195.2K \times 1.38 \times \frac{10^{-16} erg}{K} = 2.69376 \times 10^{-14}\ erg$
$\varepsilon_{CH_4} = 148.6 \times 1.38 \times 10^{-16} = 2.050 \times 10^{-14} erg$

$$\rightarrow \varepsilon_{AB} = (\varepsilon_A \varepsilon_B)^{0.5} = 2.35 \times 10^{-14}\ erg$$

$$\rightarrow \Omega_D = \frac{1.06036}{(1.897)^{0.15610}} + \frac{0.19300}{\exp\,(0.47635 \times 1.897)} + \frac{1.03587}{\exp\,(1.52996 \times 1.897)} + \frac{1.76474}{\exp\,(3.89411 \times 1.897)} = 1.0956$$

$\boxed{D_{AB} = 4.17 \times 10^{-3} cm^2/s}$

2. H_2 diffusion in CH_4

$\sigma_{H_2} = 2.827$Å
$\sigma_{CH_4} = 3.758$ Å
$\rightarrow \sigma_{AB} = 3.2925$ Å

$M_{H_2} = 2.016\ kg/kmol$
$M_{CH_4} = 16.0425\ kg/kmol$

$\rightarrow M_{AB} = 3.58\ kg/kmol$

$$\rightarrow \Omega_D = 0.917$$
$$T^* = 3.43$$

$\varepsilon_{H_2} = 8.2386 \times 10^{-5}\ erg$
$\varepsilon_{CH_4} = 2.050 \times 10^{-14} erg$

$$\rightarrow \varepsilon_{AB} = 1.3 \times 10^{-14} erg$$

$$\boxed{D_{AB} = 1.39 \times 10^{-3} cm^2/s}$$

3. CH_4 self-diffusion

$\sigma_{CH_4} = 3.758$ Å
$T^* = 2.175$
$M_{CH_4} = 16.0425\ kg/kmol$

$\mathcal{E}_{CH_4} = 2.050 \times 10^{-14} erg$
$\Omega_D = 1.045$

$$\boxed{D_{CH_4} = 5.47 \times 10^{-3} cm^2/s}$$